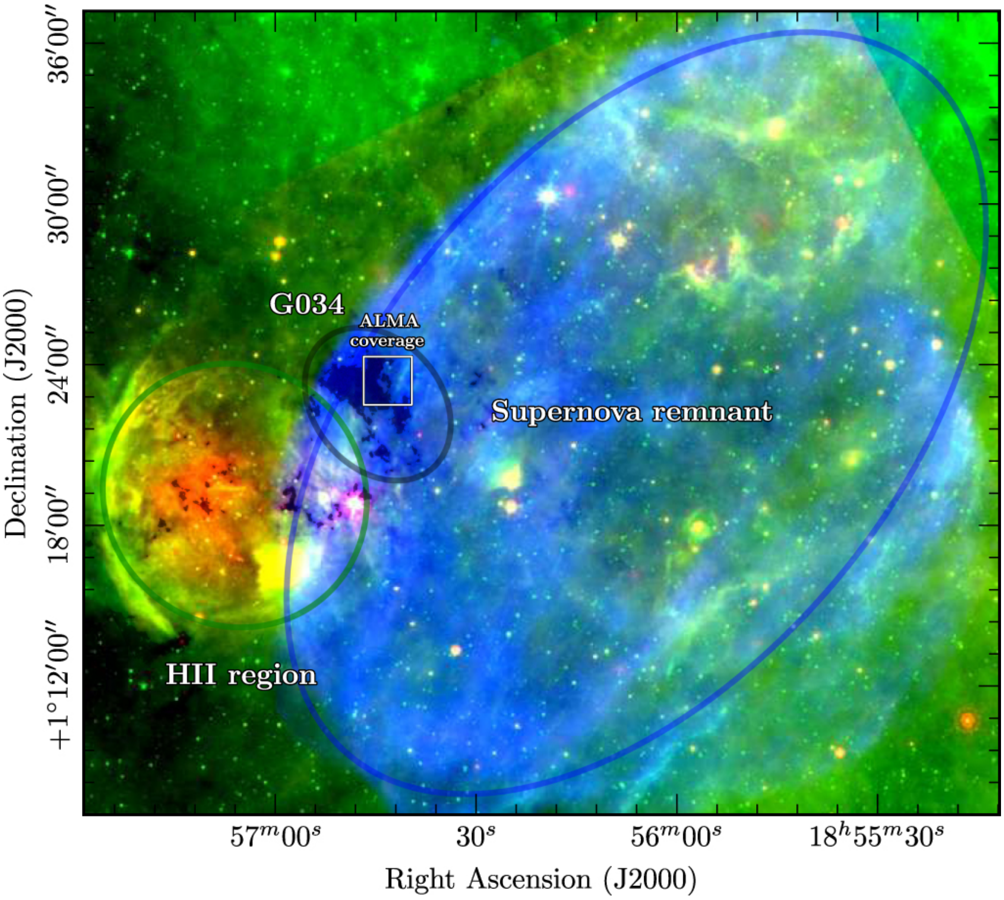

Impact of a Supernova Remnant on the Physical and Chemical Properties of an Infrared Dark Cloud

Ana-Mari Petrova

Department of Physics

CHALMERS UNIVERSITY OF TECHNOLOGY
Gothenburg, Sweden 2023
www.chalmers.se

Master's thesis 2023

Impact of a Supernova Remnant on the Physical and Chemical Properties of an Infrared Dark Cloud

Ana-Mari Petrova

Department of Space, Earth and Environment
Chalmers University of Technology
Gothenburg, Sweden 2023

Impact of a Supernova Remnant on the Physical and Chemical Properties of an Infrared Dark Cloud

Supervisor: Dr. Giuliana Cosentino, Department of Space, Earth and Environment
Examiner: Prof. Jonathan C. Tan, Department of Space, Earth and Enviroment

Master's Thesis 2023
Department of Space, Earth and Environment
Chalmers University of Technology
SE-412 96 Gothenburg
Telephone +46 31 772 1000

Cover: Shows a three-color image of G34.77-00.55 (confined by the black ellipse) besides the HII region G034.8-0.7 (green ellipse) and the SNR W44 (blue ellipse). The Figure was obtained from Cosentino et al. (2019).

Typeset in LaTeX
Gothenburg, Sweden 2023

Impact of a Supernova Remnant on the Physical and Chemical Properties of an Infrared Dark Cloud
Ana-Mari Petrova
Department of Physics
Chalmers University of Technology

Abstract

Massive stars play a fundamental role in the evolution of the Universe, but the process that initiates their formation from molecular clouds remains much debated. One way to understand the initial conditions required for massive star formation is to study Infrared Dark Clouds (IRDCs), which are cold, dense regions in the interstellar medium (ISM) seen as dark features at infrared wavelengths. Stellar feedback in the form of supernova remnants (SNRs) and HII regions has been proposed to have a large impact on the physical and chemical state of IRDCs. However, whether this feedback enhances or suppresses star formation, i.e., whether it is positive or negative feedback, is uncertain. Here we study the physical and chemical conditions of the IRDC G34.77-0.55, which is in close proximity to the SNR W44 and the HII region G34.8-0.7. We observed ^{13}CO(1-0) and C^{18}O(1-0) line emission from the IRDC and its surroundings using the Green Bank Telescope (GBT). We also observed several other molecular line species tracing higher density conditions using the Instituto de Radioastronomia Milimetrica (IRAM) 30m telescope. Mass surface density and temperature maps derived from archival Spitzer and Herschel Space Telescope data were also utilized. With these data, we first study the kinematics, by producing first moment maps that reveal a velocity gradient from high (more redshifted) to low (more blueshifted) values from the HII region side to the SNR side. This may indicate that the IRDC is located beyond the HII region and in front of the SNR. In addition, we also study the abundances of various species, especially CO, HCO$^+$, and N$_2$H$^+$. In cold, dense regions CO freezes out from the gas phase to form CO ice coatings on dust grains. We present maps of the CO depletion factor, which measures the extent of this process, and study how it depends on physical conditions. Combined with the abundances of HCO$^+$ and N$_2$H$^+$, astrochemical modeling is applied to constrain the age of the cloud to be $\sim 10^5$ - 10^6 yr and the cosmic ray ionization rate (CRIR) $\sim 10^{-17}$ s^{-1}. This CRIR is several times larger than that inferred by identical methods in another IRDC, which may indicate the impact of the W44 SNR on G34.77-0.55. However, the overall rate is still significantly lower than that of the diffuse ISM, suggesting a role for absorption or screening processes that reduce the efficiency of CR propagation into IRDCs. We discuss the location and dynamical state of dense gas structures in the IRDC and their relation to the surrounding feedback.

Keywords: IRDC G34.77-00.55 - astrochemistry - SNR W44 - star formation.

Acknowledgements

I would like to start by thanking everybody in the Chalmers Initiative on Cosmic Origins (CICO) for making me feel welcome and as a part of the group. I will cherish the time spent, the memories shared, and the things that I learned along the way. I would especially like to thank Dr. Giuliana Cosentino for her role as my supervisor. None of this would have been possible without her support, dedication, and guidance throughout the whole process. I would also like to express my gratitude towards Prof. Jonathan C. Tan for giving me this special opportunity, to begin with, and for helping me to expand my network. I would also like to thank him for his insightful feedback during the group meetings and his dedication to bringing out the best in us.

Ana-Mari Petrova, Gothenburg, April 2023

Contents

List of Figures

List of Tables

1

Introduction

1.1 The problem of massive star formation

Massive stars are defined by the fact that their masses are greater than $8\mathrm{M}_{\odot}$, and they play a crucial role in the physical and chemical evolution of galaxies. They supply the interstellar medium (ISM) with a great amount of energy and turbulence by means of stellar feedback (e.g. by stellar winds, jets, molecular outflows, HII regions, and supernova explosions). Furthermore, the gas returning from these stars is generally enriched in heavy elements that have been forged within their cores. Despite this importance, the mechanisms that regulate the formation of massive stars from molecular clouds remain an open question.

There are certain challenges that arise when observing massive stars. One such limitation is that they tend to have shorter evolutionary timescales with respect to their low-mass counterparts. Massive stars tend to enter the main sequence whilst still embedded inside the envelope, which is very dense and therefore optically thick at optical and near/mid-infrared wavelengths. Another limitation is the difficulty of gathering a large enough sample of massive stars to study, seeing as massive stars are numerically rare as reported by Frost et al. (2021) and are usually far away ($d > 5$ kpc), posing additional challenges to their detection. In light of all these technical aspects and due to the great impact that these objects have on their surroundings, studying the formation process of these objects can in general be considered challenging. An alternative way to approach the problem is to study the clouds in which they are born to infer the initial physical and chemical conditions required to form massive stars. These clouds are known as Infrared Dark Clouds.

1.2 Infrared Dark Clouds

Molecular clouds are cold and dense structures of the ISM that host the formation of stars. The most massive of these molecular clouds are known as Infrared Dark Clouds (IRDCs). IRDCs are in general characterized as cold ($T < 25$ K; e.g., Rathborne et al. (2006), Lim et al. (2016)), dense ($n_{\mathrm{H}_2} > 10^4$ cm^{-3}; e.g. Butler & Tan (2009), Kainulainen & Tan (2013), Lim et al. (2016)) and highly extincted regions ($A_V > 100$ mag; e.g., Butler & Tan (2009), Kainulainen & Tan (2013), Lim et al. (2016)) that represent the densest part (mass surface densities > 0.1 g cm^{-2}; Tan et al. (2014)) of Giant Molecular Clouds (GMCs). IRDCs were first detected in the late '90s by the Infrared Space Observatory (Perault et al., 1996) and the Midcourse Space Experiment (MSX) (Egan et al., 1998), which surveyed the Galactic plane and detected a plethora of dark silhouettes against the bright Galactic background emission. As the name would suggest, the clouds appeared dark because the background radiation was absorbed by the cloud at optical and near-infrared wavelengths (e.g., Chira et al. (2013), Perault et al. (1996), Egan et al. (1998)). Roughly 11,000 IRDCs were identified from the 8.3 μm Midcourse Space experiment images (Simon et al., 2006a), that differed greatly in both size and mass and most of them were reported to be gravitationally bound (Peretto & Fuller (2010)). IRDCs are relatively quiescent regions within GMCs, showing low star-formation activity, (Bergin & Tafalla, 2007), with H_2 column densities comparable to those from regions known to harbor massive stars (e.g. Rathborne et al. (2006),Simon et al. (2006b), Peretto & Fuller (2010)). In addition, IRDCs are also known to host cold cores (described as extraordinarily dense and massive fragments of gas and dust) and are believed to represent the earliest phase of massive star formation (Rathborne et al., 2006).

For all these reasons, IRDCs have been considered for a long time as the designated birthplaces of massive stars (e.g. Rathborne et al. (2006),Carey et al. (2000),Battersby et al. (2010)). Nowadays, we know that IRDCs host star formation at a wide range of masses, i.e., from low- to intermediate to high-mass star formation (e.g. Foster et al. (2014), Sanhueza et al. (2017)). Hence, IRDcs may potentially host most of the star formation in our Galaxy. It is therefore crucial to investigate their physical and chemical properties and how these relate to those required to initiate star formation.

1.2.1 Chemical Properties of IRDCs

IRDCs are primarily made of molecular gas and dust. Even though H_2 is the most abundant molecule in gas-phase, it is still an ineffective tracer. Indeed, the low temperatures found in IRDCs do not allow H_2 to be excited (Heyer & Dame, 2015) (ground state 500 K). At these low temperatures, rotational transitions of molecular species at mm wavelengths are efficiently excited and represent excellent tools for tracing the physical and chemical conditions of clouds. However, the H_2 molecule has no dipole moment and cannot be detected at these wavelengths.

Carbon Monoxide (CO) on the other hand is the second most abundant molecule and has low rotational transitions that lie in the range of 5-22 K from the ground state (Heyer & Dame, 2015) and can therefore be used to probe the colder regions of the interstellar medium. CO is also known to probe low-density gas, and has a critical density of roughly 2700 cm^{-3} (Fontani et al., 2012). But due to the high abundance of CO in molecular clouds, the J=1-0 transition has a tendency to be optically thick for the denser regions, which proves to be a challenge when trying to estimate the mass of the cloud. For this very reason, isotopologues such as ^{13}CO and C^{18}O are observed instead. There is still however, a possibility that ^{13}CO could become optically thick for the denser regions. But since both ^{13}CO and C^{18}O are less abundant than the main CO isotopologue, C^{18}O even more so than ^{13}CO, they contribute to a more precise estimation of the cloud and its structure (Sabatini et al., 2019).

Besides optical depth considerations, CO is known to be an early depleter. Indeed, at the low temperatures of IRDCs, CO tends to freeze onto the interstellar dust grains, resulting in an overall depletion of CO in the gas phase (Sabatini et al., 2019). The depletion factor, f_D, for CO corresponds to the ratio between the amount of CO expected in the gas phase to that effectively measured. A depletion factor value of one would suggest that all of the CO is in the gas phase. CO depletion factor values greater than one would therefore indicate a higher concentration of CO on the dust grain surface, which could be beneficial for the surface reactions (Sabatini et al., 2019) and help form more complex organic species in IRDCs.

While the freeze-out process decreases the abundance of specific molecular species, the desorption induced by cosmic rays can cause species that are formed/deposited onto the surface of dust grains to be released back into the gas phase, therefore increasing their abundance with respect to H_2. Cosmic rays are defined as charged particles, mainly protons (Vaupré et al. (2014), Ackermann et al. (2013)), that have different origins and permeate the ISM. One theory to explain the origin of Cosmic Rays is through Supernova Remnants (SNRs) (Hillas, 2005), where the protons are accelerated by the shock front as the SNRs expand (Bell, 1978). The effects of cosmic rays on CO were first investigated by Hasegawa & Herbst (1993). The authors modeled the cloud as a mixture of CO in the gas phase and onto dust grains. Cosmic rays can also influence the gas's degree of ionization. By impacting neutral species, they can form molecular ions and radicals.

The Cosmic Ray Ionization Rate (CRIR) is the ionization rate per atomic hydrogen and is denoted as ζ. A recent study by Entekhabi et al. (2021) estimated the CRIR of the IRDC G28.37+00.07 to be roughly $2 - 4 \cdot 10^{-18}$ s^{-1}. For comparison, the CRIR for the diffuse interstellar medium was found to be around 2.9 $\cdot 10^{-16}$ s^{-1} per H atom (Neufeld & Wolfire, 2017). Another benchmark/ point of reference is that studies have measured CRIR values greater than 10^{-15} s^{-1} for regions that are known to harbor some degree of star formation activity (Fontani et al., 2017).

The low CRIR value for the IRDC was believed to be due to the absorption of the lower energy cosmic rays by regions with a great column density (Neufeld & Wolfire, 2017). The highly charged particles would lose kinetic energy each time they interact with molecules in the IRDC and the number of interactions increases for higher column densities (Silsbee & Ivlev, 2020). But the presence of a SNR could potentially enhance the CRIR, which in turn may also affect the presence of ions in the post-shocked gas.

HCO^+, $H^{13}CN$ are additional tracers of dense gas as reported by Vasyunina et al. (2011), HCO^+ is describe as a good molecular outflow tracer.

N_2H^+ is a dense gas tracer with a critical density of $1.5 \cdot 10^5$ cm^{-2} (Zhang et al., 2020) and the molecule is referred to as a late depleter (Vasyunina et al., 2011), meaning that the freeze-out process doesn't affect the abundance of the molecule as much in comparison to CO.

Methanol (CH_3OH) is a low-velocity shock tracer (Jiménez-Serra et al., 2005) and the presence of CH_3OH in high quantity could possibly indicate star-forming activity. HNCO is also refered to as a potential shock tracer (Vasyunina et al., 2011).

1.2.2 Star formation in IRDCs

As mentioned before, the mechanisms that ignite star formation in molecular clouds, and especially massive star formation, are still under debate. There have been several theories suggested in order to understand what triggers the formation of a cloud in turn triggering star formation. Stars were previously believed to form due to molecular clouds collapsing due to self-gravity, which occurs when the mass of the cloud exceeds the Jeans Mass.

There are other possible scenarios besides a gravitational collapse that could trigger a star formation. One such example would be a cloud-cloud collision, where IRDCs are believed to have emerged from the compressed regions, as a result of a collision between two former molecular clouds. In (Fukui et al., 2020), the author assembled a table incorporating more than 50 regions harboring massive stars, on the basis that the massive star formation was believed to be triggered by the cloud-cloud collision.

Another theory is the flow-driven scenario, which investigates the collision between large-scale flows consisting of warm atomic gas, which could originate from stellar feedback (Heitsch et al., 2008). The collision forms a compressed layer where the column density of hydrogen atoms exceeds 10^{21} cm^{-2}, which is the required column density in order to shield the molecular gas from the dissociative effect caused by the ultraviolet radiation (van Dishoeck & Black (1988), Hartmann et al. (2001)). These compressed layers could trigger the rapid formation of filamentary molecular clouds and in turn star formation in the more density-enhanced regions (Ballesteros-Paredes et al. (1999),Hartmann et al. (2001)).

Another possible theory involves shock waves from stellar feedback, which proposes that the ejected energy wave impacting the cloud could cause parts of it to compress (Cosentino et al., 2022). The stellar feedback can either be described as a positive or a negative feedback, depending on whether it helps or suppress star formation. The feedback from a supernova explosion for example is described as long-lasting (Leitherer et al. (1999), Agertz et al. (2013)) and as highly energetic (Bally, 2010). The interstellar shock created by a SNR could possibly disperse the molecules, and in a sense decrease the density and therefore suppress the formation of stars (Leroy et al., 2013). But it could also enhance the density of the surrounding molecular gas as well as its turbulence when it keeps expanding outwards, all of which could contribute to star formation (Cosentino et al., 2022).

1.2.3 IRDC G34.77-0.55

This work focuses on the IRDC G34.77-0.55, from here on out referred to as Cloud G (Butler & Tan (2009), Butler & Tan (2012)). Located in the Aquila constellation at a near kinematic distance of 2.9 kpc (Simon et al., 2006b). As previously mentioned, it was first detected as a dark feature by the Infrared Space Observatory (Perault et al., 1996) and the Midcourse Space Experiment (Egan et al., 1998), Cloud G was later included in the IRDC MSX catalog presented by Simon et al. (2006a)). By investigating the ^{13}CO(1-0) emission associated with the cloud, Rathborne et al. (2006), estimated the cloud central velocity to be ~43.5 km/s (see also Simon et al. (2006b), Butler & Tan (2009), Butler & Tan (2012), Hernandez & Tan (2015)) and identified four cores within the cloud, where one of the cores is described as very dense and warm and is believed to be protostellar in nature. Cloud G was also a part of the 10 IRDC samples by Butler & Tan (2009) and Kainulainen & Tan (2013) where the authors investigated near-IR and mid-IR imaging data to build mass surface density maps of the 10 clouds.

In a later study presented by Cosentino et al. (2018), the dense gas (traced by $H^{13}CO^+$ and $HN^{13}C$) and the shocked gas (traced by SiO and CH_3OH) within cloud G were analyzed. The authors found that the dense gas within the cloud presents several velocity components, that were only separated by a few km/s. Furthermore, the shocked gas probed by the SiO emission is located at the edge of the cloud, far off from the cores previously identified by Rathborne et al. (2006), and was therefore not believed to be due to actively forming stars. The CH_3OH emission was mentioned to be more widespread than the SiO, but that it also showed a clear enhancement toward the same region. Cloud G showed narrow SiO and CH_3OH line emission, with widths of $\sim$ 2 km/s (Cosentino et al., 2018), all of which could point towards the fact that the cloud might have interacted with large-scale shock (Cosentino et al., 2018). A narrow SiO emission line ($\leq$ 1-2 km/s) usually indicates low-velocity shocks (Jiménez-Serra et al., 2009). The shocked gas at the edge of the cloud is likely due to the interaction between the IRDC and the nearby SNR W44 (Sashida et al. (2013), Cosentino et al. (2019)). Indeed, cloud G is located at the same distance and in between the HII region G34.8-0.7 and the SNR W44. The cloud's interaction with the SNR was first reported by Wootten (1978). The shock originating from the SNR is expanding into the cloud at a velocity $\sim$ 13 km/s (Sashida et al., 2013). Follow-up ALMA observations presented by Cosentino et al. (2019) showed that the shock is plunging into a dense ridge at the edge of the cloud and that it is enhancing the gas density to values $>10^5$ cm^{-3}, compatible with those required to form massive stars.

1.3 Virial Analysis

Although IRDCs are relatively dense structures, the material within them needs to be gravitationally bound in order to form stars. This condition is usually exploited by performing a virial analysis of the gas, that relates kinetic energy to gravitational potential energy according to $2E_K + E_G = 0$ and the virial parameter is defined as $\alpha_{\rm vir} \equiv 2E_K/E_G$ (Bertoldi & McKee, 1992). When $\alpha_{\rm vir} < 2$, then that region is what we refer to as gravitationally bound, which could possibly collapse and potentially form stars if some of the internal kinetic energy is lost. By writing out the expressions for E_K and E_G for a uniform sphere, we arrive at an expression for $\alpha_{\rm vir}$ in terms of the mass, radius, and velocity dispersion:

$$\alpha_{\mathrm{vir}} = \frac{M\sigma_{\mathrm{3D}}^2}{3GM^2/5R} = \frac{5R\sigma_{\mathrm{1D}}^2}{GM}. \tag{1.1}$$

Here the final expression is in terms of the 1D velocity dispersion, which is measured from the molecular line spectra. In this consideration, spherical geometry is assumed and magnetic field effects are neglected.

1.3.1 Aim and outline of the thesis

The aim of this thesis is to investigate the physical properties and kinematic structures of the IRDC G034.77-00.55, which is known to interact with a SNR and a HII region. We aim to investigate whether the presence of SNR in the surrounding affects the cloud's physical properties, including its kinematics, dynamics, CO depletion factor, and CRIR.

The outline of this thesis is as follows:

Firstly, we present the observational data alongside the mass surface density and dust temperature maps that are utilized in this work in Chapter 2.
This is followed by the result presented in Chapter 3.
In section 3.1, we carry out an analysis of methods for the spectral data cubes obtained with the Green Bank telescope and present maps of the estimated noise level and the integrated intensity of ^{13}CO(1-0) and C^{18}O(1-0).
The outcome of the kinematic analysis of Cloud G is presented in section 3.2, such as the channel maps of the spectral cube, and moment 1 and 2 maps.
In section 3.3, we present the estimated column density, abundance, and CO depletion factor of Cloud G, for each CO isotopologue and mass surface density map.
In section 3.4 we carry out a virial analysis of the cores.
The integrated intensity, column density, and molecular abundances of the following species: H^{13}CO$^+$(1-0), HC^{18}O$^+$(1-0), N$_2$H$^+$(1-0), HNCO(4-3), HN^{13}CO(1-0), H$_2$CO(2-1), and CH$_3$OH(3-2) are presented in section 3.5.
The observed abundance of the species in section 3.5 are furthermore compared to theoretical abundances derived from the chemical models developed in Entekhabi et al. (2021). Lastly, the results of the chemical models are presented in section 3.6.
Then, in Chapter 4, we discuss the results and the implications that our assumptions might have had on the result, following the same order established in the result section.
We finally, present our conclusions in Chapter 5.

2

Observations and Data

In this work, we use several datasets collected by multiple telescopes working at mm and IR wavelengths. In particular, observations of molecular rotational transitions were collected using the Green Bank 100m Telescope (GBT) and the 30m antenna at the Instituto de Radioastronomia Millimetrica (IRAM-30m). Other datasets, such as mass surface densities and dust temperatures across the source, were obtained by postprocessing IR images obtained by the Herschel and Spitzer telescopes. The following chapter is a detailed description of the datasets and the technical aspects of their acquisition and processing.

2.1 ^{13}CO(1-0) and C^{18}O(1-0) emission maps from Green Bank Telecope

Observations of ^{13}CO(1-0) and C^{18}O(1-0) emission towards the IRDC G034.77-00.55 were carried out in April 2021 with the 100m Green Bank Telescope (GBT, West Virginia, USA). It consists of a 16-element array, a 4x4 configuration in the plane spanned by the elevation and cross-elevation, where each element is separated from the others by $30.4''$ (information extracted from the GBT Observer's Guide). A fast mapping method was adopted for our observations, where the sky was scanned in parallel rows with a width of $5.58''$ in the direction of the Galactic Longitude. The observations were obtained in units of antenna temperature. Afterward, the GBT native software GBTIDL was used to calibrate and reduce the data. In particular, the data showed a sinusoidal systematic baseline that was removed. The final GBT dataset has a beam size of $\sim 7''$ and a velocity resolution of 0.19 km/s. The integrated noise is estimated in section 3.1 to range from 0.14-0.27 K km/s for ^{13}CO and 0.21-0.29 K km/s for C^{18}O. The size of the original map was 8.3 x 14.8 $'^2$ with the central coordinates $34^{o}44'04''$ and $-0^{o}33'18''$.

2.2 Other Molecular Transitions with IRAM-30m

As part of this work, we investigate the spatial distribution and molecular abundance of additional species, mainly tracers of the dense gas. In particular, we target the J=1-0 transition of N_2H^+, $H^{13}CO^+$,$C^{18}O$, $HC^{18}O^+$, $HN^{13}C$, the J=2-1 transition of H_2CO, the J=3-2 transition of CH_3OH, and the J=4-3 transition of HNCO. The data were obtained using the IRAM-30m antenna (Instituto de RadioAstronomia

Millimetrica, Pico Veleta, Spain), during May and September 2013. The observations utilized the On-The-Fly observing mode, where the telescope is moving continuously over the target and sorting the accumulated data into a grid. The obtained maps were of the size of 3.4 x 4 $'^2$ with central coordinates $\alpha(J2000) = 18^h56^m45^s$ and $\delta(J2000) = 1°21'45''$ and an off-position of (-240″,-40″) (Cosentino et al., 2018). An angular distance of 6″ was utilized in the direction perpendicular to the line-of-sight of Cloud G.

The Fourier Transform Spectrometer was utilized during the observations, which provided a spectral resolution of 200 kHz. At the frequencies of our target molecules (85.162-145.602 GHz), this corresponds to velocity resolutions in the range of 0.402-0.688 km/s. The observations were measured in units of antenna temperature but were converted into a main-beam temperature, using a beam efficiency of 0.79-0.82 and forward efficiency of 0.95. The final datacubes have pixel size 14.4″, beam size 28.89″ and rms per channel of 0.003-0.02 K.

The CLASS software from the GILDAS package was used in order to produce data cubes, which were further displayed with the programming language, Python. The properties of the original maps for the different molecules are listed in Table 2.1 below.

Table 2.1: A collection of observational properties for the different molecules, such as the velocity resolution, the number of channels, rms per channel in mK, beam efficiencies, spatial resolutions, pixel size, and initial beam sizes for all the observed transitions in this work.

Species	δv (km/s)	N_{ch}	rms	Beam eff (mK)	Pixel size (″)	Telescope beam (″)
	GBT data					
$^{13}CO(1\text{-}0)$	0.187	261	159	0.34	2.75	5.50
$C^{18}O(1\text{-}0)$	0.187	261	233	0.34	2.75	5.50
	IRAM data					
$H^{13}CO^{+}(1\text{-}0)$	0.675	150	4	0.81	14.18	28.36
$HC^{18}O^{+}(1\text{-}0)$	0.688	148	11	0.81	14.44	28.89
$C^{18}O(1\text{-}0)$	0.053	1687	20	0.79	14.00	28.00
$N_2H^{+}(1\text{-}0)$	0.063	1273	19	0.82	13.20	26.40
HNCO(4-3)	0.666	152	4	0.81	14.74	29.49
$HN^{13}C(1\text{-}0)$	0.672	151	3	0.81	14.88	29.77
$H_2CO(2\text{-}1)$	0.402	251	5	0.79	8.90	17.81
$CH_3OH(3\text{-}2)$	0.404	250	5	0.79	8.93	17.87

2.3 Mass Surface Density and Dust Temperature Maps

Multi-wavelength (70-500 μm) images obtained by the Herschel telescope as part of the Herschel Infrared Galactic Plane Survey (HiGAL; Molinari et al. (2016)) were used to obtain a mass surface density and a dust temperatures map toward Cloud G. As reported by Lim et al. (2016), the images were first reported to the same pixel size of 36″ i.e., corresponding to the pixel size of the 500 μm image.

The Hershel images were corrected by modeling and subtracting the background emission. Two methods were used for modeling the background emission. The ”Galactic Gaussian (GG)” method assumes that the local latitudinal profile of background emission is a Gaussian centered on the Galactic plane. This profile is characterized and then subtracted from all five Hi-GAL wavelengths from 70 to 500 μm.

The "Small Median Filter (SMF)" method characterizes the background based on median filtering around the elliptical region of the defined IRDC. The background intensity in the elliptical region is then estimated by interpolation and subtracted from all images as in the GG method.

Following background subtraction, a modified black body function was fit for each 36″ pixel. The best-fitting procedure returned a mass surface density and dust temperature value for each pixel. From the best parameters, maps of the two quantities were obtained; the total mass surface density, Σ, and dust temperature, T. This process was then repeated at an 18″ resolution, while retaining the dust temperature values from the 36″ resolution map, to derive a so-called "hires" map of Σ. The Σ maps used in our study are the hires $\Sigma_{\rm GG}$ and $\Sigma_{\rm SMF}$ maps, which are shown in Figure 2.1. The corresponding temperature maps for the GG and SMF methods are shown in Fig. 2.2.

Note that white pixels in these Σ maps have been masked due to the pixels showing a negative flux value for at least one wavelength. According to Lim et al. (2016) the values of the $\Sigma_{\rm SMF}$ map surrounding the IRDC tend to be underestimated. Note this latter method sets the background intensity via a more local estimation around the IRDC, so it lacks sensitivity to these surrounding regions. When comparing the GG and SMF maps, the latter method yields colder temperature estimates in the main, dense region of the IRDC, while the Σ values derived through the SMF method are slightly higher. Systematic uncertainties in these maps are estimated to be at the $\sim 30\%$ level.

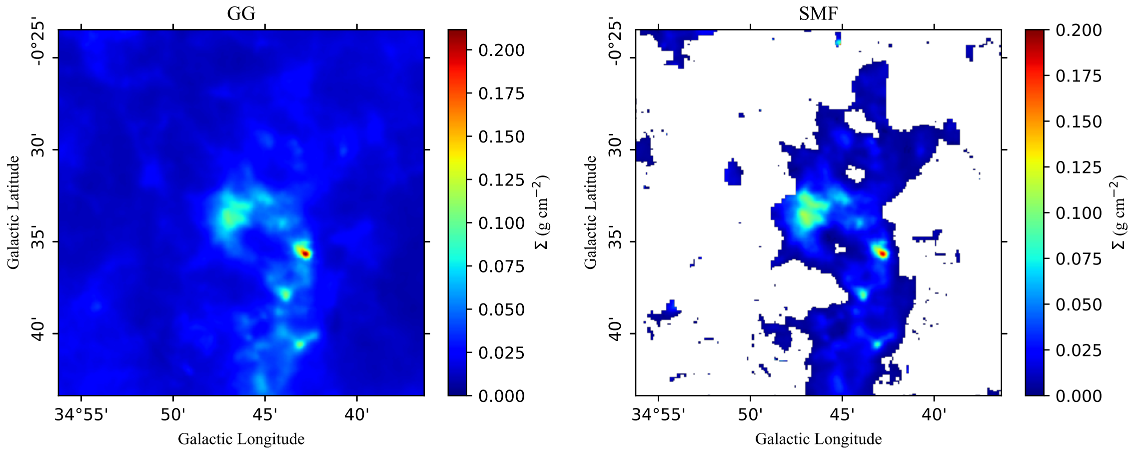

Figure 2.1: High-resolution (18″) mass surface density maps (color scale) of the IRDC G034.77-00.55 derived from Herschel images following the method described by Lim et al. (2016) and applying galactic gaussian (left panel) and small median filter (right panel) background subtraction.

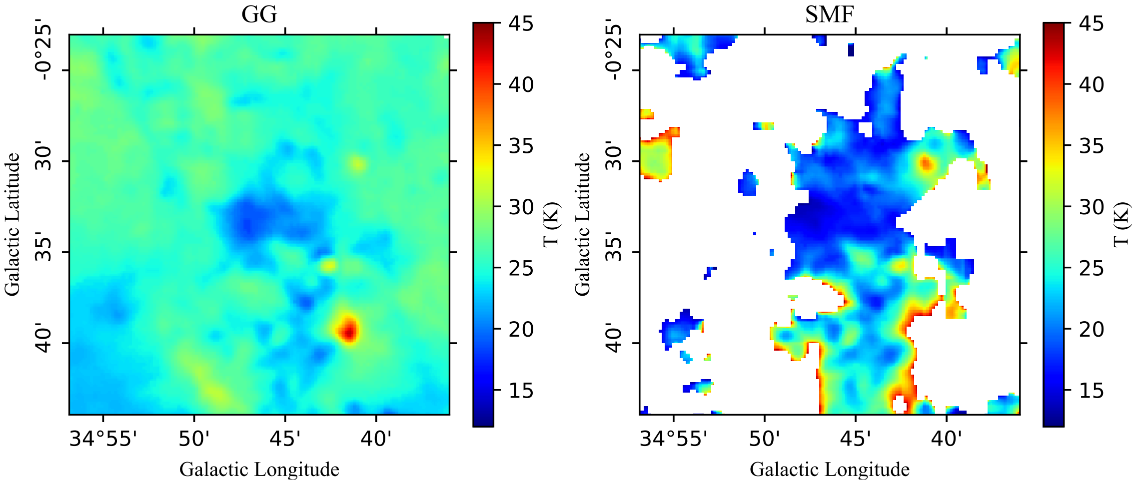

Figure 2.2: High-resolution (36″) dust temperature maps (color scale) of the IRDC G034.77-00.55 derived from Herschel images following the method described by Lim et al. (2016) and applying galactic gaussian (left panel) and small median filter (right panel) background subtraction.

A second method to estimate the mass surface density is based on MIR extinction (MIREX) by utelizing the Spitzer GLIMPSE $8\,\mu$m images that have a corresponding 2″ resolution (Butler & Tan (2012), Kainulainen & Tan (2013)). This method was developed originally in order to examine cold, high mass surface density regions, i.e., MIR dark (which is why the method struggles with MIR bright regions). However, the systematic uncertainties of the method associated with the zero point offset mean that it is less reliable at low mass surface densities, i.e., $\Sigma < 0.05\ \mathrm{g\,cm^{-2}}$. These systematic uncertainties were reduced by combining the maps with the lower spatial resolution NIR extinction maps (Kainulainen & Tan (2013) [KT13]). We will use these KT13 maps in this project, especially when probing the central, cold dense region of the IRDC. Note, that the MIREX method is independent of temperature; but at the same time, no temperature information is directly available on the same spatial scales as the MIREX map. The white pixels in Figure 2.3 correspond to regions in which the method is not efficient due to the bright IR emission.

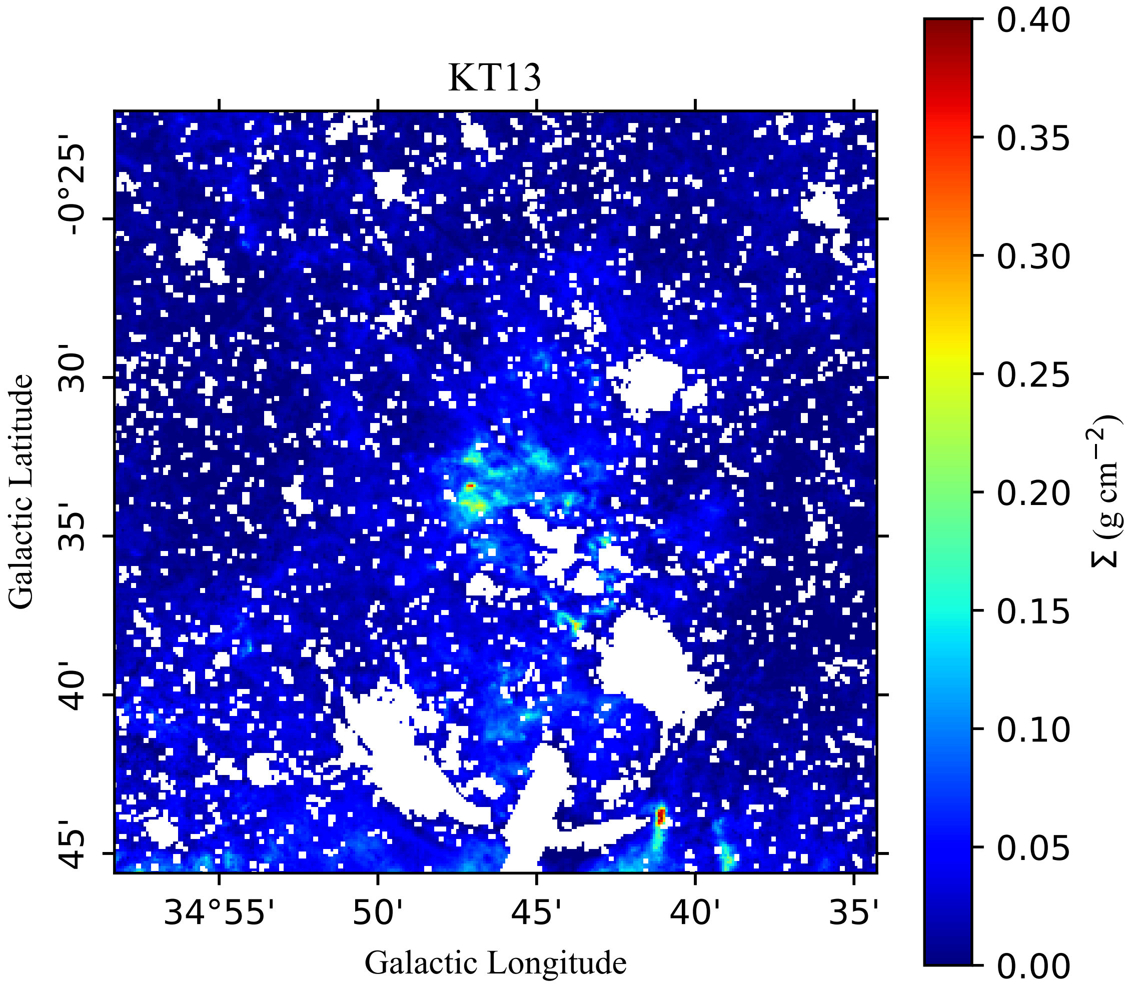

Figure 2.3: Mass surface density map derived from the mid-infrared (8 μm) extinction (MIREX) technique, including larger-scale NIR correction (Kainulainen & Tan, 2013). The effective angular resolution of this map is 2″.

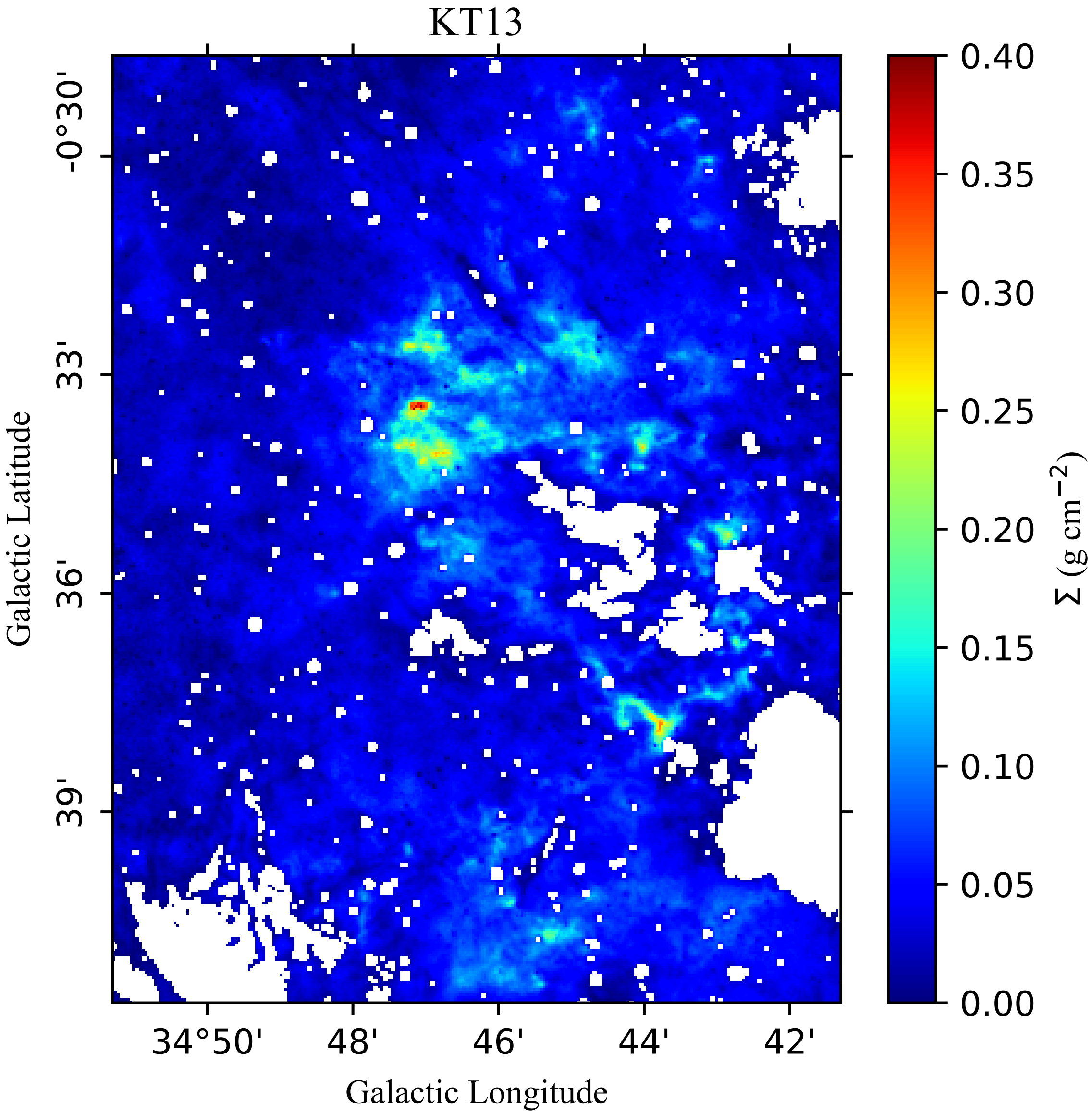

Figure 2.4: Zoomed in more closely towards the IRDC in Figure 2.3.

Once the mass surface density of a region is known in units of g cm^{-2}, we convert it to a hydrogen column density via

$$N_{\rm H} = \frac{\Sigma}{\mu_{\rm H}} \quad ({\rm cm}^{-2}) \tag{2.1}$$

where $\mu_{\rm H} = 1.4 m_{\rm H} = 2.34 \times 10^{-24}$ g, i.e., assuming $n_{\rm He} = 0.4 n_{\rm H}$ and assuming that the contribution from the additional species to the total mass is so minor that it can be neglected. The chemical abundance of various species will be expressed in terms of an abundance relative to that of H nuclei. For constant dust properties, the visual extinction is proportional to $N_{\rm H}$ Kainulainen & Tan (2013).

$$A_V = \frac{N_{\rm H}}{1.9 \times 10^{21}\ {\rm cm}^{-2}} \,({\rm mag}) \tag{2.2}$$

The values of visual extinction of the regions in the IRDC are needed when compared to the parameters of astrochemical models.

In our analysis, we require an estimate of N_H toward single regions across the maps. The minimum aperture possible to extract single region information is dictated by the poorest angular resolution in our data i.e., 16″ radius corresponding to the beam size of the $HC^{18}O^+$(1-0) specie (see Table 2.1). From this 2D aperture, we assume that the material within a single region is uniformly distributed in a sphere of radius 16″.

Given the distance to Cloud G is 2.9 kpc Rathborne et al. (2006), the radius of these apertures is 0.225 pc. Therefore, n_{H} is given by

$$n_{\mathrm{H}} = N_{\mathrm{H}} \frac{\pi r^2}{4\pi r^3/3} = \frac{3}{4r} N_{\mathrm{H}}. \tag{2.3}$$

Finally, we estimate the free-fall time, which in our case is the time required for a molecular cloud to collapse due to self-gravity in the absence of an internal outward pressure.

$$t_{\mathrm{ff}} = \sqrt{\frac{3\pi}{32 G n_{\mathrm{H}} \mu_{\mathrm{H}}}}, \tag{2.4}$$

where G is the gravitational constant and the normalization constant is that for the idealized case of a uniform sphere.

All these datasets and analysis methods will be applied in the next chapter to study the kinematics, CO depletion, and dynamics of Cloud G.

3

Results

In the following chapter, we first present the result of our analysis of the ^{13}CO(1-0) and C^{18}O(1-0) emission across the IRDC G034.77-00.55, such as the average spectra for the whole cloud and positions 1-6, as well as a noise estimation. We furthermore present the result of the kinematical and dynamical analysis of Cloud G. We also present the final CO depletion factor maps for the different cases and how the depletion factor varies against physical properties such as dust temperature and mass surface density. Finally, with the observations of molecular rotational transitions collected using the GBT and the additional molecules collected with the IRAm-30m we estimate the CRIR and chemical age of Cloud G through means of comparing the observed abundances to those predicted by models.

3.1 The ^{13}CO(1-0) and C^{18}O(1-0) emission across the IRDC G034.77-00.55

From the GBT observations, we obtain three-dimensional (position-position-velocity; PPV) cubes in FITS (flexible image transfer system) format for the molecular lines, of ^{13}CO(1-0) and C^{18}O(1-0). The total average spectrum is thus obtained by summing the spectrum of every pixel in an image and dividing by the number of pixels for each individual image (pixels lacking good data, i.e., with a NaN value, are excluded and do not contribute to the sum). For each of the CO isotopologues, we have extracted the average spectrum across the map and these are shown in Figure 3.1.

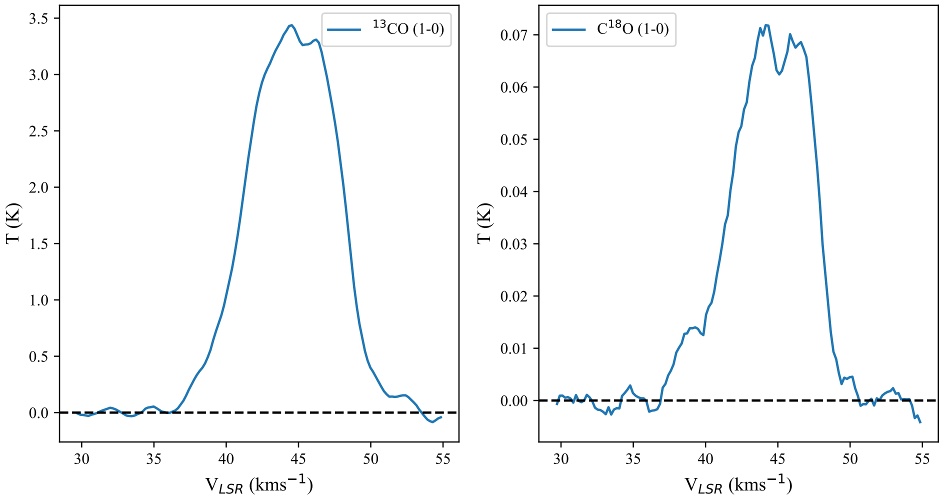

Figure 3.1: The average spectra of the ^{13}CO(1-0) and C^{18}O(1-0) line emission. The chosen integration range is shown with black dashed lines in each subplot in the figure.

Spectra of the different molecules were obtained for 6 distinct positions toward cloud G, in order to identify the velocity range in which the line is present and that will be used to obtain integrated intensity maps. The independent regions were selected based on their relatively high mass surface density values compared to the rest of the cloud. Positions 1,2 and 4 are also known to host cold cores (Rathborne et al. (2006)). In order to extract spectra toward the six positions a beam aperture of 16″ was used. The ^{13}CO(1-0) and C^{18}O(1-0) spectra of the distinct regions are shown in Figure 3.2. From the figure, we observe that the emission extends over a velocity range from 36 km/s to 52.6 km/s (88 channels). Hence, we consider this range to obtain integrated intensity maps of the two species.

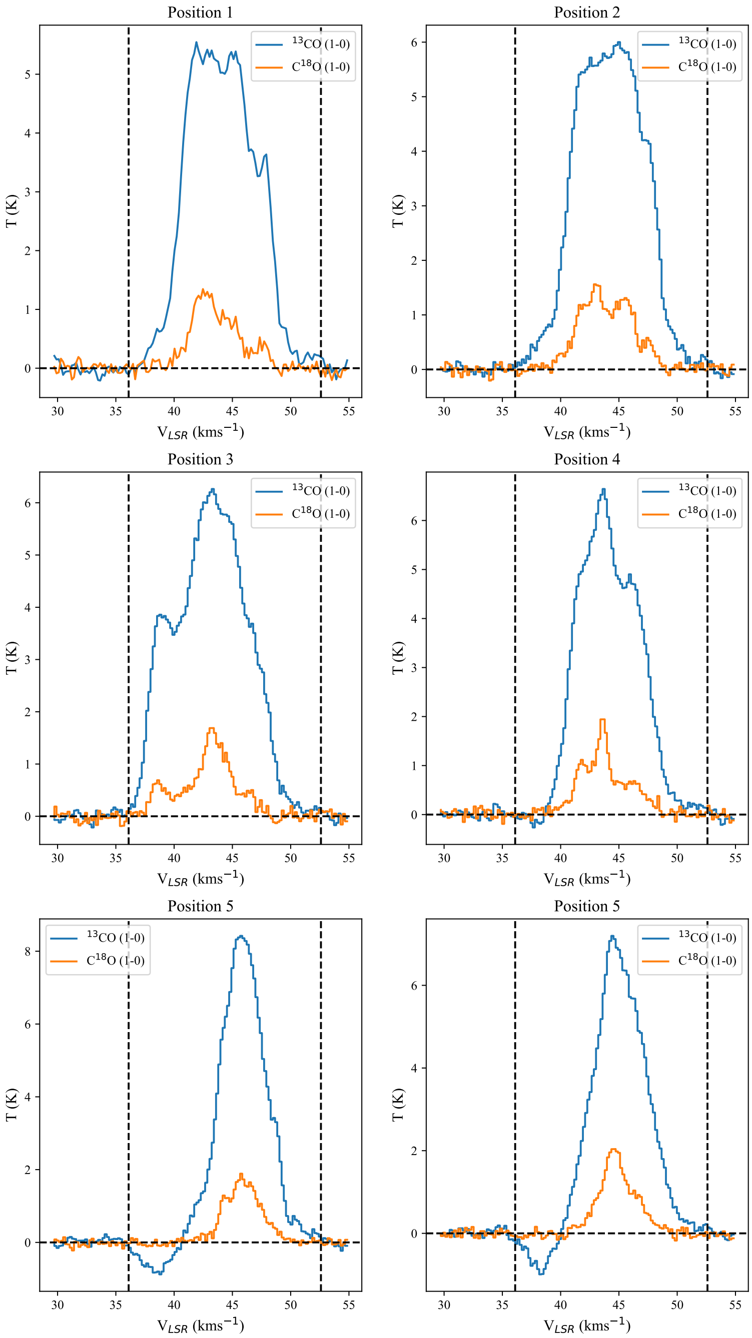

Figure 3.2: The corresponding spectra to the distinct observed regions from the GBT data. The chosen integration range is shown with black dashed lines in each subplot in the figure.

The noise level in the obtained spectra was determined by calculating the root mean square (RMS) of the portion of the spectrum that is free from emission lines, i.e. 29.7 km/s-35.0 km/s (28 channels). The area of the RMS noise was determined according to equation 3.1.

$$A_{RMS} = RMS\sqrt{n}\,dv \tag{3.1}$$

by multiplying the RMS noise level with the square root of the number of channels used to estimate the rms and the respective velocity resolution, in order to estimate a cut-off point for the integrated intensity maps.

The RMS noise level for the ^{13}CO and C^{18}O are illustrated in Figure 3.3.

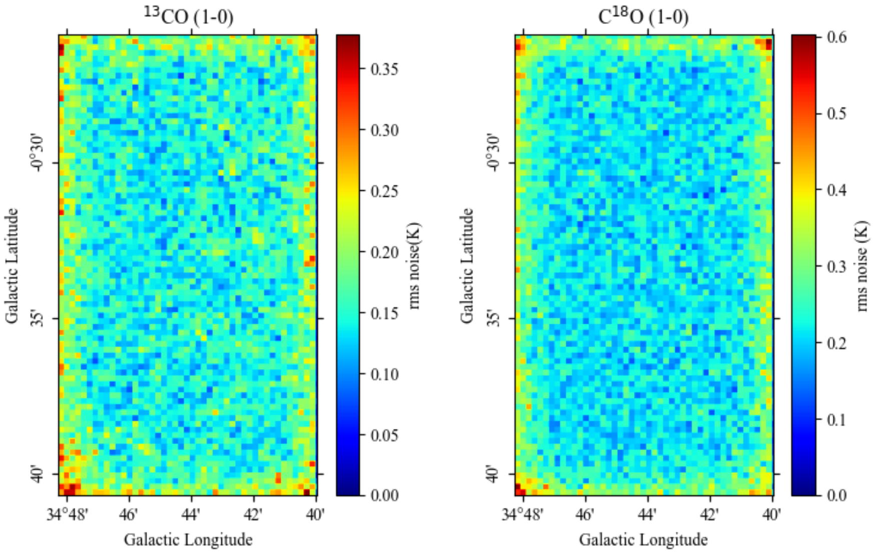

Figure 3.3: RMS noise level for ^{13}CO(1-0) (left figure) and C^{18}O(1-0) (right figure) was determined as the root mean square of the portion of the spectrum that is free from emission lines, ranging from 29.7 km/s to 35.0 km/s (28 channels).

In our case, everything below one time the integrated RMS was regarded as noise and was therefore excluded. The integrated RMS level for the ^{13}CO and C^{18}O are show in Figure 3.4.

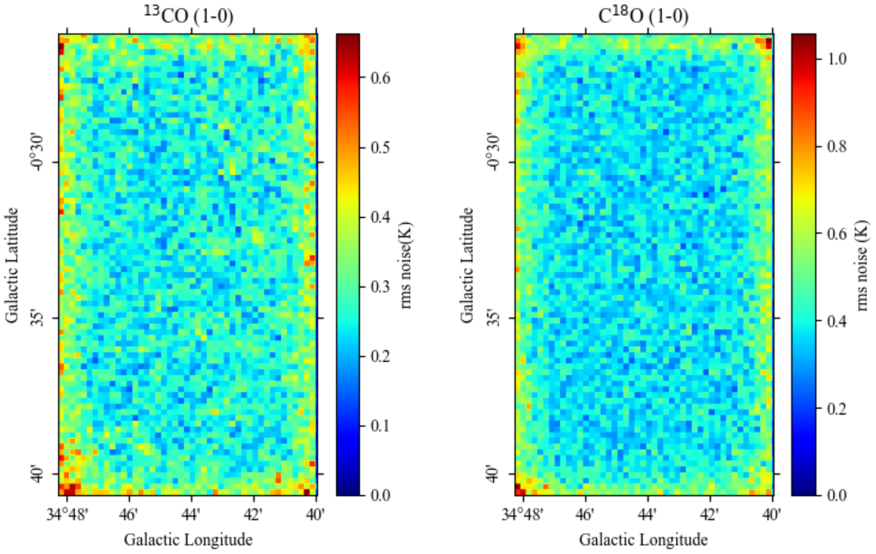

Figure 3.4: The integrated noise for ^{13}CO(1-0) (left figure) and C^{18}O(1-0). The RMS noise given in Figure 3.3 was multiplied by the velocity difference (see Table 2.1) and the square root of 28 channels.

The integrated noise was also estimated by simply integrating over the line-free region, 29.7 km/s-35.0 km/s (28 channels). The resulting maps of the integrated noise are illustrated in Figure 3.5.

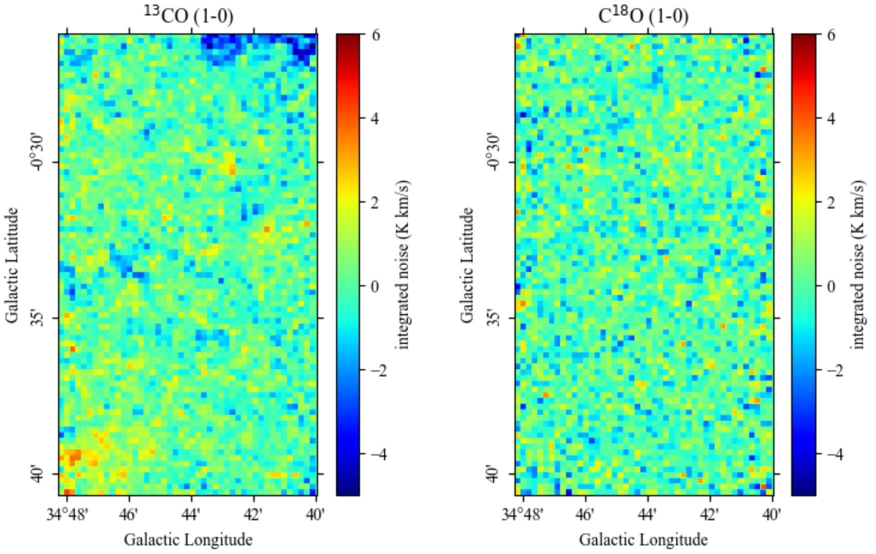

Figure 3.5: The integrated noise for ^{13}CO(1-0) (left figure) and C^{18}O(1-0) obtained by integrating over the line free region 29.7 km/s-35.0 km/s

In order to compare the integrated noise obtained from the different methods, we estimate the dispersion of the integrated noise in Figure 3.5. The dispersion towards the center of the map was estimated to equal 0.27 K km/s for ^{13}CO and 0.29 K km/s for C^{18}O. These values were then compared to the average values for the integrated noise in Figure 3.4, which was estimated to be 0.14 for ^{13}CO and 0.21 for C^{18}O respectively.

When subtracting the noise from the integrated intensity maps, the integrated noise was scaled by a factor of 88/28, seeing as we only calculated it for 28 channels, while we integrate over 88 channels for the integrated intensity maps.

The integrated intensity maps from the GBT data for ^{13}CO(1-0) and C^{18}O(1-0) are shown in Figure 3.6. The positions of interest mentioned previously in the method, are depicted by black circles. The 0.1 g cm^{-2} level (white contour) from the KT13 map is superimposed on the integrated intensity maps.

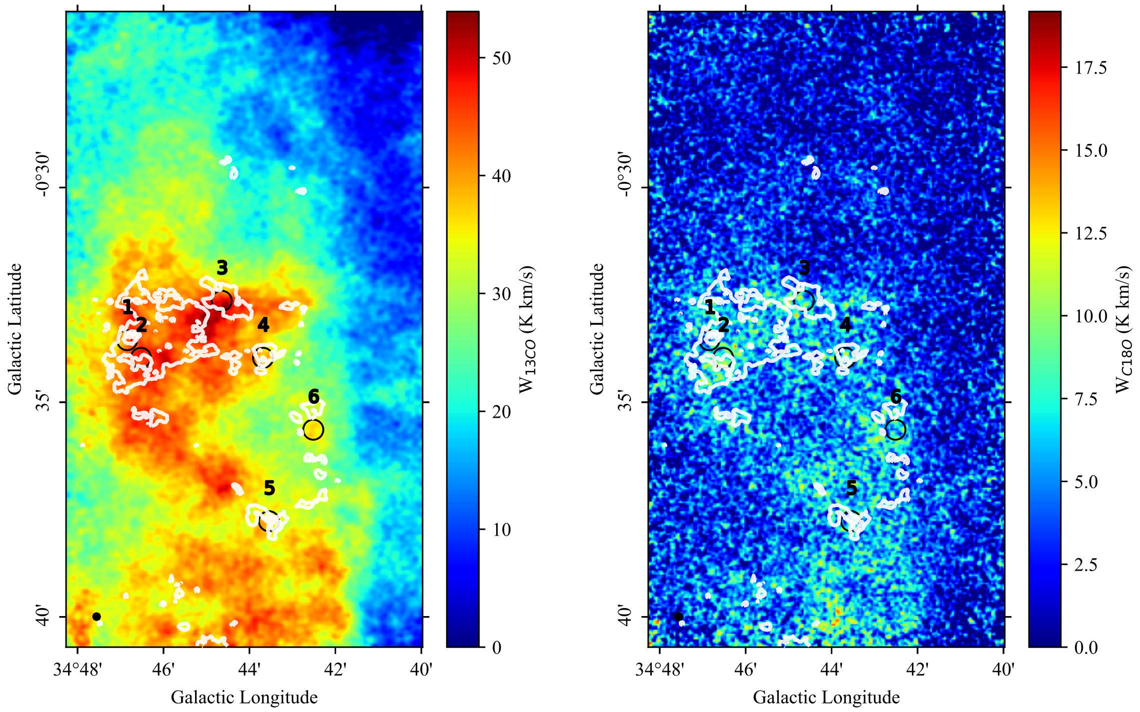

Figure 3.6: The full resolution integrated intensity maps of Cloud G based on the GBT data. *(a) Left:* The integrated intensity of ^{13}CO(1-0), with the six selected positions marked with black circles. *(b) Right:* As (a), but for C^{18}O(1-0).

The features were more feasible to differentiate for the moment 0 map of C^{18}O one could clearly observe the ring formation. However, the map for C^{18}O appears more grainy, showing regions sometimes smaller than the beam size with a dip or rise in integrated intensity that differs from the surroundings.

3.2 Kinematics of the ^{13}CO and C^{18}O emission gas

As seen in Figure 3.2, both the ^{13}CO and C^{18}O (1-0) emissions show multiple velocity peaks and variations in the line central velocities across the different positions.

All this indicates the presence of a complex kinematic structure toward the cloud. In order to investigate these gas kinematics, channel maps were created of both molecules with the intention to further study the structure in Cloud G. The overall ring formation of Cloud G can be seen present in Figures A.11 and A.12. The dense region in the upper part of the ring structure and the bar next to it seem to correlate to where the emissions of ^{13}CO and C^{18}O are detected. The dense warm core found in the Σ_{GG} and Σ_{SMF} maps, can also be detected in the channel maps, especially in the case of C^{18}O. Figure A.11 and Figure A.12 also show that the brightest emissions observed in the channel maps were found south-east of the ring structure in the velocity range $\sim 44.5 - 48$ km/s.

The moment 1 and moment 2 maps of Cloud G are presented in Figure 3.7. The moment 1 map, shows an intensity-weighted velocity, otherwise known as a velocity field. The moment 2 map, on the other hand, shows an intensity-weighted dispersion. These maps were derived according to the equations in equation 3.2. A line width map was obtained by taking the square root of the moment 2 map, $\sigma = \sqrt{M_2}$.

$$M_1 = \frac{\int v \cdot T_{mb} dv}{\int T_{mb} dv} \approx \frac{\sum_i v_i \cdot T_{mb,i}}{\sum_i T_{mb,i}}, \quad M_2 = \frac{\int T_{mb}(v - M_1)^2 dv}{\int T_{mb} dv} \approx \frac{\sum_i T_{mb,i}(v_i - M_1)^2}{\sum_i T_{mb,i}} \tag{3.2}$$

In both moment 1 maps the intensity-weighted velocity is greater towards the southwest corner of the image compared to the mean velocity of the cloud and slightly smaller in the northeast corner. On average, the intensity-weighted velocity is around 46 km/s for the southwest region and 42-43 km/s for the northeast region. The extreme dark spots in the moment 1 maps towards the northeast are disregarded since the corresponding pixels in the moment 0 map show an absence of emission. This could possibly indicate that the region towards the HII region in the southwest direction is red-shifted and the region towards the supernova remnant is blue-shifted in comparison to the cloud's mean velocity of 43.5 km/s. This could insinuate that the SNR lies farther away from us than Cloud G. The HII region would therefore be located closer to the observer using the same reasoning. The moment 1 map could therefore possibly advocate for the geometrical structure regarding the relative locations of Cloud G, the HII region, and the supernova remnant.

The upper part of the ring structure shows an average width of 2-2.5 km/s for the ^{13}CO line emission and around 1.5-2 km/s for C^{18}O based on the molecules respective moment 2 maps. The same region that showed higher values from the moment 1 map had a slightly lower intensity weighted dispersion compared to the rest of the cloud. Moreover, the intensity weighted dispersion for ^{13}CO seems to be elevated in the north-east direction, this elevation could not be distinguished for the C^{18}O. The regions surrounding position 5 and the warm dense core, show a decline in the value of the velocity dispersion.

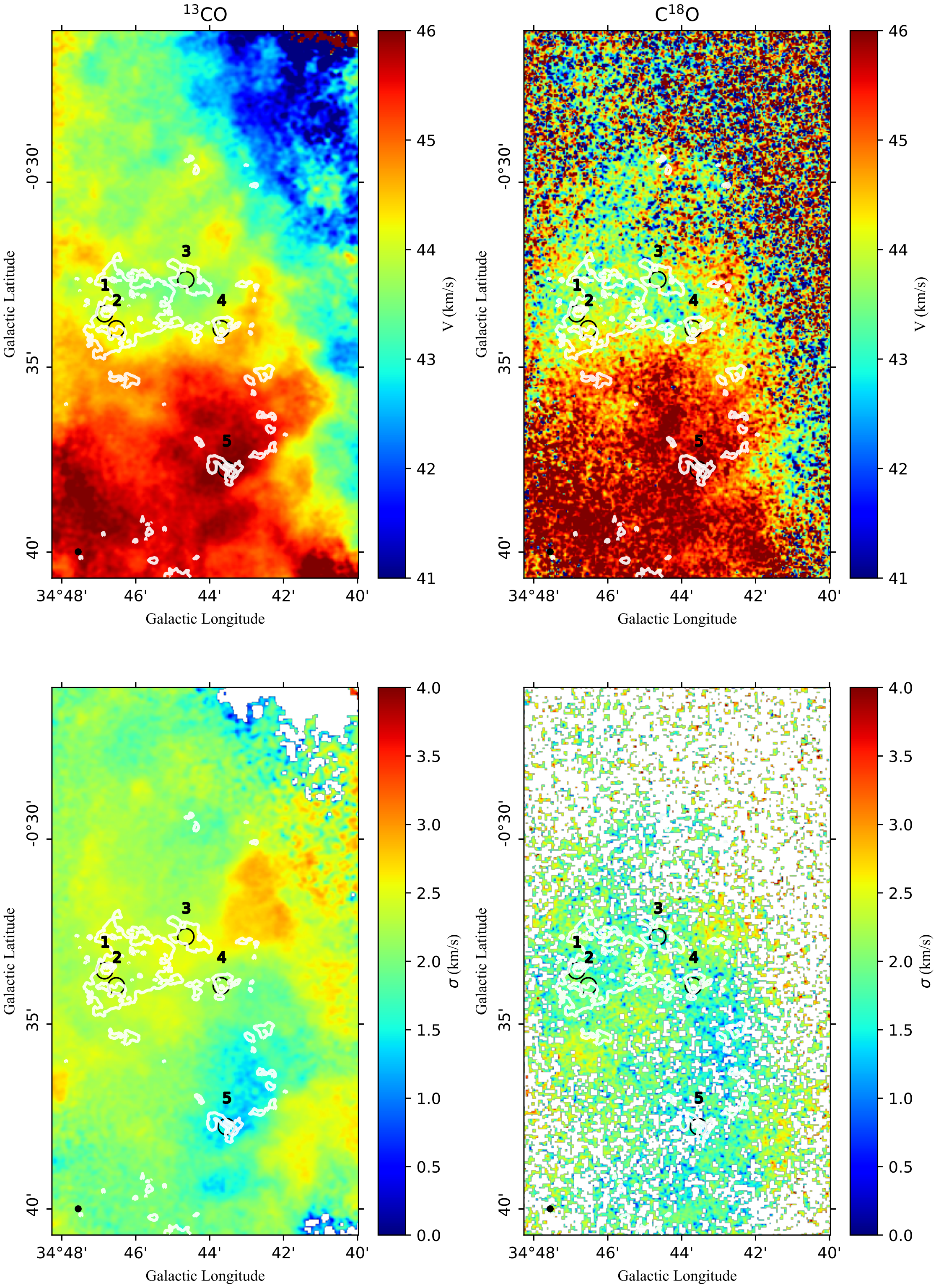

Figure 3.7: Top row: Intensity weighted velocity. Bottom row: Intensity weighted dispersion. Σ_{KT13} is superimposed on top of the moment maps as white contour lines.

Table 3.1: Show the values of the moment 1 and moment 2 map for the six distinct positions

Position	1	2	3	4	5	6
V_{13CO} (km/s)	44.08	44.25	43.62	44.17	45.92	45.10
V_{C18O} (km/s)	43.72	44.08	43.63	43.98	45.90	44.91
σ_{13CO} (km/s)	2.38	2.35	2.45	2.19	1.4	1.76
σ_{C18O} (km/s)	1.84	1.91	1.59	1.81	1.28	1.36

3.3 CO depletion

Firstly, the molecular column density was determined for each molecule, which is expressed as the number of molecules per unit of area integrated along the line of sight between the observer and the source. Assuming that the line is optically thin and that the excitation temperature remains the same regardless of which rotational level is observed, the column density is then given by equation A4 from Caselli et al. (2002):

$$N = \frac{8\pi}{A\lambda^3 g_u} Q_{rot}(T_{ex}) \frac{1}{J_\nu(T_{ex} - J_\nu(T_{bg})} \frac{exp(-E_l/k_B T_{ex})}{1 - exp(-h\nu/k_B T_{ex})} \int T_{mb}\, d\nu, \tag{3.3}$$

where h and k_B are the Planck and Boltzmann constant respectively. ν and λ are the corresponding rest frequency and wavelength of the observed transition for a specific molecule. The Einstein coefficient related to the rate of spontaneous emission of light is denoted as A. g is the statistical weight, while E is the energy of the state, and the down-cased indices u and l in the column density equation refer to the upper and lower levels. The formula relating g_u to the rotational quantum number is given as $g_u = 2J + 1$. The integral is simply the integrated intensity. The excitation temperature, T_{ex} was assumed to be 7.5 K, a common assumption for IRDCs (e.g., Hernandez et al. (2011), Hernandez & Tan (2015), Entekhabi et al. (2021)). The excitation temperature was derived for Cloud G in Cosentino et al. (2018) and was found to range from range 6–11 K. The background temperature of the Cosmic Microwave Background (CMB) is $T_{bg} = 2.73$. The brightness temperature, $J_\nu(T)$ is defined as follows

$$J_\nu(T) = \frac{h\nu}{k_B} \frac{1}{exp(h\nu/k_B T) - 1}. \tag{3.4}$$

The rotational partition function, Q_{rot} is expressed as

$$Q_{\mathrm{rot}}(T_{\mathrm{ex}}) = \sum_{J=0}^{\infty} (2J+1)\mathrm{exp}(-E_J/k_B T_{\mathrm{ex}}), \quad \text{where} \quad E_J = J(J+1)hB, \tag{3.5}$$

where B is the rotational constant.

When estimating Q_{rot} for the different molecules, the infinite sum was treated as a finite sum, where the upper bound of the sum was set to a finite number based on a value of Q_{rot} converging.

The values for the different partition functions are shown in the table 3.2. Values of the rest frequencies, Einstein A coefficient, rotational constant, and the energy of the lower state were all obtained through the Molecular Spectroscopy Jet Propulsion Laboratory (JPL) catalog. All of the spectroscopic information of the observed transitions are given in table 3.2.

Table 3.2: Spectroscopic information such as the observed molecular transitions, rest frequencies, Einstein A coefficients, rotational constants, the energy of the lower state, degeneracy of the upper state, as well as the estimated partition function.

Species	$J_u - J_l$	ν (MHz)	$log_{10}A$ (s^{-1})	B_0 (MHz)	E_L (K)	g_u	Q_{rot}
^{13}CO	(1-0)	110201.3543	-7.19843	55101.011	0.00	3	3.195
C^{18}O	(1-0)	109782.1734	-7.20302	54891.420	0.00	3	3.205

In Figure 3.8, we present the column density map of both CO isotopologues as well as the ratio between the molecules. The ratio values alongside the ring structure are found to range from 4 to 9 in general, with the exception of a handful of pixels that depict significantly greater ratio values of 14. This is a product of the graininess nature of the integrated intensity map of C^{18}O. Another exception is that the ratio values for warm dense core were found to be slightly lower than the rest of Cloud G (a value of 3). One could speculate that for the regions with a lower ratio value, it is plausible that the line emission of ^{13}CO is optically thick, and the column density of ^{13}CO is underestimated. The region surrounding Cloud G displays greater ratio values, because of the lack of C^{18}O seeing as C^{18}O is a dense gas tracer. We present in Figure 3.9 how the column density ratio relates to the C^{18}O column density. We can observe that the ratio decreases as the column density of C^{18}O increases.

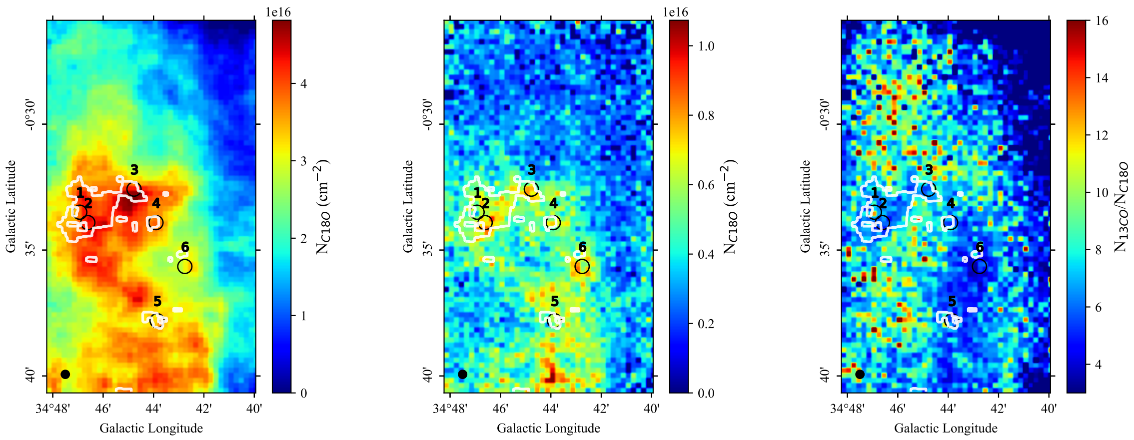

Figure 3.8: A map illustrating the ratio between the column densities of ^{13}CO(1-0) and C^{18}O(1-0) (regridded to the Herschel mass surface density maps with additional smoothing; pixel size of 12″) of Cloud G with the six distinct positions marked with labeled black circles.

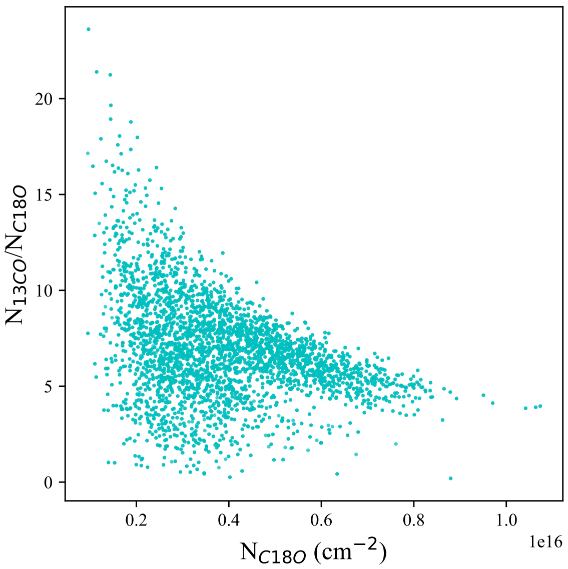

Figure 3.9: The column density ratio ($N^{13/18}$) scattered against the column density of C^{18}O(1-0) (See Figure 3.8 and the column density in Figure 3.11 for reference).

The molecular abundance is expressed as a ratio between the column density of a species and the column density of hydrogen nuclei. In order to obtain an abundance map, one first needs to ensure that the column density map and the mass surface density map share a common fits header. This is achieved by using the map with the worse resolution as a template and reprojecting the other map. The Herschel mass surface density maps for example have a lower resolution than the integrated intensity maps, and the opposite is true for the Kainulainen-Tan mass surface density map. The maps obtained from the C^{18}O(1-0) line emission were smoothened out further, by determining the average of regions consisting of four pixels, in order to decrease the graininess of the map and decrease the number of nan pixels.

At the typical conditions of density and temperature of IRDCs, the abundances of certain molecules in the gas phase are depleted onto interstellar dust grains. The CO depletion factor is defined as

$$f_D = \frac{X(CO)_{\text{exp}}}{X(CO)_{\text{obs}}} \tag{3.6}$$

where $X(CO)_{\text{obs}}$ and $X(CO)_{\text{exp}}$ are the measured CO abundance and the expected CO abundance (if all of the carbon present is in a gas phase) respectively. $X(CO)_{\text{exp}} = 1.4 \cdot 10^{-4}$ was assumed (Lacy et al. (1994)).

$$X(CO) = I\frac{N(\text{species})}{N_H} \tag{3.7}$$

where I is the isotopic ratio between the common $^{12}C^{16}O$ and the molecule in question. For $^{12}C/^{13}C$, the isotopic ration is 49.8 (Zeng et al. (2017)) and for $^{16}O/^{18}O$ it is 327 (Wilson & Rood (1994)). Both ^{13}CO and $C^{18}O$ were converted to CO by multiplying with their respective isotopologue ratios.

The estimated abundance and depletion factor come with a degree of uncertainty. The method in which these uncertainties were estimated follows that of Entekhabi et al. (2021). The first uncertainty arose in connection with the noise level for the spectra and was set to equal the integrated noise level. The second source of uncertainty came from the assumption that the excitation temperature was 7.5 K and just like in Entekhabi et al. (2021), the excitation temperature was varied by ±30% to determine the effect on the column density. The column density was, therefore, estimated for both 5.25 K and 9.75 K, and in both cases, the column densities were compared to those of 7.5 K. On average the column densities varied around 7-18 %.

When estimating the abundances, the systematic uncertainties of the Σ-maps were also taken into account, which was estimated to be $\sim 30\%$ (Kainulainen & Tan (2013), Lim et al. (2016)). For CO, the uncertainty from the isotopic ratio was also included, assuming an uncertainty of around 20%. The final uncertainty was estimated by summing all of the individual uncertainties in a quadrature for each molecule.

One of the project's goals was to create a high-resolution CO depletion map based on the GBT data. This was achieved and presented in Figures 3.10 to 3.15. The figures are displayed in the same manner.

The general shape of the mass surface density map in Figures 3.10, 3.12 and 3.14 can be observed in the abundance map and is therefore also reflected in the depletion map. All of the positions of interest show signs of high depletion factor values. However, the warm dense core, the upper part of the ring structure, and the region surrounding position 5, all show particularly high depletion values compared to the rest of the map. One explanation for the high depletion value in the core is due to it being a dense region, around $\Sigma_{GG} \sim 0.2$ g cm^{-2}, resulting in the column density of atomic hydrogen being $8 \cdot 10^{22}$ cm^{-2}.

Furthermore, Figures 3.10 and 3.14 also show an elevated depletion factor towards the northeast part of the map. Notice that in both of these regions mentioned, the temperature was above 30 K, which is a deviation from the usual trend, where the depletion factor decreases as the temperature increases. The high depletion factor can therefore not be explained by the freeze-out process of CO, but rather as the result of a lack of ^{13}CO emission in the region. The carbon might instead be found in another form.

Looking at the Figures derived from C^{18}O, (see Figures 3.11, 3.13 and 3.15), we notice that the "graininess" of the integrated intensity map is also present in the depletion maps beside the general shape of the mass surface density map.

Table 3.3 summarizes the average depletion factor extracted from the marked positions from all of the depletion maps with a pixel size of $6''$ for the instance of ^{13}CO and $12''$ for C^{18}O. The motivation behind the choice of only including these maps was to ensure that we are studying the exact same region in every depletion map. Based on the table, one can observe that the highest depletion value of ^{13}CO originated from the warm dense core, while for the instance of C^{18}O, the highest value was found in the upper part of the ring structure in addition to the warm dense core. The depletion factor values marked in table 3.3 derived from ^{13}CO show slightly higher values than those derived from C^{18}O, with the exception of position 1. We can observe that Position 1 contains a small region with a depletion factor value much higher than its near surrounding. This could be a direct product of the grainy/speckle nature of the moment 0 map.

An additional trend in table 3.3 is that values of the depletion factor derived from Σ_{SMF} appear to be larger towards the upper part of the ring structure and lower elsewhere compared to the corresponding depletion values from Σ_{GG}. Σ_{KT13} however, shows significantly higher f_D values, as a direct result of the mass surface density map being almost twice as dense. Since the warm dense region was removed in the Σ_{KT13} map, it is therefore not present in the corresponding depletion maps, nor in Table 3.3.

Position	**GG**		**SMF**		**KT13**	
	^{13}CO (6″)	C^{18}O (12″)	^{13}CO (6″)	C^{18}O (12″)	^{13}CO (6″)	C^{18}O (12″)
1	3.02	3.45	3.35	3.81	6.11	6.80
2	2.70	2.38	2.8	2.47	5.41	4.67
3	1.84	1.75	1.71	1.62	3.73	3.50
4	2.02	1.99	1.67	1.63	3.49	3.43
5	3.04	2.93	2.42	2.27	4.6	4.37
6	5.73	3.85	4.90	3.28	-	-

Table 3.3: Collection of the average depletion factor value for the positions 1-6. For a simpler comparison, the f_d values for ^{13}CO were all obtained from the depletion maps with a pixel size of 6″ (see Figures 3.10, 3.12 and KT13 6″ in appendix). The depletion values for C^{18}O were obtained from the depletion maps with a pixel size of 12″ (see Figures 3.11, 3.13 and KT13 6″ in appendix).

Figures 3.16 and 3.17 show an in-zoomed version of the depletion maps in Figures 3.10-3.15, focusing solely on the northern region of Cloud G (the same region that was enclosed in the ellipse (Simon et al. (2006a), Kainulainen & Tan (2013)).

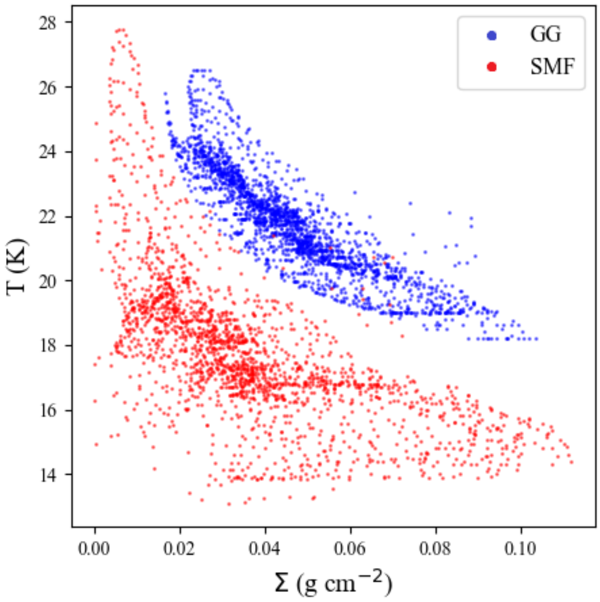

Figure 3.19: Scatter plot of the dust temperature against the mass surface density.

For each scatterplot, the x-axis was divided into smaller subsections where the average of the values was determined and reported in Figure 3.20.

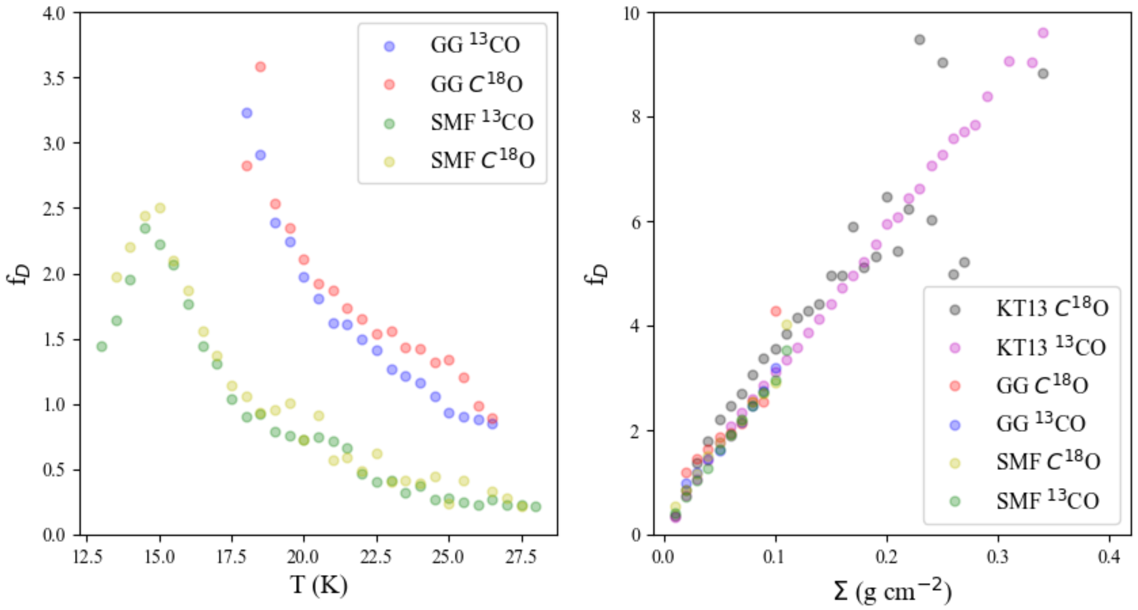

Figure 3.20: Scatter plot of the depletion factor against either the dust temperature (left panel) or the mass surface density (right panel). The different colors in the scatterplot show the different combinations used, stating whether the depletion values were derived from the ^{13}CO emission or the C^{18}O or which mass surface density map was utilized.

In order to illustrate how the depletion factor varies depending on the temperature and mass surface density, scatter plots were created (see Figure 3.18). One can clearly discern that the f_D decreases for higher temperatures and increases for greater density values. The f_D values derived from the ^{13}CO and C^{18}O appear to be quite similar for each case. The CO depletion factor for Cloud G was found to range from 1.5-6 for the instance where it is derived from Σ_{GG} or Σ_{SMF}, and the values are up to twice as large when they are derived from Σ_{KT13}. The depletion factors in the right panel of Figure 3.20 are arranged in a neat lineup for ^{13}CO with little dispersion. This is another indication that the depletion map is a reflection of the mass surface density map, implying that the variation in the ^{13}CO column density map was not great enough to influence the resulting depletion map. The scatter plot for C^{18}O appears more scattered (has a more significant dispersion) and could be noise dominated, due to the presence of greater variations/strong features in the column density.

In the left panel of Figure 3.18, the f_D values appear to be reasonably similar in size regardless of which density map was used to derive the depletion values. The main difference between the f_D values is that those derived from the Σ_{GG} appear to be shifted to the right by roughly 4 K, a product due to the fact that T_{SMF} is in general colder than T_{GG}. Other than that, both cases illustrate the same relation between the dust temperature and mass surface density, mainly how the denser regions of

Cloud G correspond to colder regions (see Figure 3.19). The lowest temperatures in T_{SMF} in Figure 3.16 are located towards the upper left corner (close to the edge of the observed part of Cloud G) of the map rather than at the densest regions. The region with the greatest f_D derived from Σ_{SMF} was found to have a corresponding dust temperature of 15 K in Figure 3.20. The left panel in Figure 3.20 shows an increasing trend for temperatures less than 15 K and a decreasing trend everywhere elsewhere.

We can also note that the region with the highest f_D derived from the KT13 mass surface density map, also appears as a dark spot in the integrated intensity map. The dark dips in the moment 0 map of $\mathrm{C^{18}O}$ could be proven to be an obstacle, as they can be observed to intensify/overestimate the f_D values. The same goes for the rest of the depletion factor maps derived from the $\mathrm{C^{18}O}$.

Another thing worth noting is that some of the depletion factors values fall below 1. A depletion factor of a value below 1 would indicate that the observed abundance of CO gas is greater than the expected abundance if all of the carbon present is in the gas phase, which is contradictory. This could be a consequence of the uncertainties associated with the CO depletion values as estimated above. The values above 1 are associated with the colder denser regions. The f_D values from the scatter plots for the different cases fall below 1 at different temperatures and densities depending on which molecule was observed, and which temperature and mass surface density map was used. We, therefore, normalized all depletion factor values below 1, by multiplying the said values with a scalar so that the resulting depletion value would equal unity, each subinterval in the binned scatterplot had a unique scalar. Figures 3.21 and 3.22 shows Figures 3.16 and 3.17 after normalization. We can observe that the region surrounding the upper clump shows no signs of depletion in the instance of SMF compared to GG and KT13. The regions that are depleted for SMF are constrained to regions with a temperature below 17.5 K (see Figure 3.23).

3.4 Virial Analysis

We performed a mass calculation for all three mass surface density maps, resulting in three different mass estimates for positions 1-4 that are reported in Table 3.4.

We furthermore estimated the virial parameter as follows:

$$\alpha_{\mathrm{vir}} = \frac{M\sigma_{\mathrm{3D}}^2}{3GM^2/5R} = \frac{5R\sigma_{\mathrm{1D}}^2}{GM}. \tag{3.8}$$

Since the velocity dispersion and radius of the considered regions are dictated by the beam size and the velocity molecular spectra, the only factor that affects the virial parameter is the mass estimate. For this, we used the mass surface maps obtained with the Herschel and KT13 methods. While the GG and SMF Herschel maps lead to similar mass estimates, the KT13 maps lead to mass estimates that are a factor of two larger. This is probably due to the method used to estimate the mass surface density. The estimated virial parameters from Table 3.4 are illustrated in Figure 3.24 as scattered points. Σ_{GG}, Σ_{SMF}, and Σ_{KT13} are represented by the colors red, blue, and green respectively. ^{13}CO and C^{18}O are represented by a circular shaped marker and a triangle shape marker. Each set consisted of four points, corresponding to the four regions in the upper region of the ring structure. Furthermore, a polynomial of the first order was fitted to the scattered data points for each set, to further illustrate a correlation between the mass and virial parameter. The lines are either dashed or dotted depending on what molecule was used.

The derived virial parameters all hint toward the idea that the four chosen regions are all gravitationally unbounded. Moreover, the virial parameter for the whole cloud was estimated to be around 4.7 in Tan et al. (2013). All of the fitted lines show a negative correlation in Figure 3.24. Regions with a greater mass tended to have a lower virial parameter and could thereby be considered gravitationally bound.

In the case of KT13, the slope of the lines is approximately 3.3 times smaller than that of GG and 4.3 smaller than that of SMF, indicating a weaker, negative correlation between the virial parameter and the mass. The deviation from scattered points to the fitted line is smaller for ^{13}CO than those for C^{18}O, where the values from regions 3 and 4 seem to be more scattered. However, one would have to include more points than simply four before drawing a conclusion, to ensure that the result is reliable.

Furthermore, the total velocity contribution was separated into thermal, σ_T, and non-thermal contributions, σ_{NT}, that were calculated according to Jiménez-Serra et al. (2014);

$$\sigma_{NT} = \sqrt{\frac{\Delta\nu_{obs}^2}{8ln(2)} - \frac{k_B T_{kin}}{m_{obs}}} \qquad \sigma_T = \sqrt{(\sigma_{obs})^2 - (\sigma_{NT})^2} \tag{3.9}$$

we assumed a kinetic temperature of 15 K. $\Delta\nu_{obs}$ is the observed line width. m_{obs} is the mass of the observed molecule (29 a.m.u for ^{13}CO and 30 a.m.u for C^{18}O).

Virial parameters derived from solely the thermal contribution also insinuate that the four chosen regions are all gravitationally unbounded.

Table 3.4: Collection of properties for positions 1-4 in the northern region, such as the mass surface density, the mass, velocity dispersion squared for both ^{13}CO and C^{18}O and the virial parameters.

Parameter	GG				SMF				KT13			
Position	1	2	3	4	1	2	3	4	1	2	3	4
Σ (gcm^{-2})	0.094	0.084	0.064	0.059	0.088	0.093	0.062	0.52	0.168	0.197	0.122	0.108
Mass $M_\odot$	71.31	63.67	48.46	44.58	66.60	70.55	47.16	39.92	127.64	150.19	92.81	82.04
Total contribution												
σ_{13CO} (km/s)	2.38	2.35	2.45	2.19	2.38	2.35	2.45	2.19	2.38	2.35	2.45	2.19
σ_{C18O} (km/s)	1.84	1.91	1.59	1.81	1.84	1.91	1.59	1.81	1.84	1.91	1.59	1.81
α_{vir} ^{13}CO	20.77	22.76	32.30	28.20	22.24	20.54	33.18	31.49	11.61	9.65	16.86	15.32
α_{vir} C^{18}O	12.39	15.26	13.35	20.03	13.27	13.77	13.72	22.37	6.92	6.47	6.97	10.89
Non-thermal contribution												
σ_{13CO} (km/s)	1.01	1.00	1.04	0.93	1.01	1.00	1.04	0.93	1.01	1.00	1.04	0.93
σ_{C18O} (km/s)	0.78	0.82	0.67	0.78	0.78	0.82	0.67	0.78	0.78	0.82	0.67	0.78
α_{vir} ^{13}CO	3.75	4.10	5.82	5.08	4.01	3.7	5.98	5.68	2.09	1.74	3.04	2.76
α_{vir} C^{18}O	2.23	2.75	2.41	3.61	2.39	2.48	2.47	4.03	1.25	1.17	1.26	1.96
Thermal contribution												
σ_{13CO} (km/s)	2.15	2.13	2.21	1.99	2.15	2.13	2.21	1.99	2.15	2.13	2.21	1.99
σ_{C18O} (km/s)	1.66	1.75	1.42	1.67	1.66	1.75	1.42	1.67	1.66	1.75	1.42	1.67
α_{vir} ^{13}CO	17.03	18.66	26.47	23.12	18.23	16.84	27.20	25.81	9.51	7.91	13.82	12.56
α_{vir} C^{18}O	10.16	12.51	10.94	16.42	10.87	11.29	11.24	18.34	5.67	5.30	5.71	8.92

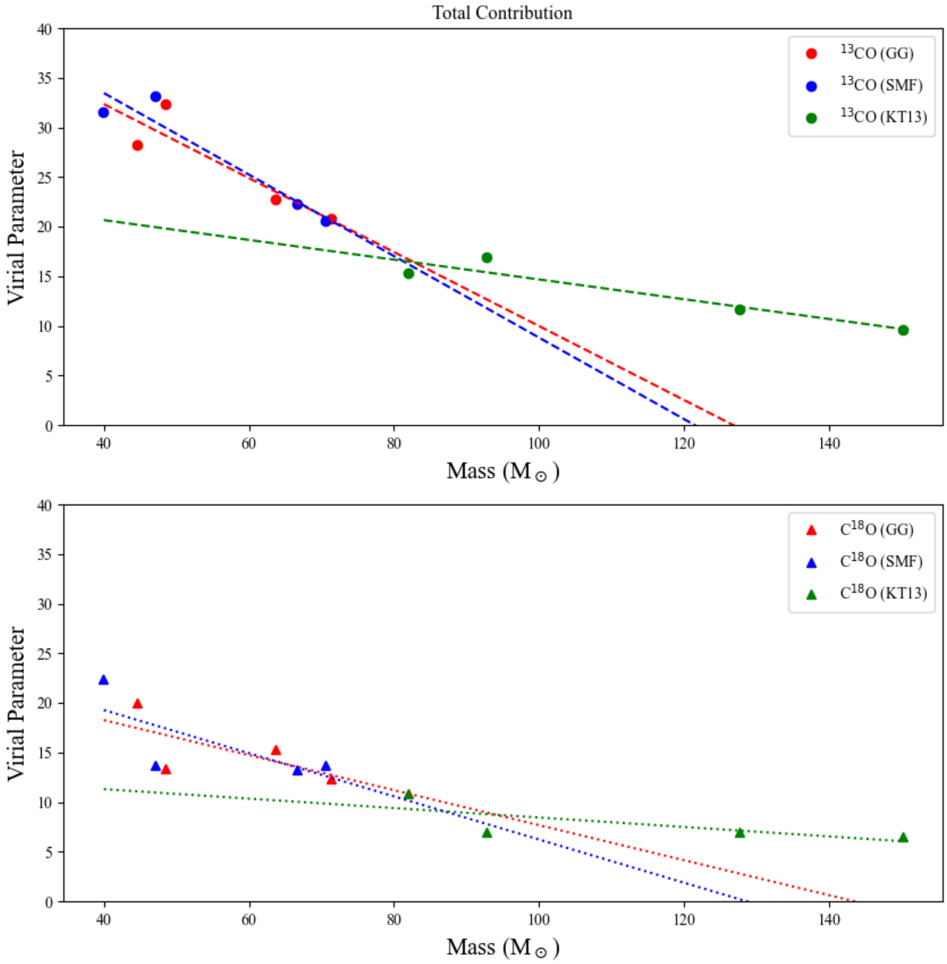

Figure 3.24: Illustrates how the virial parameter depends on the mass in the case where the total velocity dispersion contribution is considered. The different sets of values are present in the legend

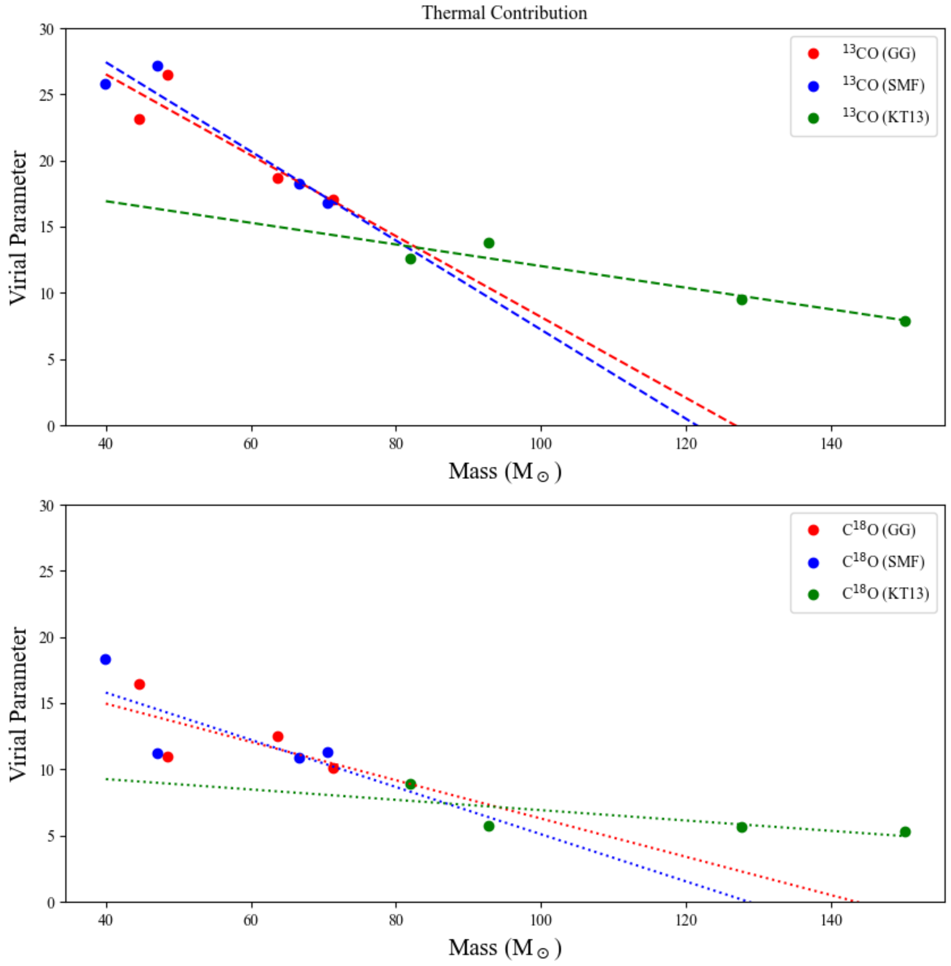

Figure 3.25: Illustrates how the virial parameter depends on the mass in the case where only the thermal velocity dispersion contribution is considered. The different sets of values are present in the legend

3.5 Additional abundances from IRAM-30m telescope

In addition to the CO isotopologues from the GBT data, we also studied additional abundances taken with the IRAM-30m telescope, such as $H^{13}CO^+$, $HC^{18}O^+$, $C^{18}O$, N_2H^+, HNCO, $HN^{13}C$, H_2CO, CH_3OH. The IRAM-30m telescope covered solely the northern part of the ring structure observed from the GBT maps. The integrated intensity maps for those different molecules are shown in Figure 3.27. The integrated intensity maps for the different molecules were regridded to the map with the worst resolution among them, which happened to be the map of $HC^{18}O^+$. All of the necessary spectroscopic information is reported in Table 3.5 needed to estimate the column density.

Table 3.5: Spectroscopic information such as the observed molecular transitions, rest frequencies, Einstein A coefficients, rotational constants, the energy of the lower state, degeneracy of the upper state, as well as the estimated partition function.

Species	$J_u - J_l$	ν (MHz)	$log_{10}A$ (s^{-1})	B_0 (MHz)	E_L (K)	g_u	Q_{rot}
$H^{13}CO^+$	(1-0)	86754.2884	-4.41416	43377.320	0.00	3	3.956
$HC^{18}O^+$	(1-0)	85162.2231	-4.43833	42581.210	0.00	3	4.023
$C^{18}O$	(1-0)	109782.1734	-7.20302	54891.420	0.00	3	3.205
N_2H^+	(1-0)	93173.3977	-4.44034	46586.867	0.00	3	33.258
HNCO	(4-3)	87925.2370	-5.05655	11071.010	6.33	9	36.90
$HN^{13}C$	(1-0)	87090.8500	-4.72878	43545.610	0.00	3	3.82
H_2CO	(2-1)	145602.9490	-4.10719	38833.987	3.49	5	10.52
CH_3OH	(3-2)	145103.1850	-4.90930	24679.980	6.96	7	13.25

For the case of N_2H^+ the partition function was determined in another way. When obtaining the column density for N_2H^+, the integrated intensity of the desired isolated component was considered only. In this case, the partition function Q_{hfs} was determined with the help of the values from the JPL catalog. The file consisted of seven measurements of how Q_{rot} varies depending on the temperature. A polynomial of the first order was later on fitted to the points, thus giving us a relation between the temperature and rotational partition function and making it possible to interpolate the value of the partition function at 7.5 K.

The corresponding spectra for the locations marked in the map are shown in Figure 3.29. The integration range for the IRAM was established to range from 39.4 km/s to 46.9 km/s. The main motive behind the selection was to ensure that the dense gas tracers were included inside the range. Since we only utilized one of the hyperfine lines for N_2H^+, the upper limit for the integration range was thus chosen in order to ensure that the other hyperfine lines were excluded. Consequently, some parts of the emission of $C^{18}O$ remain excluded, seeing as $C^{18}O$ shows a broader line compared to the rest of the molecules. Only the emission within the integration range was considered when creating the integrated intensity maps from now on.

The integrated intensity, column density, and abundances of each molecule are shown in Figure 3.30. The white pixels present in the abundance maps are masked pixels from the mass surface density maps. The dark blue pixels correspond to regions where the emission was below the integrated noise and was therefore excluded.

The CO f_D maps in Figure 3.32 all show elevated depletion values towards positions 1 and 2. The f_D values derived from the Σ_{GG} show additionally enhanced values for the depletion factor towards the southern part of the map. The depletion factor values derived from the Σ_{KT13} are significantly higher than the other maps.

Tables 3.6-3.7 contain collections of the different properties extracted for the four mentioned positions. In each case, the mass surface density and temperature values from the regridded maps with respect to the IRAM data are showcased, as well as properties mentioned in the section *Mass Surface Density and Dust Temperature Maps*. Moreover, the abundances of the original 8 molecules extracted from the IRAM data and their more common isotopologues were included. In the case of CO, the depletion factor was also shown in the tables.

Table 3.6: The estimated properties for positions 1 to 4 within IRDC G034.77-00.55 based on the GG mass surface density map.

Parameter	GG				Units
Position	1	2	3	4	
Σ	0.0945	0.0816	0.0678	0.0636	(gcm^{-2})
T	18.42	19.53	20.38	20.37	(K)
N_H	4.03	3.48	2.89	2.72	10^{22} (cm^{-2})
n_H	4.36	3.76	3.13	2.93	10^{4} (cm^{-3})
t_{ff}	2.08	2.24	2.46	2.54	10^{5}(yrs)
A_v	21.23	18.33	15.23	14.29	(mag)
$\bar{A}_v$	5.31	4.58	3.81	3.57	(mag)
[H^{13}CO^{+}]	2.59 ± 0.80	2.85 ± 1.11	2.01 ± 0.78	3.23 ± 1.00	10^{-11}
[HCO^{+}]	1.29 ± 0.47	1.42 ± 0.52	1.00 ± 0.37	1.61 ± 0.59	10^{-9}
[HC^{18}O^{+}]	0.22 ± 0.07	0.71 ± 0.22	0.02 ± 0.01	0.71 ± 0.22	10^{-11}
[C^{18}O]	1.10 ± 0.35	1.59 ± 0.50	2.00 ± 0.63	1.61 ± 0.51	10^{-7}
[CO]	3.59 ± 1.34	5.19 ± 1.94	6.53 ± 2.44	5.37 ± 2.01	10^{-5}
[N$_2$H^{+}]	3.35 ± 1.05	3.12 ± 0.98	1.07 ± 0.33	1.98 ± 0.62	10^{-10}
[HNCO]	6.35 ± 2.16	5.33 ± 1.81	2.99 ± 1.11	4.47 ± 1.52	10^{-10}
[HNC]	2.16 ± 0.79	2.07 ± 0.76	0.49 ± 0.18	1.20 ± 0.44	10^{-9}
[H$_2$CO]	1.15 ± 0.37	1.48 ± 0.48	1.89 ± 0.61	2.69 ± 0.87	10^{-10}
[CH$_3$OH]	2.02 ± 0.70	2.63 ± 0.92	1.45 ± 0.51	3.51 ± 1.22	10^{-9}
f_D CO	3.90 ± 1.46	2.70 ± 1.01	2.14 ± 0.80	2.61 ± 0.98	

Table 3.7: The estimated properties for positions 1 to 4 within IRDC G034.77-00.55 based on the SMF mass surface density map.

Parameter	SMF				Units
Position	1	2	3	4	
Σ	0.1025	0.0805	0.0636	0.0527	(gcm^{-2})
T	15.01	16.23	16.90	16.72	(K)
N_H	4.37	3.43	2.71	2.25	10^{22} (cm^{-2})
n_H	4.73	3.71	2.93	2.43	10^{4} (cm^{-3})
t_{ff}	2.00	2.26	2.54	2.79	10^{5}(yrs)
A_v	23.02	18.07	14.29	11.84	(mag)
$\bar{A}_v$	5.76	4.52	3.57	2.96	(mag)
[$H^{13}CO^{+}$]	2.40 ± 0.74	2.95 ± 0.91	2.15 ± 0.66	3.93 ± 1.22	10^{-11}
[HCO^{+}]	1.20 ± 0.44	1.47 ± 0.54	1.07 ± 0.39	1.96 ± 0.72	10^{-9}
[$HC^{18}O^{+}$]	0.21 ± 0.07	0.74 ± 0.23	0.02 ± 0.01	0.87 ± 0.27	10^{-11}
[$C^{18}O$]	1.02 ± 0.32	1.64 ± 0.52	2.13 ± 0.67	2.00 ± 0.63	10^{-7}
[CO]	3.33 ± 1.24	5.36 ± 2.00	6.96 ± 2.60	6.55 ± 2.45	10^{-5}
[N_2H^{+}]	3.19 ± 1.00	3.30 ± 1.03	1.13 ± 0.35	2.4 ± 0.75	10^{-10}
[HNCO]	5.86 ± 1.99	5.48 ± 1.86	3.18 ± 1.08	5.42 ± 1.84	10^{-10}
[HNC]	2.00 ± 0.74	2.11 ± 0.78	0.52 ± 0.19	1.40 ± 0.52	10^{-9}
[H_2CO]	1.06 ± 0.34	1.52 ± 0.49	2.02 ± 0.65	3.29 ± 1.06	10^{-10}
[CH_3OH]	1.86 ± 0.65	2.69 ± 0.94	1.55 ± 0.54	4.27 ± 1.49	10^{-9}
f_D CO	4.20 ± 1.57	2.61 ± 0.98	2.01 ± 0.75	2.14 ± 0.80	

3.6 Model Comparison

The abundance and the depletion factor values for positions 1-4 are used in this chapter for model comparison in order to constrain the cosmic rate ionization rate and the chemical age of the cloud for Cloud G.

The astrochemical models used in this project were first developed by Walsh et al. (2015) and were further developed in Entekhabi et al. (2021), with the intention to illustrate how certain molecular abundances varied with respect to time. The chemical models in Walsh et al. (2015) utilized the UMIST Database (McElroy et al., 2013), which included processes such as photoionization and photodissociation. Furthermore, the gas-grain interaction was also considered in Walsh et al. (2015), by including the depletion of molecules onto the surface of dust grains by means of thermal- and nonthermal desorption, specifically a Cosmic Ray-induced thermal desorption. Additionally, the grain-surface reactions based on the OSU network (Garrod et al., 2008) were also included in the chemical model in Walsh et al. (2015). For a more detailed explanation see Walsh et al. (2015).

In this project two astrochemical model grids were used, Grid 1 and Grid 2, the exact same model grids that were utilized in Entekhabi et al. (2021). The CO ice binding energy,i.e. the energy required for desorption of the CO off the ice mantle, was assumed to be 855 K for Grid 1 and 1100 K for Grid 2 in Entekhabi et al. (2021). The Cosmic Ray-induced thermal desorption was solely included for Grid 2, where the heat released during the impact of cosmic rays contributes to the desorption of species, that were previously deposited onto the surface of dust grains, to be released into the gas phase and thus increasing their abundance. However, the photoreactions induced by Cosmic Rays, such as photodissociation and ionization, were included for both model grids.

The initial abundances for CO, HCO^+, N_2H^+ are reported in Table 1 in Entekhabi et al. (2021). Each model in a grid is associated with a certain number density, temperature, visual extinction, and cosmic ray ionization rate (Entekhabi et al., 2021), resulting in 137750 models. The range for each of these parameters is mentioned in Table 2 in Entekhabi et al. (2021). Each unique model is based on the different combinations of values for the parameters and each model is evolved during a time-lapse of 10^8 years.

The number density, dust temperature, and visual extinction are determined for each of the four positions, implying that the cosmic ray ionization rate is the only parameter that is unknown. The parameters were fixed to A_v=4 mag, T=20 K for the GG case, and A_v=4 mag, T=15 K for the SMF case. For both cases, the number density for the different regions was rounded to the closets density values, which was $4.6 \cdot 10^4$ cm^{-3} for the first two positions and $2.2 \cdot 10^4$ cm^{-3} for the last two positions. But we can constrain the CRIR value with the estimated abundances of CO, HCO^+, N_2H^+, by comparing the observed abundances of [CO],[HCO^+],[N_2H^+] to the theoretical abundances predicted by the models. We are therefore searching for a CRIR that can explain the abundances for all of the species of interest, which is why it is necessary to observe multiple molecules in order to better constrain the CRIR. This is achieved by ensuring that χ^2 expressed as in equation 6 in Entekhabi et al. (2021) is minimized, by choosing ζ and t in a way to ensure that the difference between theoretical och measured abundance is as small as possible.

The χ^2 landscapes for the GG case are shown in Figures 3.33-3.36. The χ^2 landscape images for the different images are in general similar. The parameters ζ and t are in general more constrained in the χ^2 landscapes from Grid 2 than those from Grid 1. The lowest χ^2 values, represented with a white cross can be observed to be mostly constrained to lower ionization rates.

The ζ and t in addition to the χ^2 values for every white cross are reported in Table 3.8 and 3.9 for both the GG and SMF cases. The average value of ζ and t for the GG case were roughly $2.5 \cdot 10^{-18}$ s^{-1} and $4.6 \cdot 10^6$ years for Grid 1 and $5.35 \cdot 10^{-18}$ s^{-1} and $3 \cdot 10^5$ years for Grid 2. The value of the age of the cloud estimated through Grid 2 is similar to the local free-fall times in Tables 3.6-3.7. The average value of ζ and t for the SMF case on the other hand were roughly $6.7 \cdot 10^{-18}$ s^{-1} and $3.86 \cdot 10^5$ years for Grid 1 and $5.35 \cdot 10^{-18}$ s^{-1} and $7.66 \cdot 10^5$ years for Grid 2.

	GG			
Grid 1	Region 1	Region 2	Region 3	Region 4
ζ (s^{-1})	$2.2 \cdot 10^{-18}$	$4.6 \cdot 10^{-18}$	$1.0 \cdot 10^{-18}$	$2.2 \cdot 10^{-18}$
t (yrs)	$1.10 \cdot 10^{7}$	$1.95 \cdot 10^{6}$	$3.55 \cdot 10^{6}$	$2.34 \cdot 10^{6}$
χ^2	0.936	1.547	0.849	0.124
	SMF			
ζ (s^{-1})	$1.0 \cdot 10^{-17}$	$1.0 \cdot 10^{-17}$	$2.2 \cdot 10^{-18}$	$4.6 \cdot 10^{-18}$
t (yrs)	$2.57 \cdot 10^{5}$	$2.34 \cdot 10^{5}$	$6.46 \cdot 10^{5}$	$4.07 \cdot 10^{5}$
χ^2	0.856	1.324	0.583	0.636

Table 3.8: Collection of the parameter determined for each region based on the extreme-restricted χ^2 landscape for Grid 1.

	GG			
Grid 2	Region 1	Region 2	Region 3	Region 4
ζ (s^{-1})	$4.6 \cdot 10^{-18}$	$1 \cdot 10^{-17}$	$2.2 \cdot 10^{-18}$	$4.6 \cdot 10^{-18}$
t (yrs)	$2.75 \cdot 10^{5}$	$2.14 \cdot 10^{5}$	$3.55 \cdot 10^{5}$	$3.55 \cdot 10^{5}$
χ^2	0.449	1.000	0.576	0.458
	SMF			
ζ (s^{-1})	$4.6 \cdot 10^{-18}$	$1.0 \cdot 10^{-17}$	$2.2 \cdot 10^{-18}$	$4.6 \cdot 10^{-18}$
t (yrs)	$6.02 \cdot 10^{5}$	$5.37 \cdot 10^{5}$	$1.15 \cdot 10^{6}$	$7.76 \cdot 10^{5}$
χ^2	0.348	0.836	0.537	0.214

Table 3.9: Collection of the parameter determined for each region based on the extreme-restricted χ^2 landscape for Grid 2.

The evolution of the $\mathrm{CO}, \mathrm{HCO}^+$, and $\mathrm{N_2H^+}$ are visualized in Figure 3.37 to Figure 3.40, where the number density, visual extinction, and temperature are kept fixed as previously. Five different values were considered for the CRIR ranging from $\zeta = 10^{-19}$ s^{-1} to $\zeta = 10^{-15}$ s^{-1}. The only true free parameter was the age of the cloud. The dotted line showed the predicted abundances from Grid 1 and the solid lines show the predicted abundances for Grid 2.

Studying the evolution of [CO], we can see that for the case of Grid 1 the best CRIR value would in general correspond to $\sim 10^{-18}$ s^{-1} for a smaller timescale of $10^6 - 10^7$ years. But for greater timescales around 10^8, the CRIR could potentially increase to 10^{-16} s^{-1} (especially for regions 2 and 3 see Figures 3.38 and 3.39. For Grid 2 on the other hand, for timescales ranging from 10^5 to 10^6 years, the CRIR value for the best model would be $\sim 10^{-17}$ s^{-1} and for timescales greater than 10^7 years the value would be closer to $\sim 10^{-16}$ s^{-1}.

The highest possible CRIR value obtained by $[\mathrm{N_2H^+}]$ would be $\sim 10^{-15}$ s^{-1} for Grid 1 and Grid 2, but this value is obtained by the model for a timescale less than 10^4 years. In general, for $[\mathrm{N_2H^+}]$ the later timescale solutions have a lower ionization rate, this is true for both Grid 1 and Grid 2. For the time similar to that of the t_{ff} the ionization rate would roughly correspond to $\sim 10^{-17}$ s^{-1}.

It is mainly the $[\mathrm{HCO^+}]$ that constrains the CRIR to lower values. The best ionization rate estimate for Grid 1 would correspond to a value of $\sim 10^{-18}$ s^{-1}, for Grid 2 the value would slightly increase to $\sim 10^{-18} - 10^{-17}$ s^{-1}.

The evolution of the $\mathrm{CO}, \mathrm{HCO}^+$, and N_2H^+ was likewise studied for the SMF case, the time evolution of regions 2 and 4 are visualized in 3.41 and 3.42. We can observe that [CO] struggles to constrain the value of the CRIR, seeing as all of the CRIR studied appear to be compatible with the observed abundance. The same reasoning can be applied for [N_2H^+], where the different models agree with the observed abundance for different timescales. It is therefore [HCO^+] that constrains the CRIR parameter. The greatest difference to the corresponding time evolution of region 2 for the GG case, is that the [HCO^+] constrain the CRIR to 10^{-17} s^{-1} rather than $\sim$ 10^{-18} s^{-1}. The observed abundance [HCO^+] for region 2 were $1.42{\cdot}10^{-9}$ (GG) and $1.47{\cdot}10^{-9}$ (SMF).The difference in the temperatures used for modeling is, therefore, the only explanation for the different outcomes of CRIR value. For grid 2, the optimal CRIR was found to range between $10^{-18} - 10^{-17}$ s^{-1}.

Figure 3.43 shows how f_D evolves with respect to n_H with the rest of the values fixed. The parameters were fixed at; A_v=4 mag, T=20 K for the GG case. In general, one expects the depletion factor to show a positive correlation towards the density, which we observed in the scatter plots for the GBT data. For [HCO$^+$]/[CO] and [N$_2$H$^+$]/[CO], one would need to observe more regions in order to determine a correlation between the abundance ratios and the number density. For the bottom panels in Figure 3.43, the observations agree more with the models with the greater CRIR parameter with the exception of [HCO$^+$]. The opposite can be said for the upper panels. The observed values as a collection/set are scattered alongside the red dotted line where CRIR is equal to $\zeta = 2.2 \cdot 10^{-18}$ s^{-1} and the chemical age of the cloud is estimated to be $2 \cdot 10^6$ years.

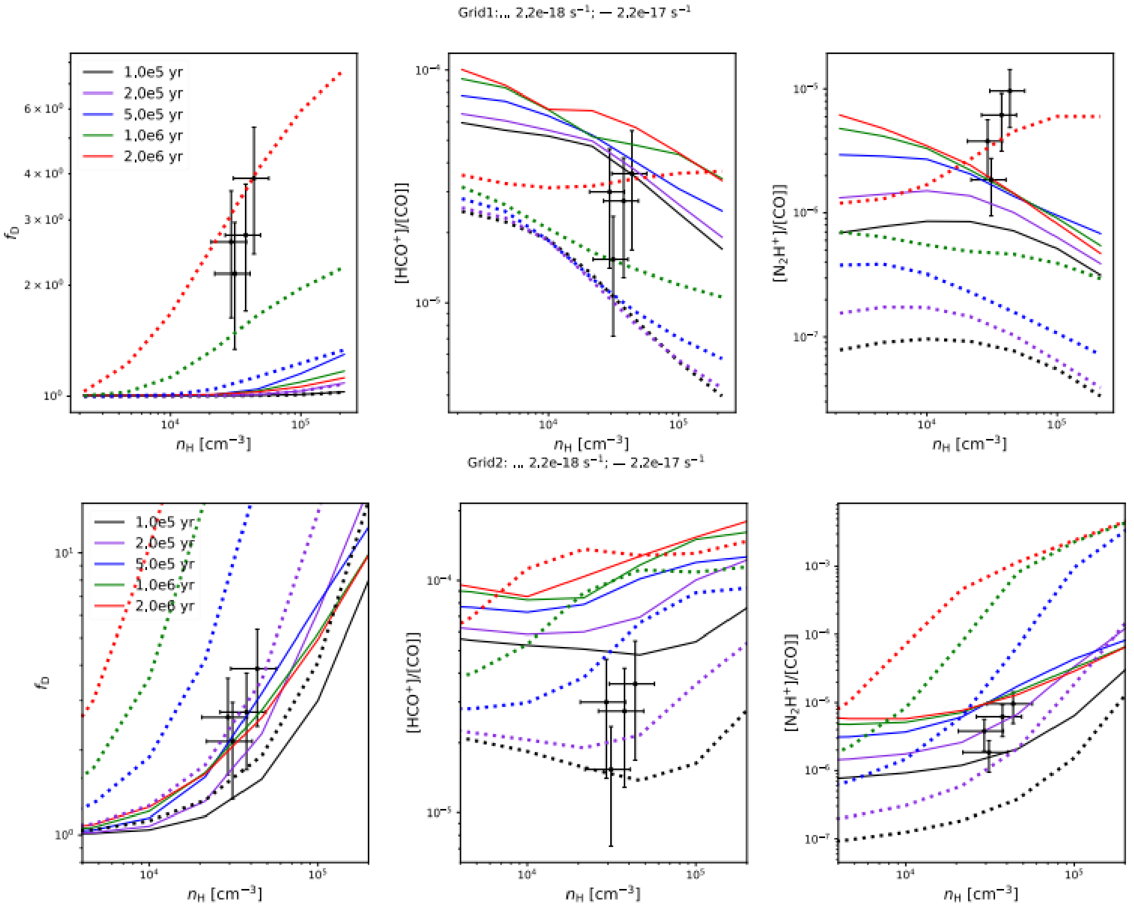

Figure 3.43: Showcasing the depletion, and the ratio between the abundances of CO, HCO$^+$, and N$_2$H$^+$ versus n_{H}, for a selective set of different timescales. Grid 1 was used to model the upper panels and Grid 2 for the bottom panels. The solid lines correspond to $\zeta = 2.2 \cdot 10^{-17}$ s^{-1} while the dotted ones correspond to $\zeta = 2.2 \cdot 10^{-18}$ s^{-1}. T = 15 K and A_v = 20 mag. The data for the observed regions are marked out with their respective uncertainties.

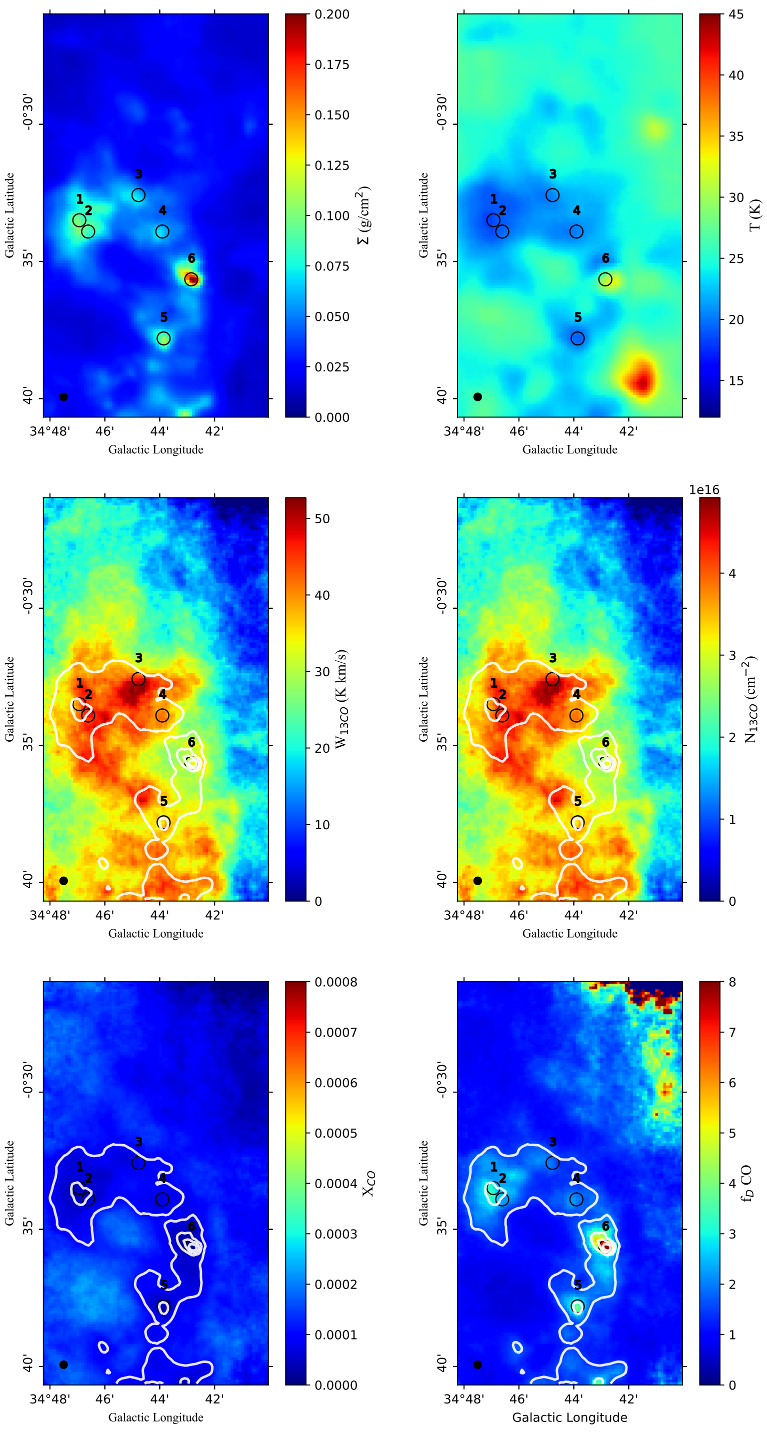

Figure 3.10: Top left: the mass surface density obtained with the GG method. Top right: the dust temperature map for the GG method. Middle left: the integrated intensity of ^{13}CO over the integration range 36-52.5 km/s. Middle right: the corresponding column density of ^{13}CO. Bottom left: the corresponding abundance of ^{13}CO. Bottom right: the depletion factor of CO. The mass surface density is overlayed on top of the middle and bottom rows as white contours. The maps had a pixel size of 6″.

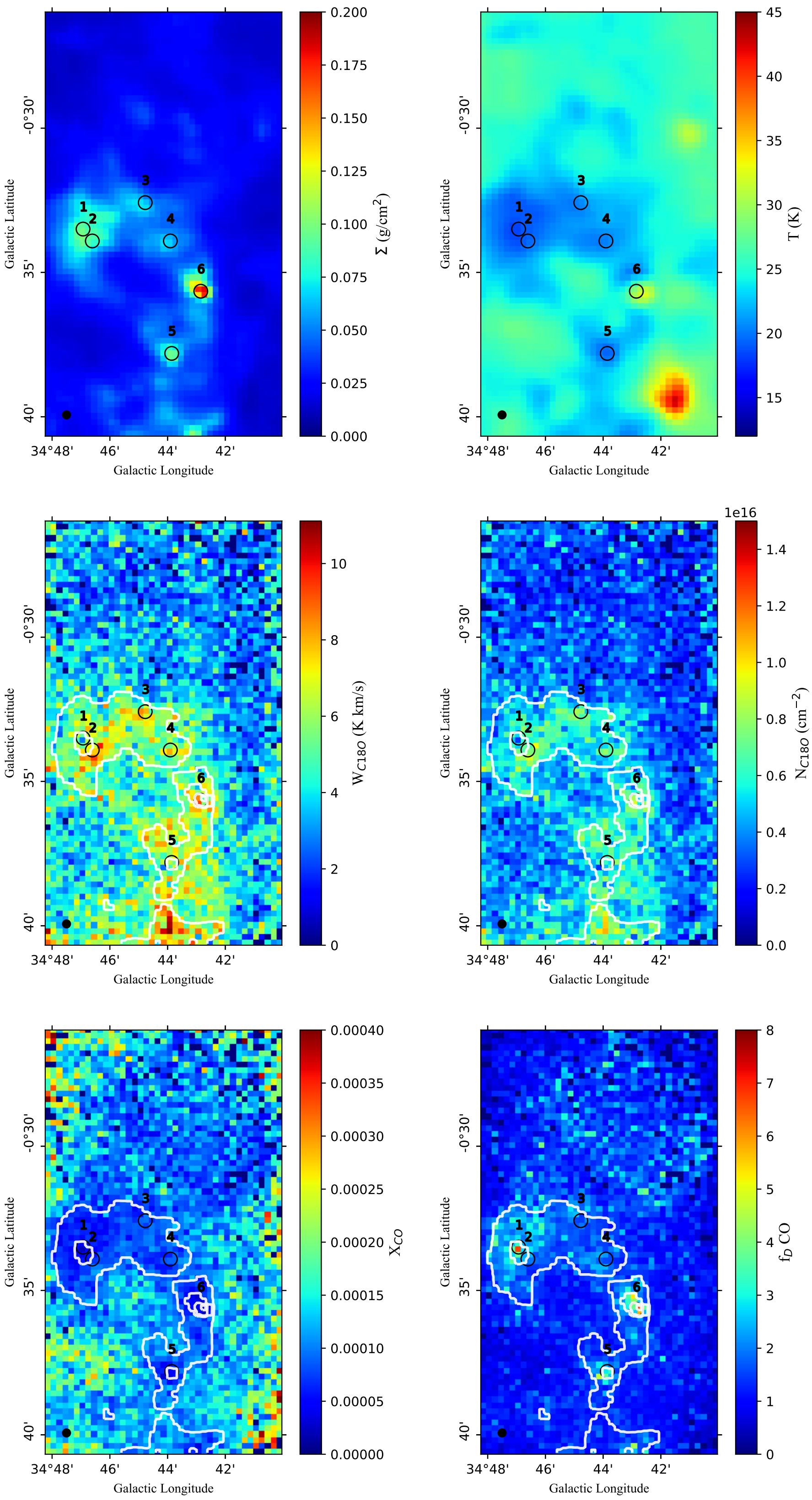

Figure 3.11: Same as in Figure 3.10 but for the instance of Σ_{GG} and integrated intensity for C^{18}O. The maps had a pixel size of 12″.

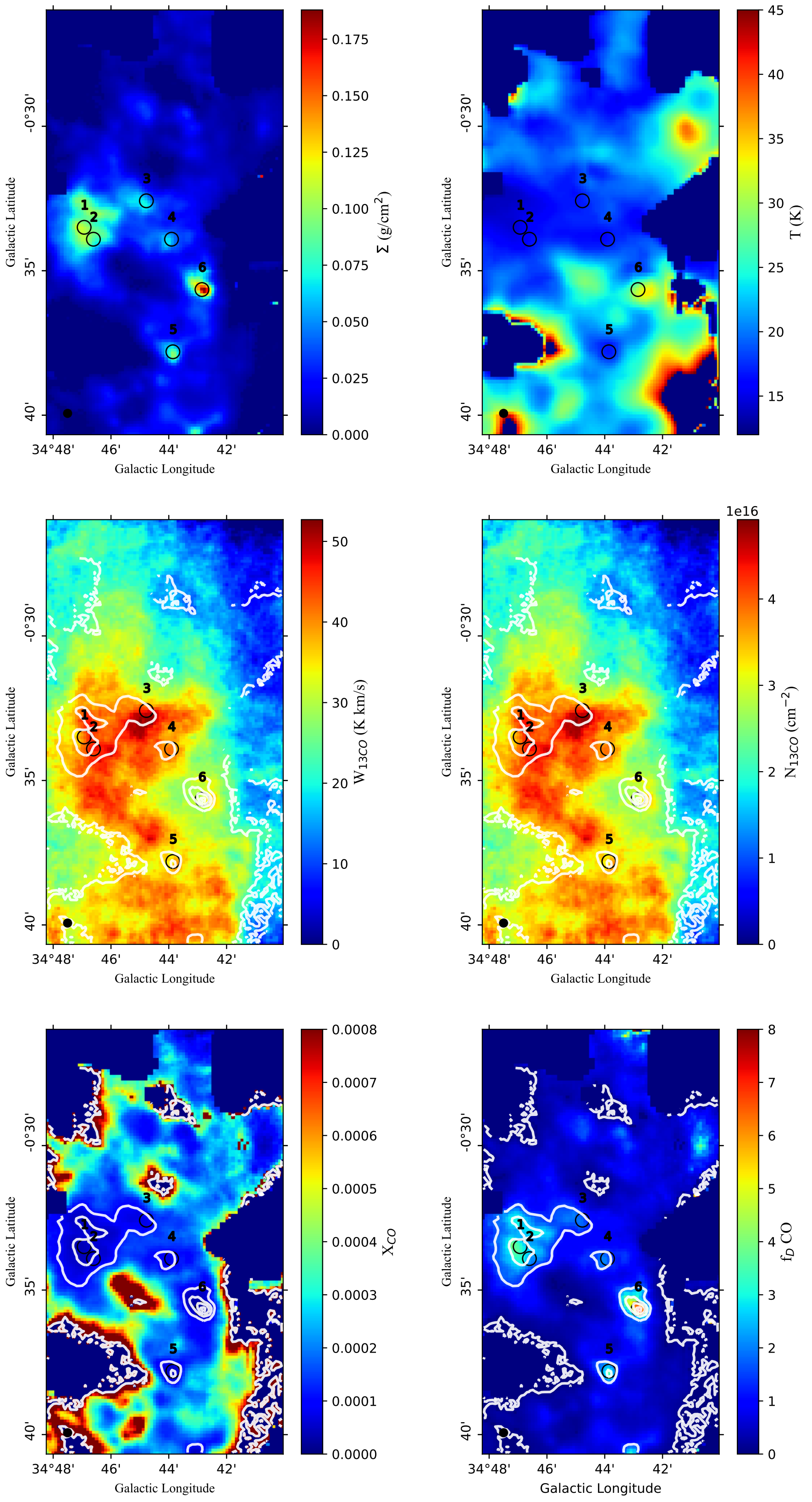

Figure 3.12: Same as in Figure 3.10 but for the instance of Σ_{SMF} and integrated intensity for ^{13}CO. The maps had a pixel size of $6''$.

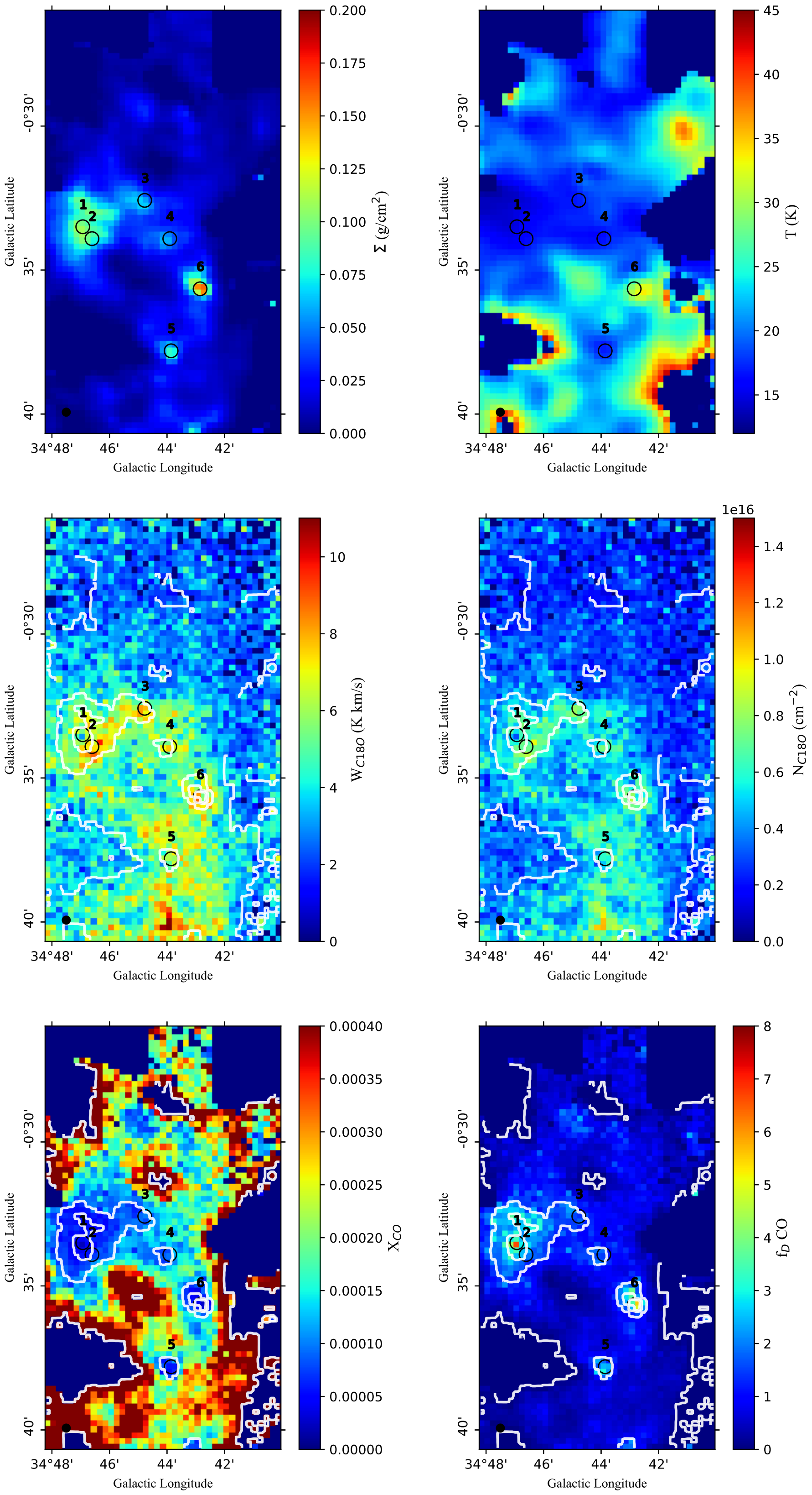

Figure 3.13: Same as in Figure 3.10 but for the instance of Σ_{SMF} and integrated intensity for C^{18}O. The maps had a pixel size of 12″.

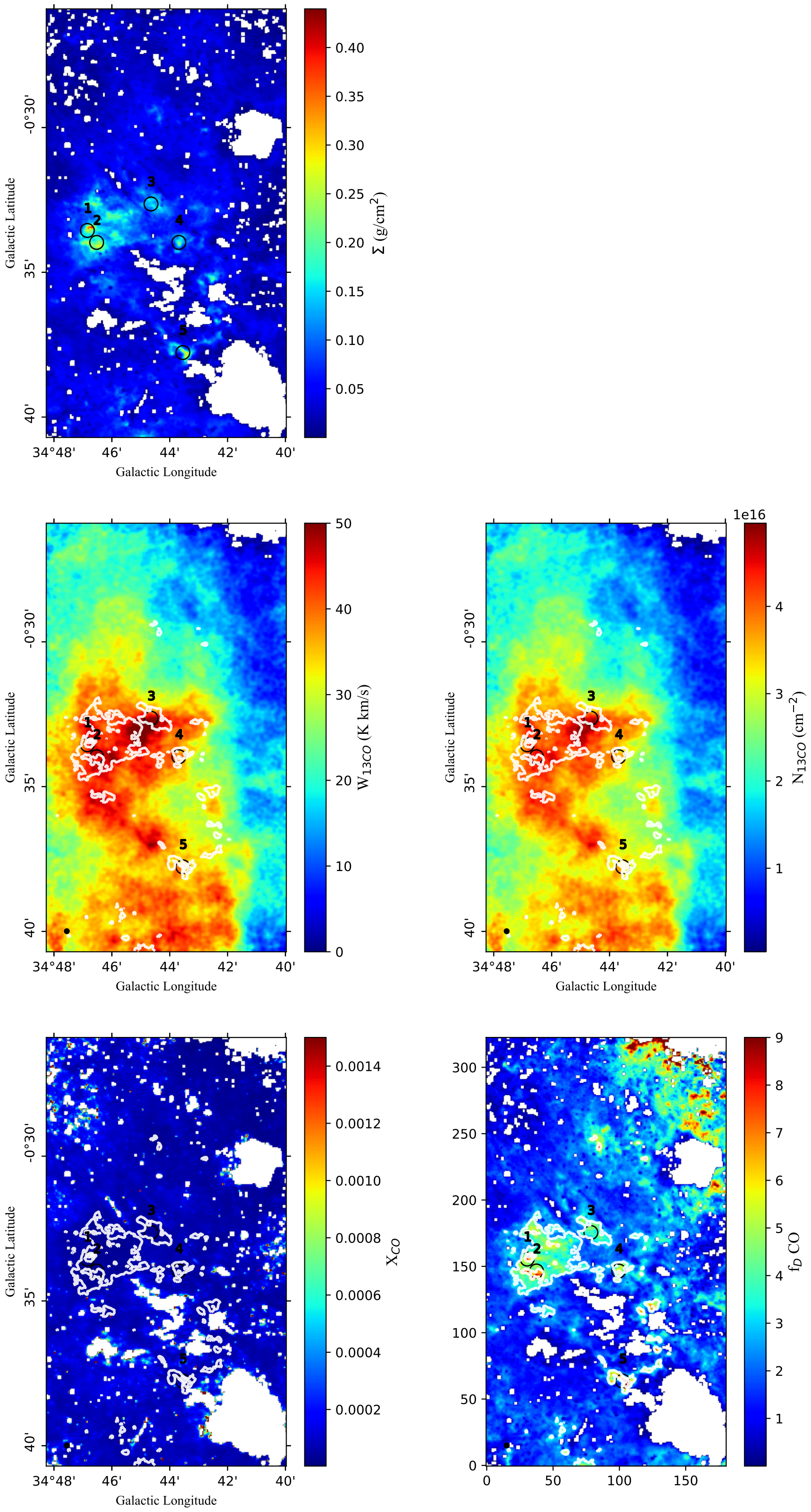

Figure 3.14: Same as in Figure 3.10 but for the instance of Σ_{KT13} and integrated intensity for ^{13}CO. The maps had a pixel size of 2.75″.

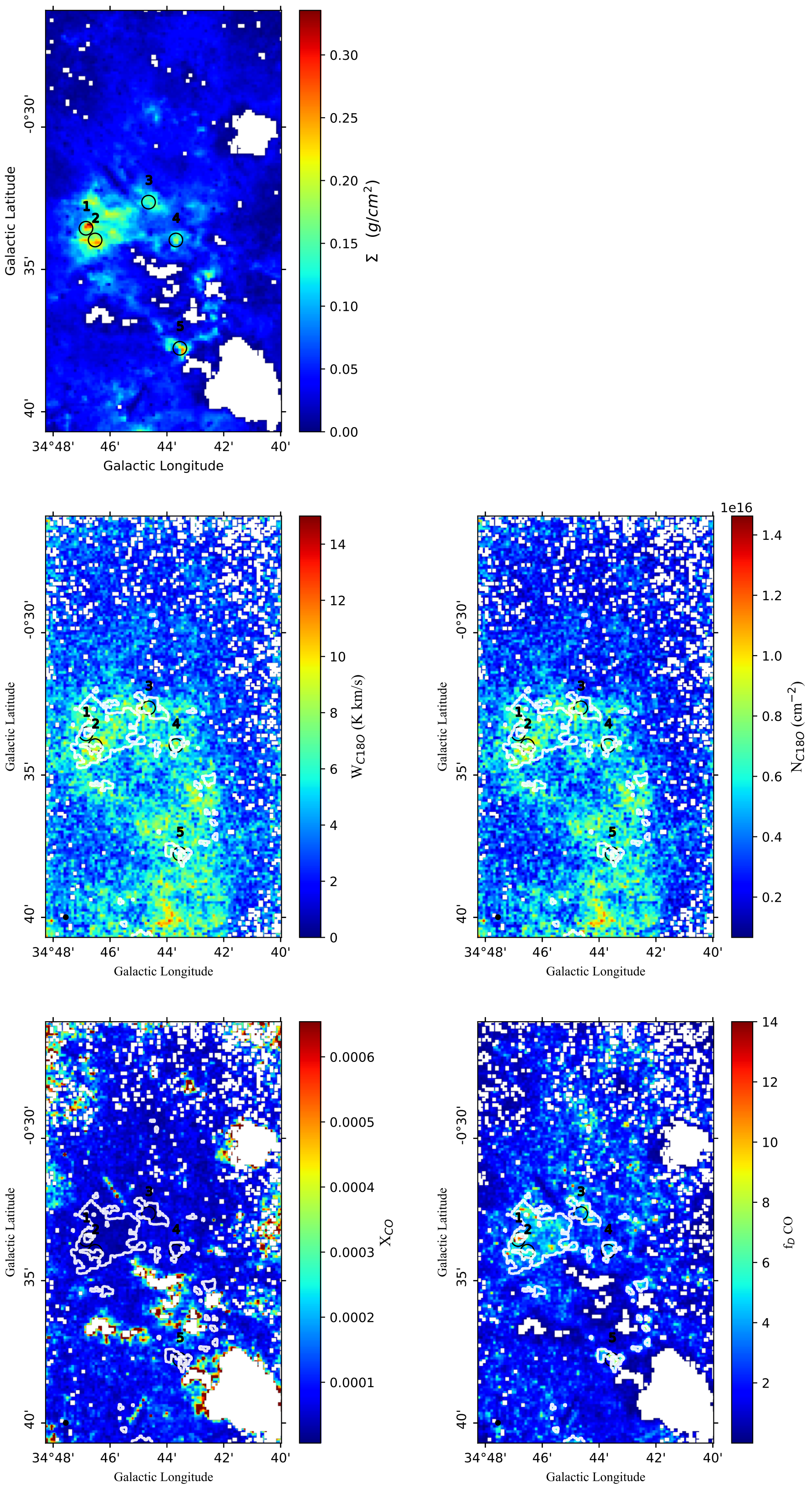

Figure 3.15: Same as in Figure 3.10 but for the instance of Σ_{KT13} and integrated intensity for C^{18}O. The maps had a pixel size of 5.5″.

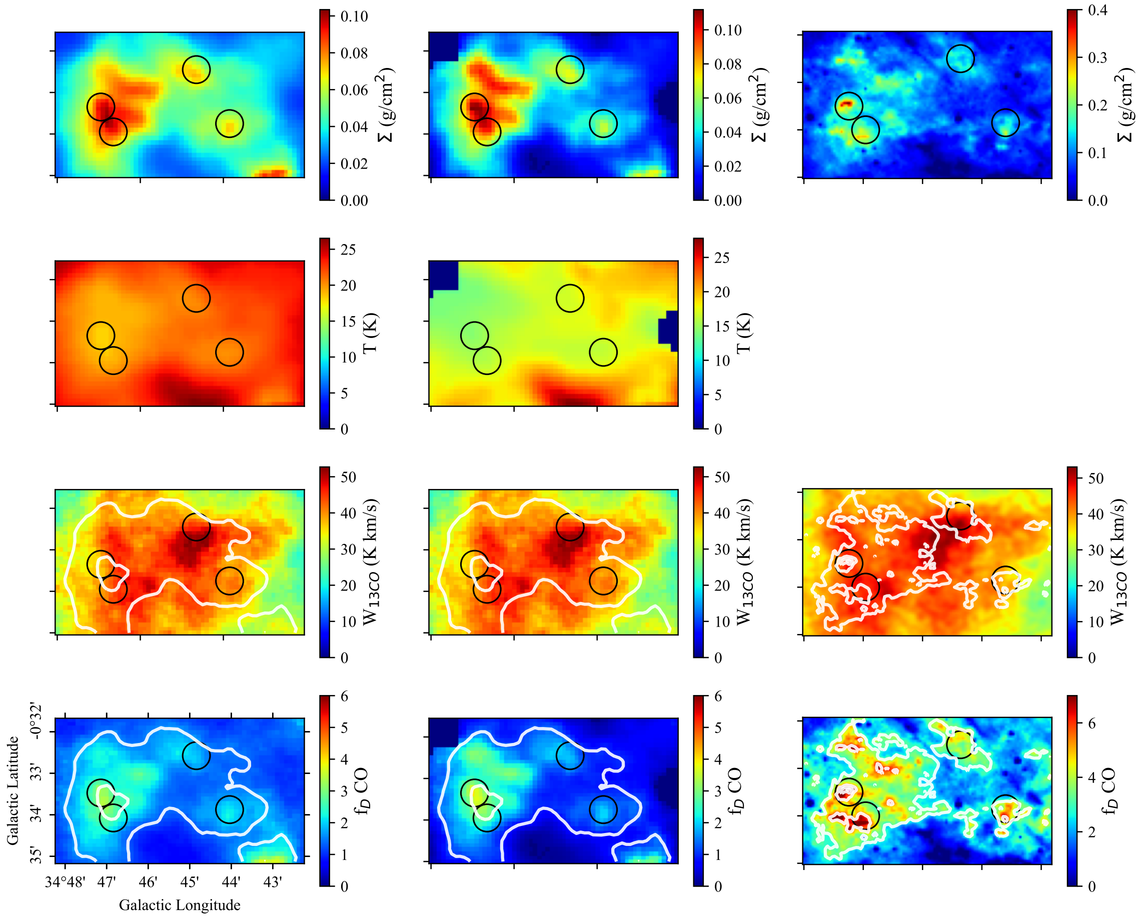

Figure 3.16: A collection of all the mass surface density maps, temperature maps, column density maps, and depletion factor maps zoom in towards the region enclosed in the ellipse defined in Simon et al. (2006a), Kainulainen & Tan (2013). The first, second, and third columns display the maps obtained with the GG-method, SMF-method, and KT13 respectively. The first and second rows show the mass surface density maps and the dust temperature map. The third and fourth rows show the column densities of ^{13}CO and the CO depletion factor map. Respective Σ was overlaid on top of the depletion maps.

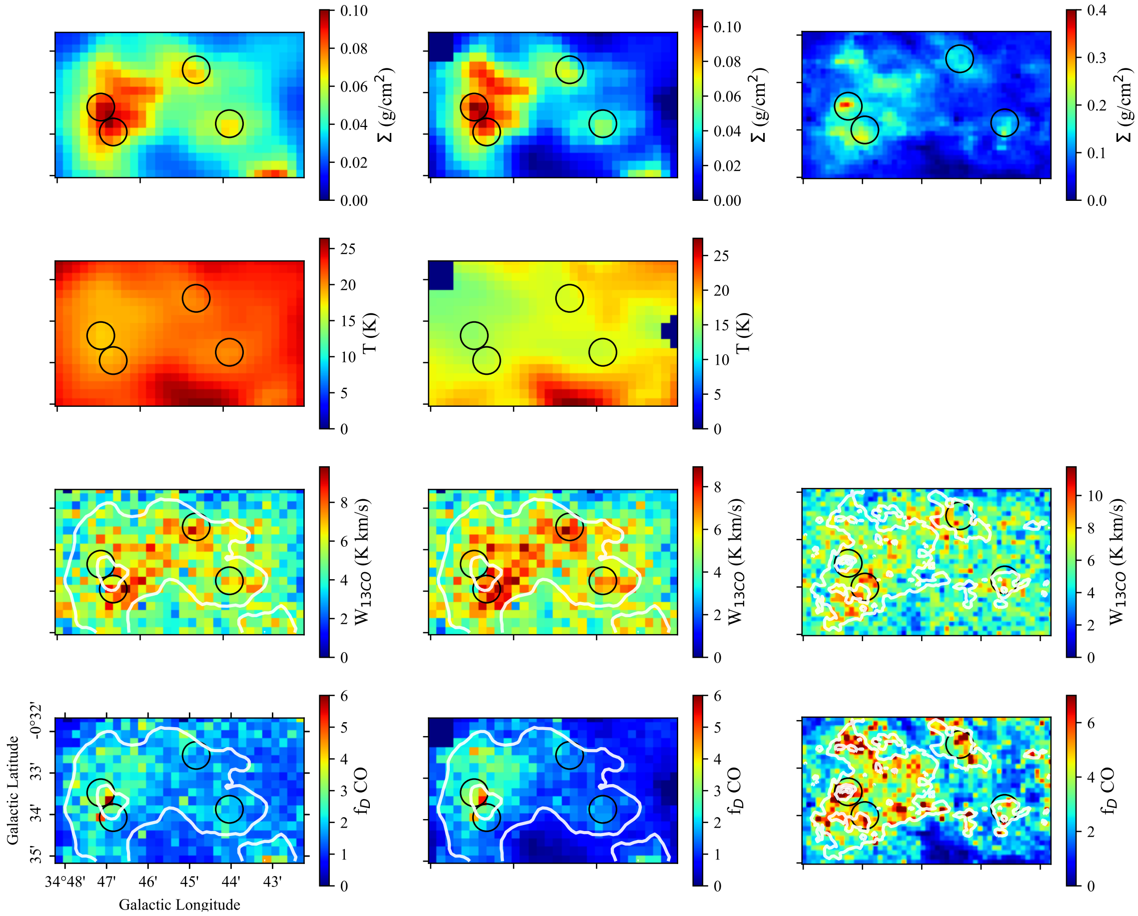

Figure 3.17: A collection of all the mass surface density maps, temperature maps, column density maps, and depletion factor maps zoom in towards the region enclosed in the ellipse defined in Simon et al. (2006a), Kainulainen & Tan (2013). The first, second, and third columns display the maps obtained with the GG-method, SMF-method, and KT13 respectively. The first and second rows show the mass surface density maps and the dust temperature map. The third and fourth rows show the column densities of C^{18}O and the CO depletion factor map. Respective Σ was overlaid on top of the depletion maps.

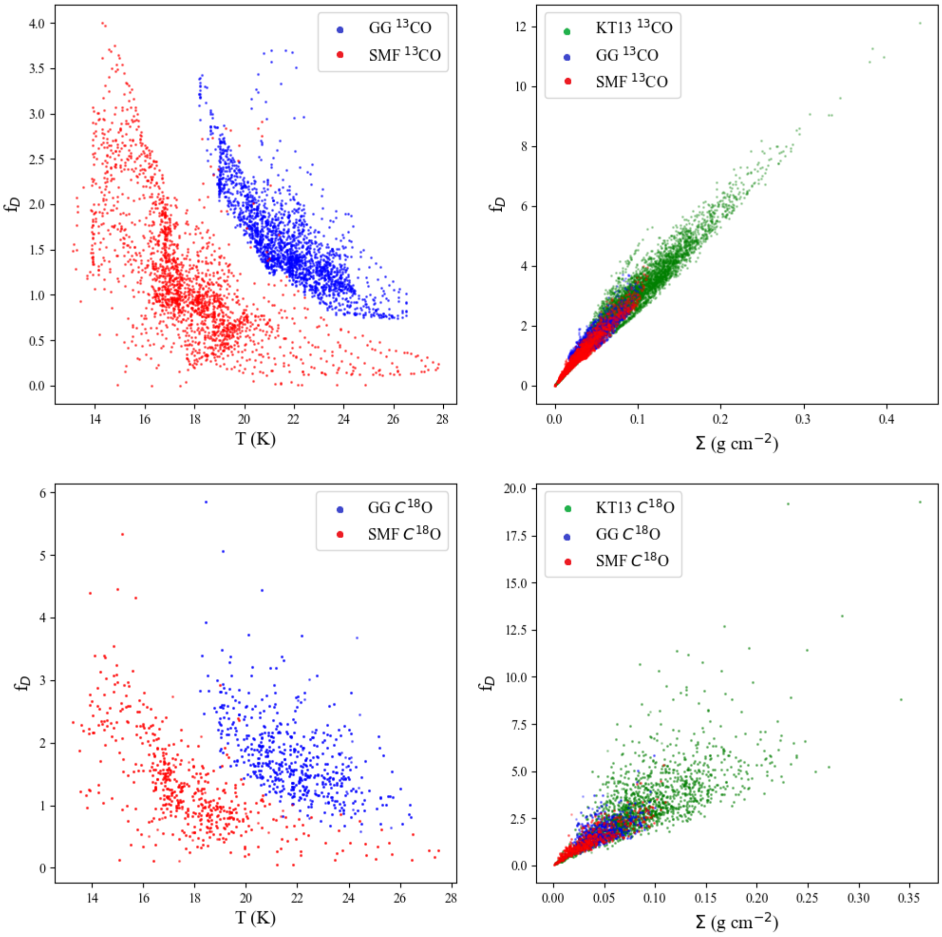

Figure 3.18: Scatter plot of the depletion factor against either the dust temperature (Left panel) or the mass surface density (Right panel). The depletion factors derived from the different instances are depicted in different colors.

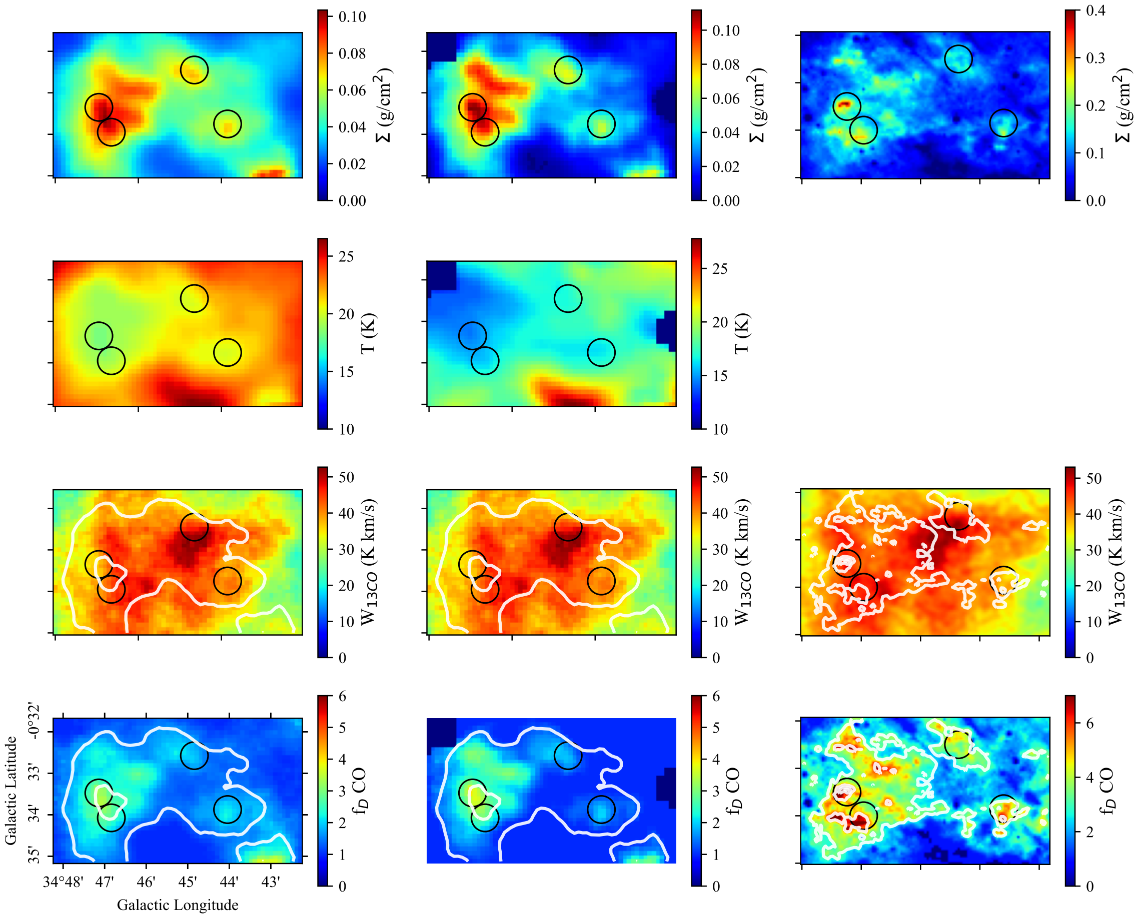

Figure 3.21: A collection of all the mass surface density maps, temperature maps, column density maps, and depletion factor maps zoom in towards the region enclosed in the ellipse defined in Simon et al. (2006a) and Kainulainen & Tan (2013). The first, second, and third columns display the maps obtained with the GG-method, SMF-method, and KT13 respectively. The first and second rows show the mass surface density maps and the dust temperature map. The third and fourth rows show the column densities of ^{13}CO and the CO depletion factor map. Respective Σ was overlaid on top of the depletion maps. Depletion factor values have been normalized, all depletion values below 1 now are set to equal to 1.

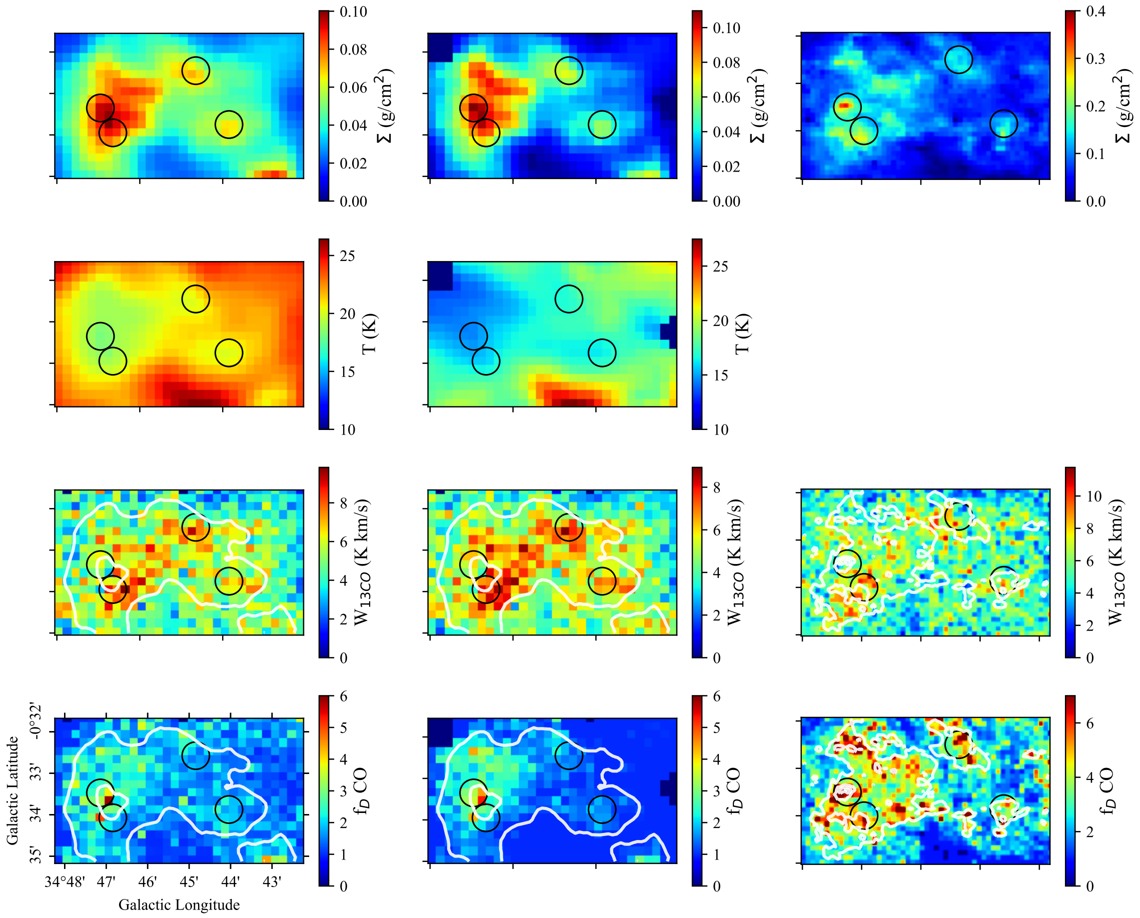

Figure 3.22: A collection of all the mass surface density maps, temperature maps, column density maps, and depletion factor maps zoom in towards the region enclosed in the ellipse defined in Simon et al. (2006a) and Kainulainen & Tan (2013). The first, second, and third columns display the maps obtained with the GG-method, SMF-method, and KT13 respectively. The first and second rows show the mass surface density maps and the dust temperature map. The third and fourth rows show the column densities of $C^{18}O$ and the CO depletion factor map. Respective Σ was overlaid on top of the depletion maps. Depletion factor values have been normalized, all depletion values below 1 now are set to equal to 1.

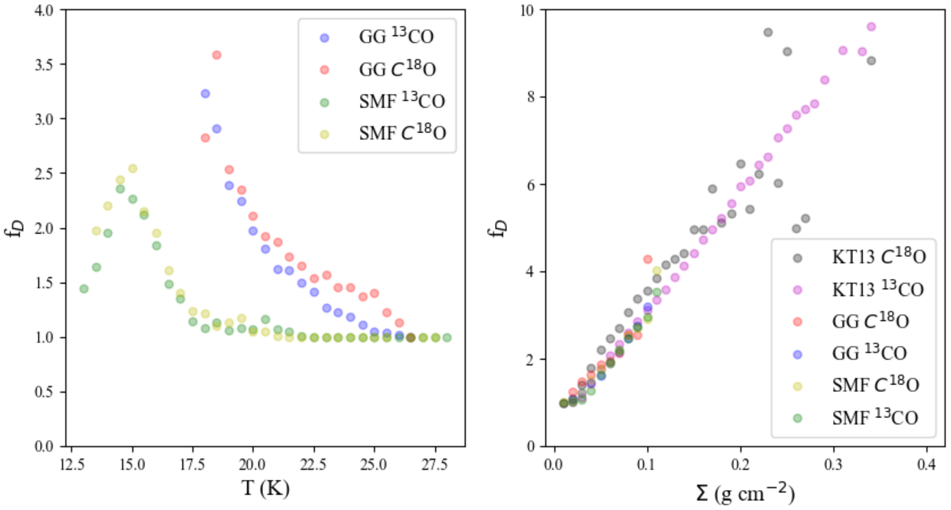

Figure 3.23: Same as in Figure 3.20 except that depletion factor values have been normalized. All depletion values below 1 in Figure 3.21 and 3.22 now are set to equal to 1 by multiplying with a scalar.

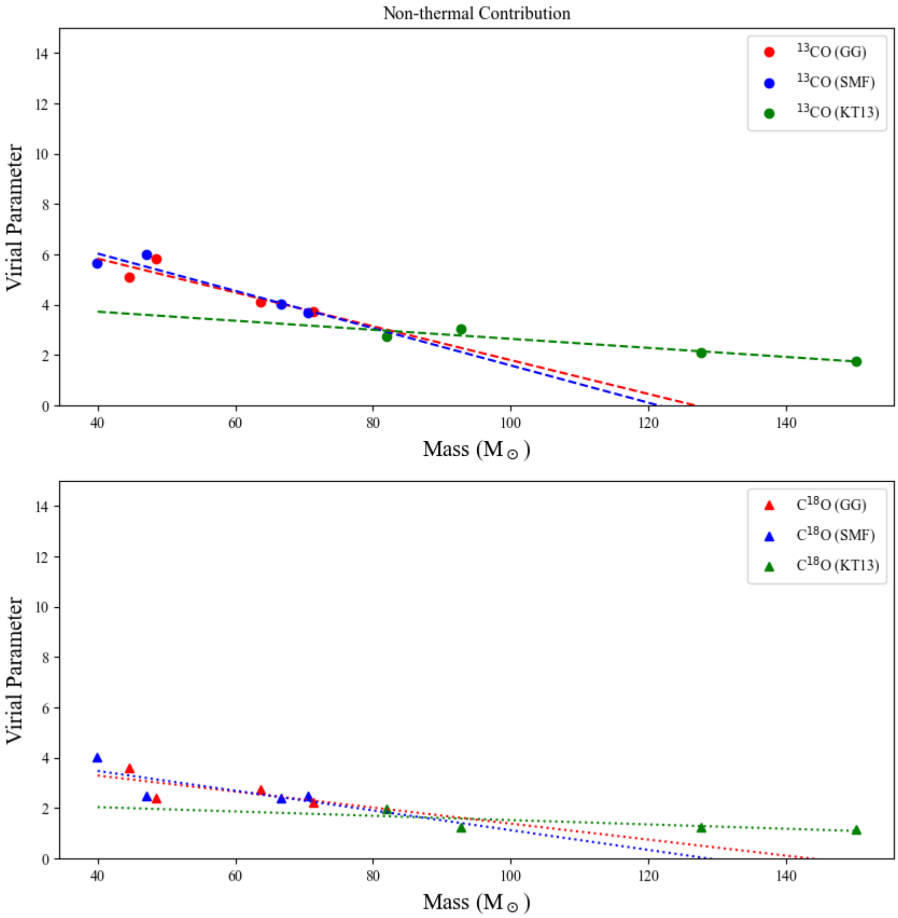

Figure 3.26: Illustrates how the virial parameter depends on the mass in the case where only the non-thermal velocity dispersion contribution is considered. The different sets of values are present in the legend

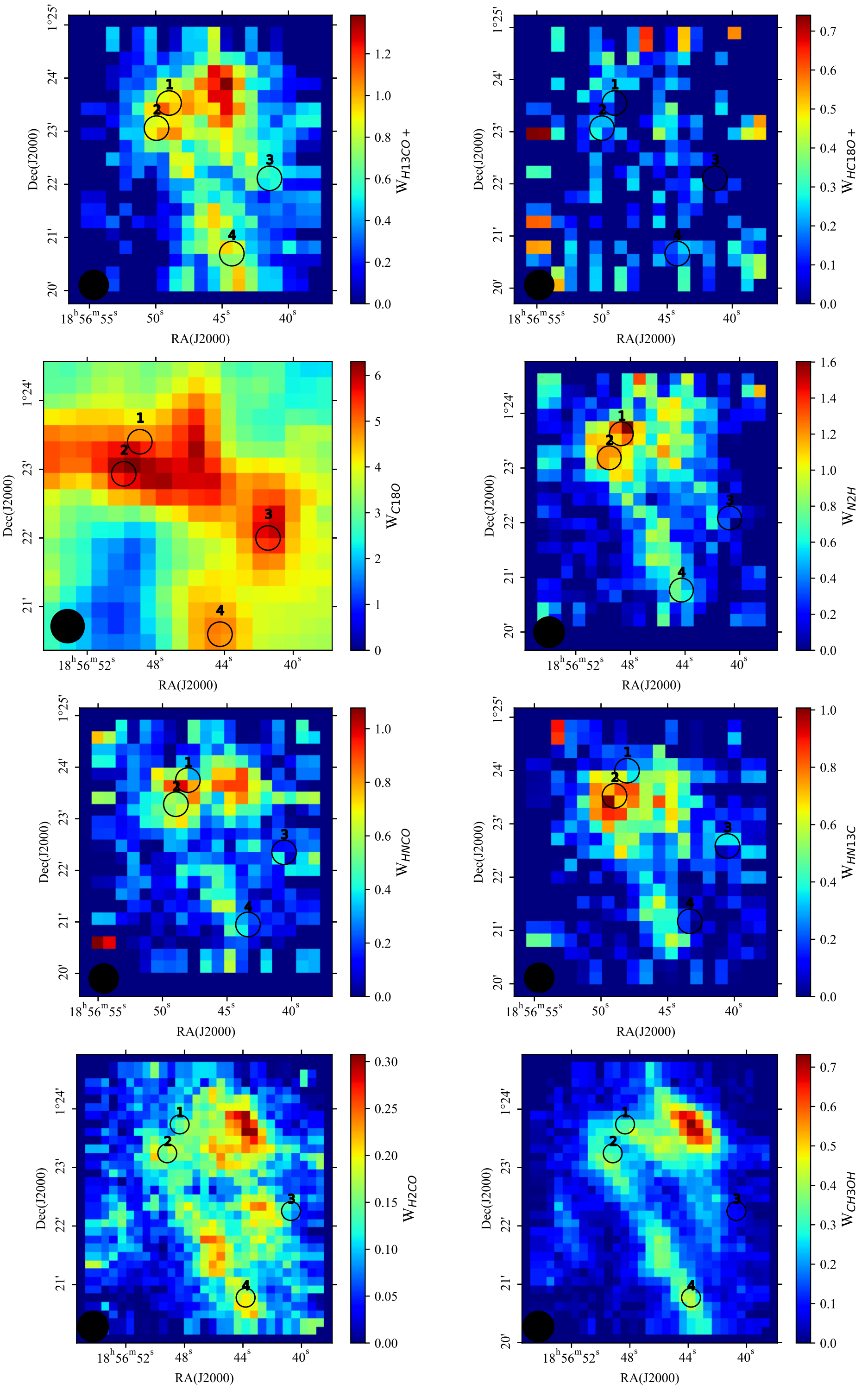

Figure 3.27: The integrated intensity maps for $H^{13}CO^+$(1-0), $HC^{18}O^+$(1-0), $C^{18}O$(1-0), N_2H^+(1-0), HNCO(4-3), $HN^{13}C$(1-0), H_2CO(2-1), and CH_3OH(3-2). In each panel, the distinct observed positions are marked with black circles.

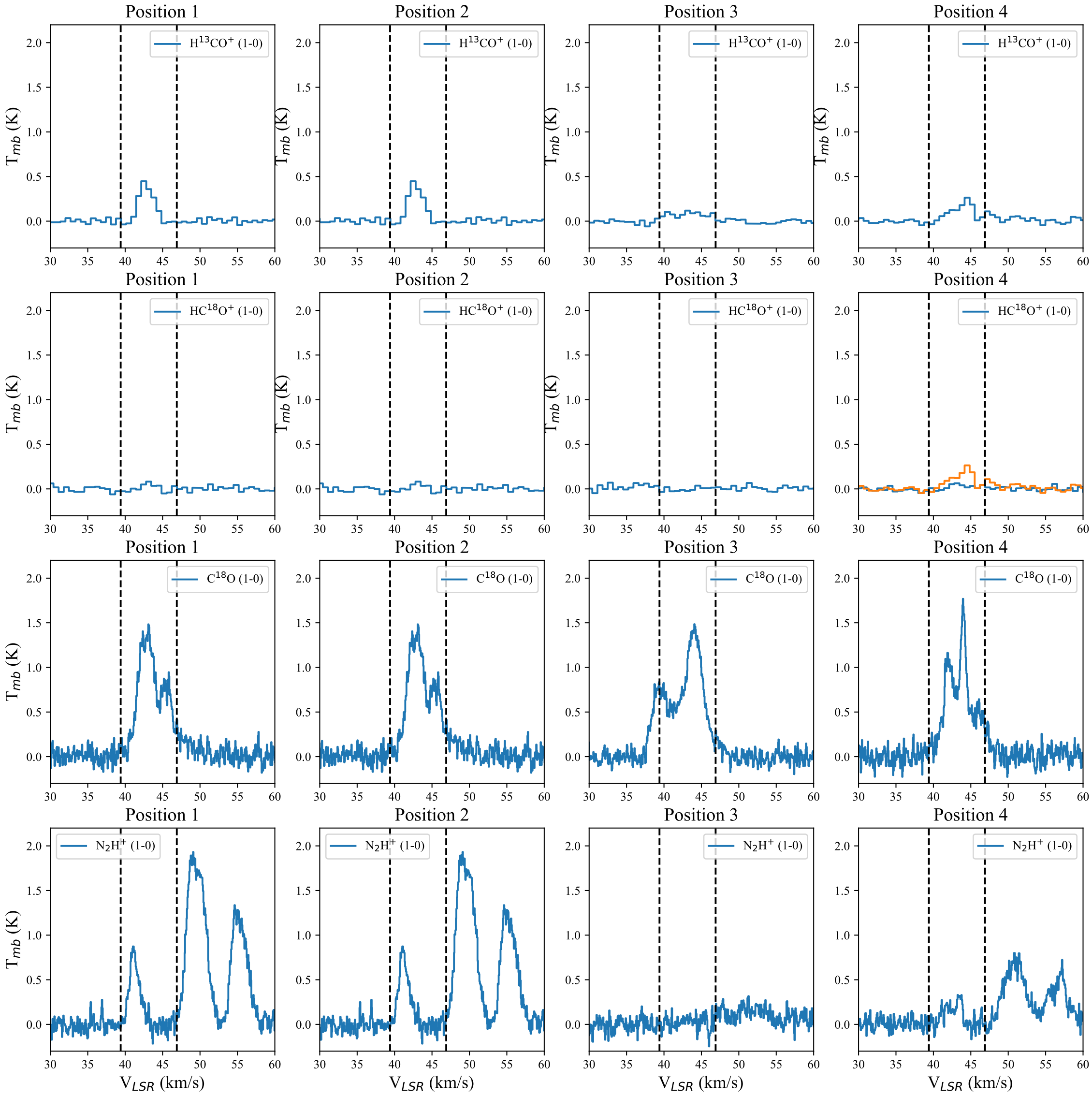

Figure 3.28: The corresponding spectra to the distinct observed regions from the IRAM data. The chosen integration range is shown with black dashed lines in each subplot in the figure

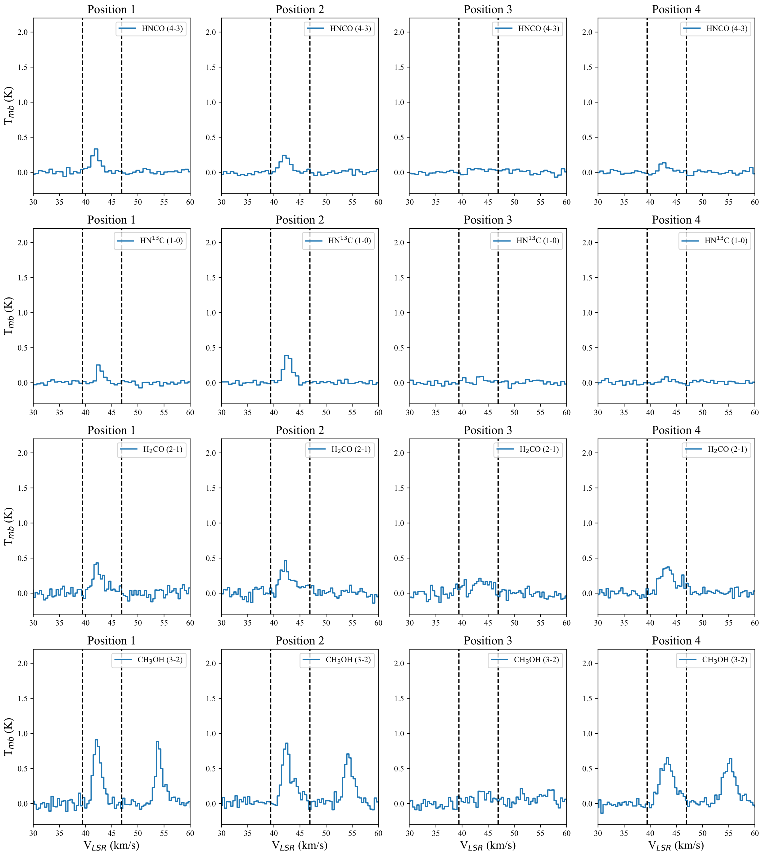

Figure 3.29: The corresponding spectra to the distinct observed regions from the IRAM data. The chosen integration range is shown with black dashed lines in each subplot in the figure

Figure 3.30: Collection of the IRAM maps. Each column corresponds to a certain molecule. The observed molecules are arranged from left to right as $H^{13}CO^+$(1-0), $HC^{18}O^+$(1-0), N_2H^+ (1-0) and $C^{18}O$(1-0). First row: the integrated intensity for each molecule. Second row: the respective column density. Third row: the molecular abundance using the Σ_{GG}. The fourth and fifth rows: same as in the third row but using Σ_{SMF} and Σ_{KT13}.

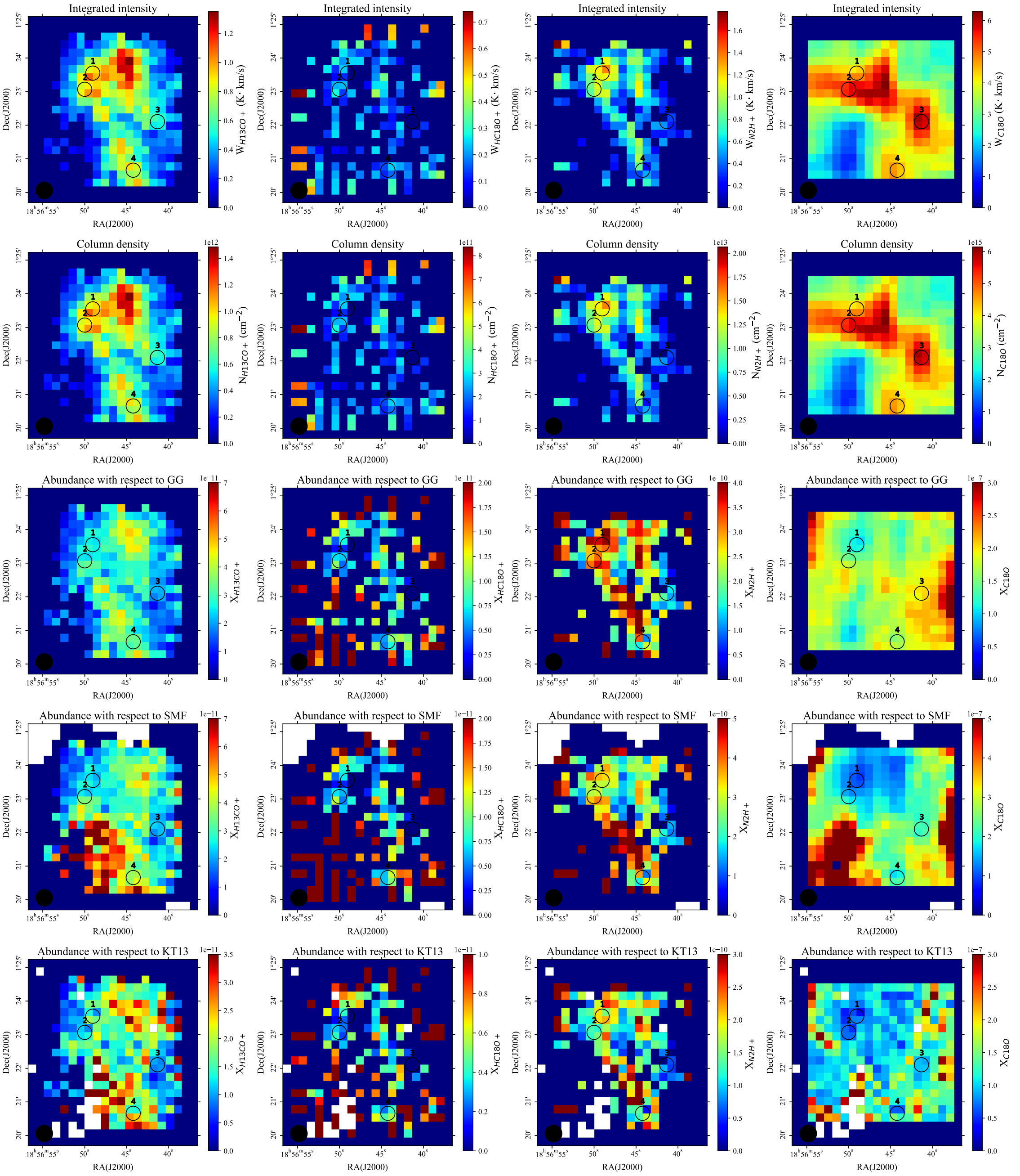

Figure 3.31: Collection of the IRAM maps. Each column corresponds to a certain molecule. The observed molecules are arranged from left to right as HNCO(4-3), $HN^{13}C$(1-0), H_2CO(2-1), and CH_3OH(3-2) and $C^{18}O$(1-0). First row: the integrated intensity for each molecule. Second row: the respective column density. Third row: the molecular abundance using the Σ_{GG}. The fourth and fifth rows: same as in the third row but using Σ_{SMF} and Σ_{KT13}.

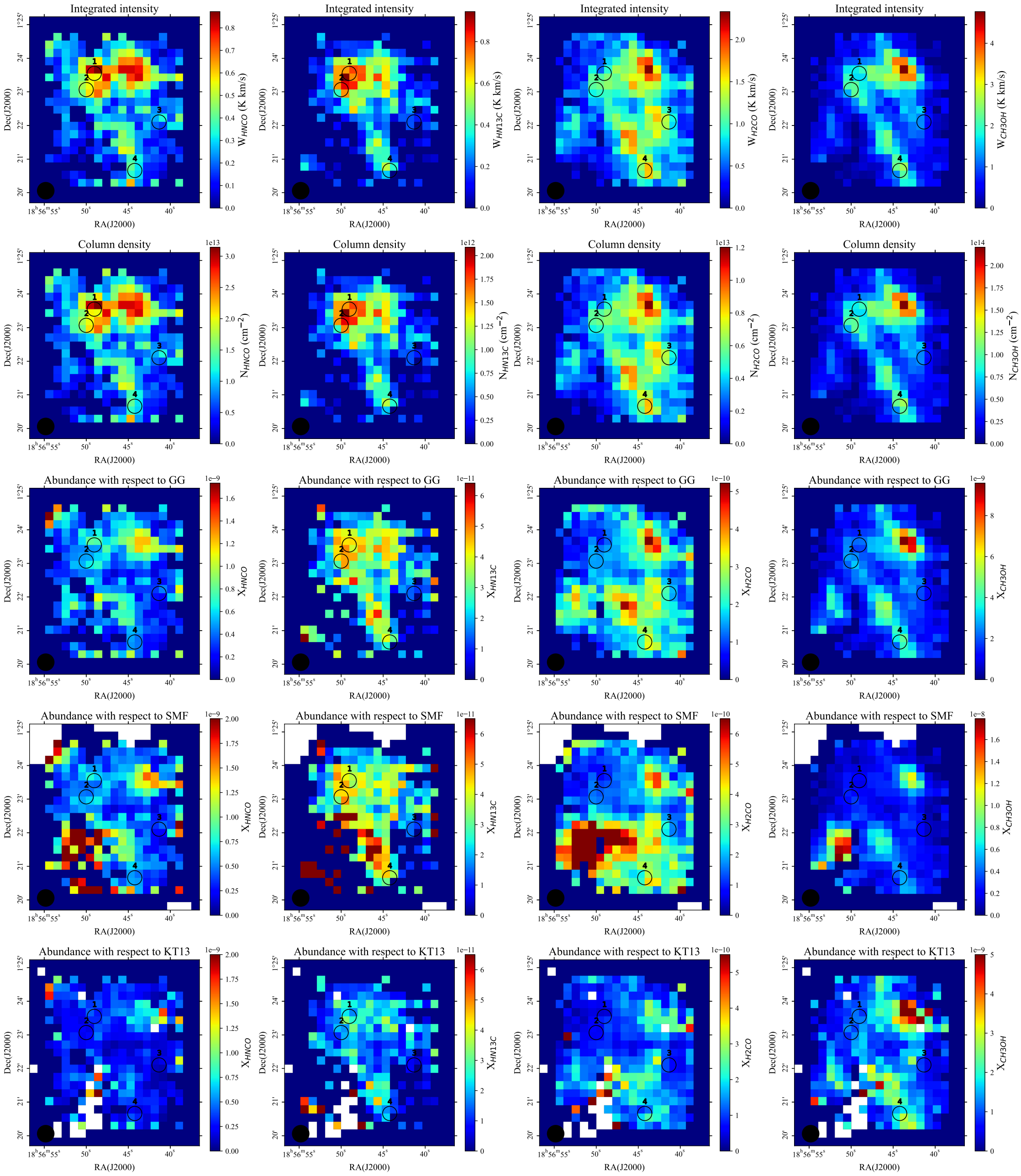

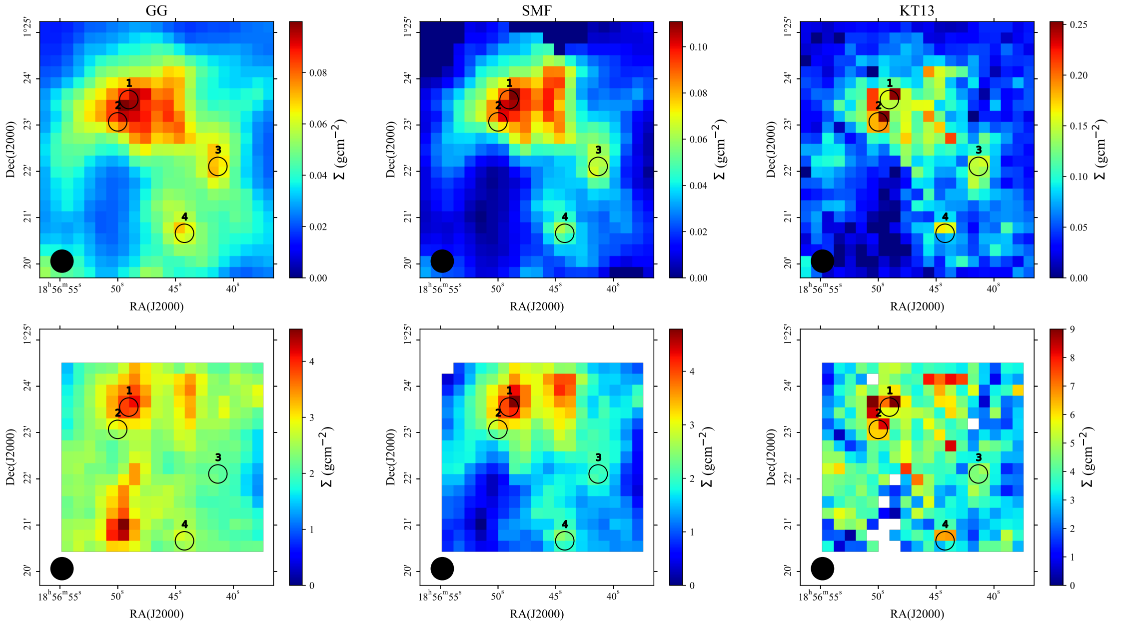

Figure 3.32: Upper row: Mass surface desnity maps:Σ_{GG} (Left), Σ_{SMF} (Middle) and Σ_{KT13} (Right). Bottom row: The respective CO depletion factor map.

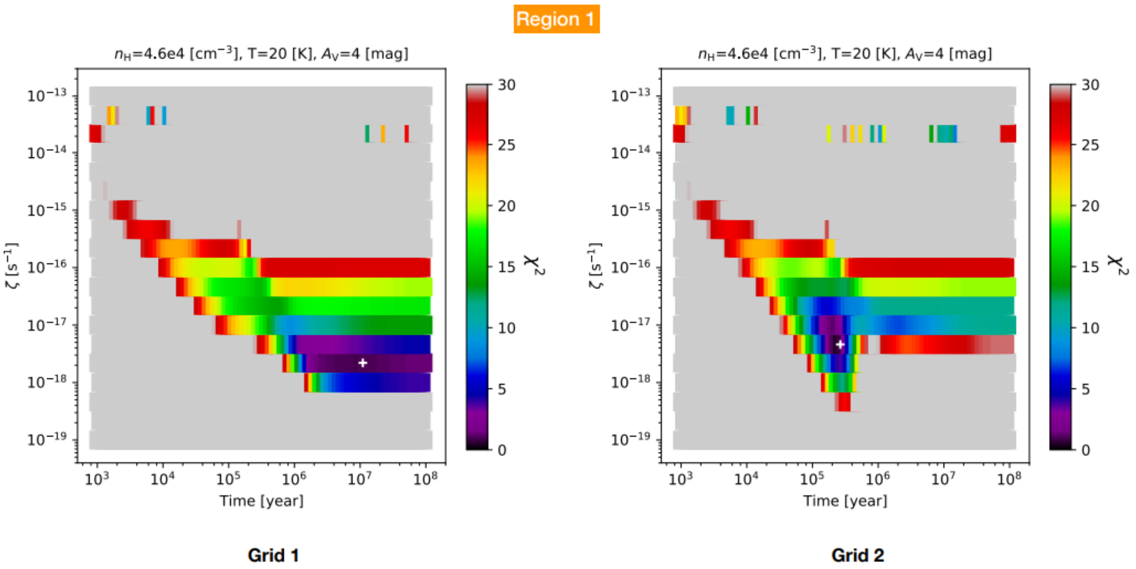

Grid 1

Grid 2

Figure 3.33: Show the minimized χ^2 (based on the abundances of CO, HCO^+ and N_2H^+) for the extreme-restricted search method for region 1.

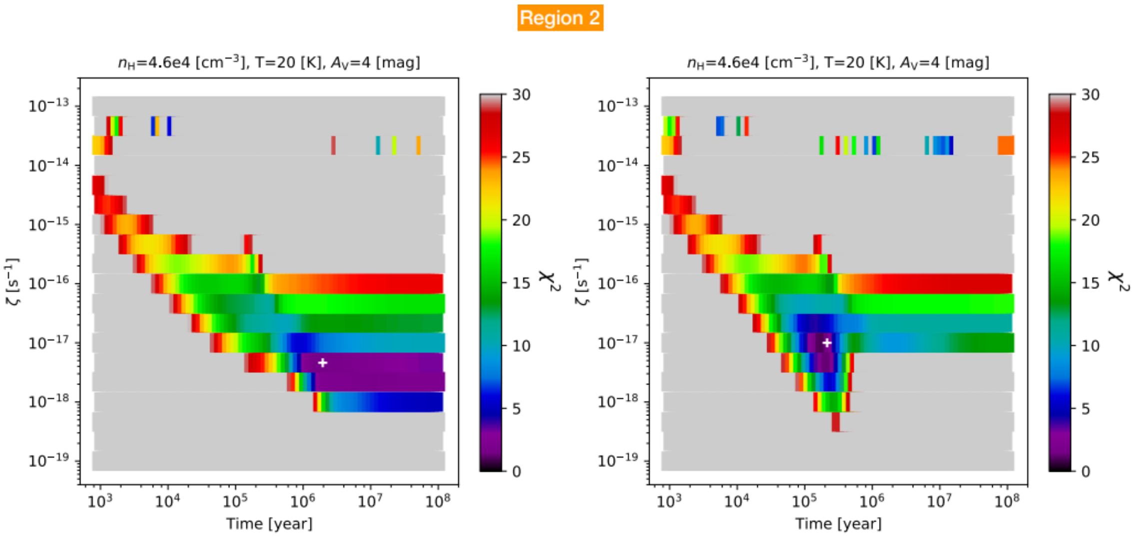

Grid 1

Grid 2

Figure 3.34: Same as for Figure 3.33 but for region 2.

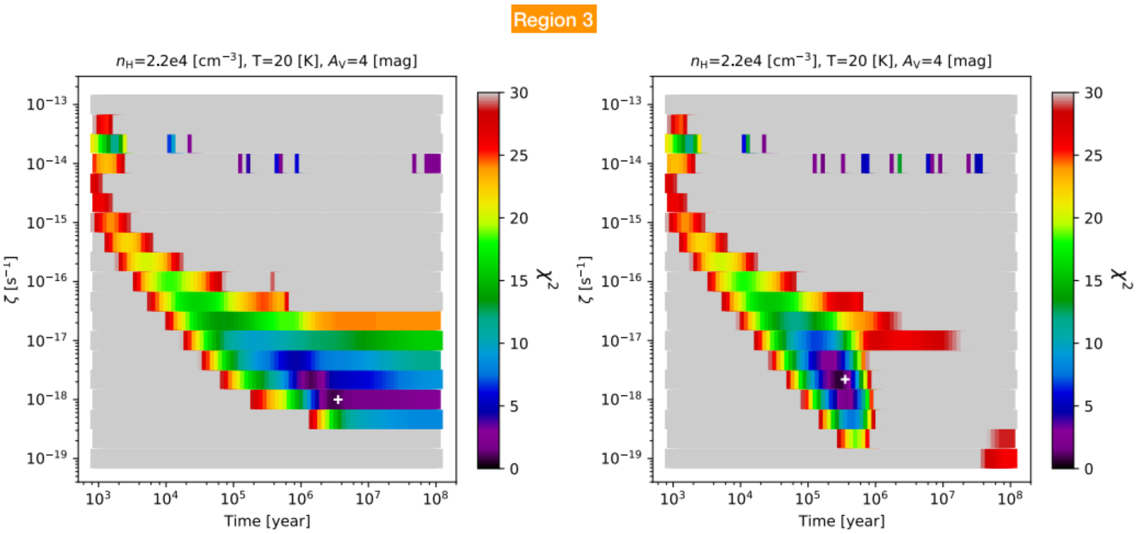

Grid 1

Grid 2

Figure 3.35: Same as for Figure 3.33 but for region 3.

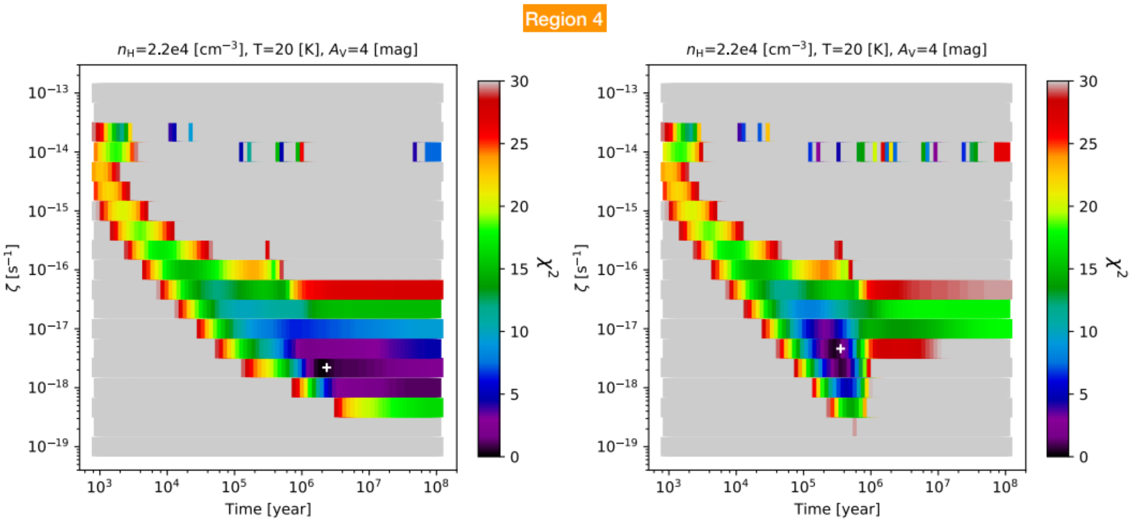

Grid 1 **Grid 2**

Figure 3.36: Same as for Figure 3.33 but for region 4.

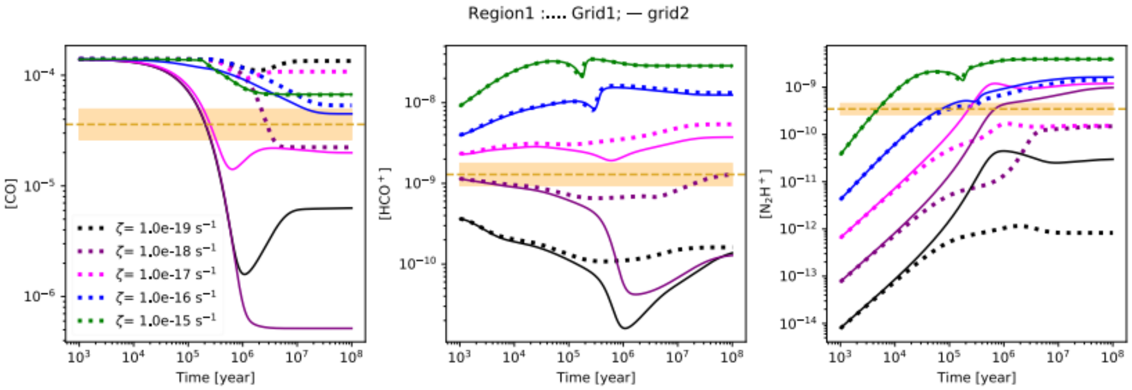

Figure 3.37: Shows the predicted time evolution by the models for [CO] (left panel), [HCO$^+$] (middle panel), and [N$_2$H$^+$] (right panel) based on different CRIR. The solid lines correspond to Grid 2 while the dotted ones correspond to Grid 1. The dotted horizontal line shows the observed abundances from Region 1 for the GG case. The shaded region shows the uncertainties concerning the derived abundances.

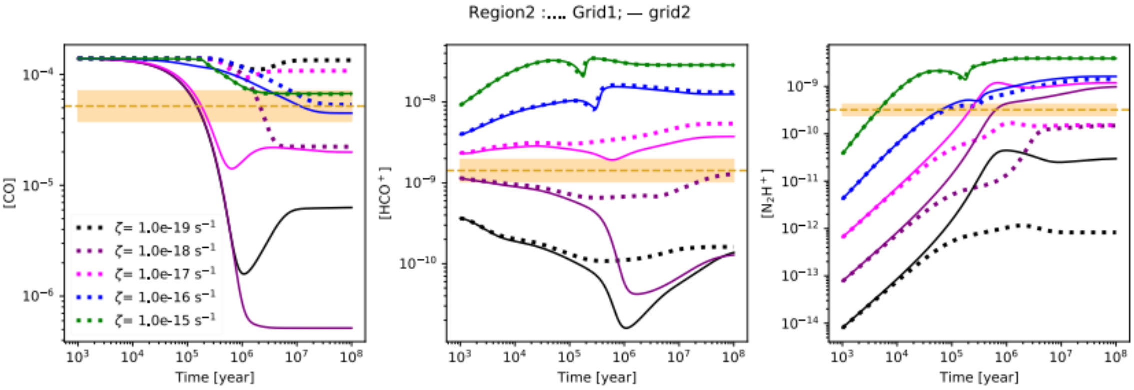

Figure 3.38: Same as for Figure 3.37 but for region 2

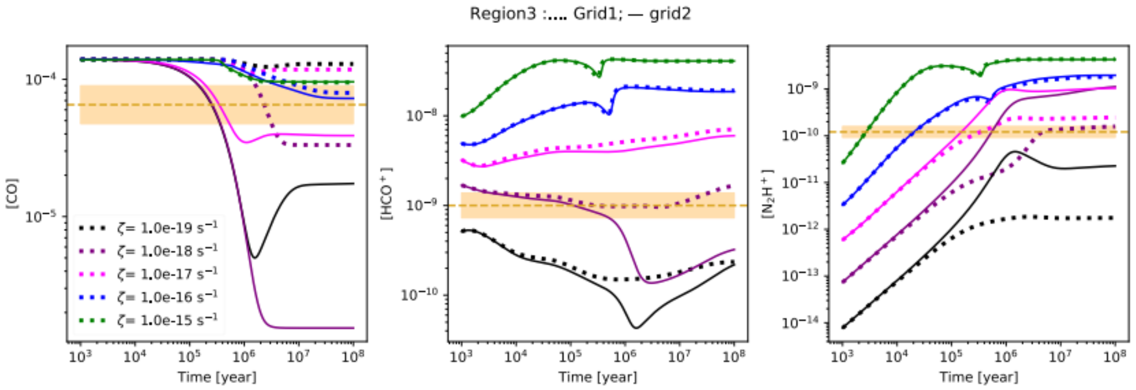

Figure 3.39: Same as for Figure 3.37 but for region 3

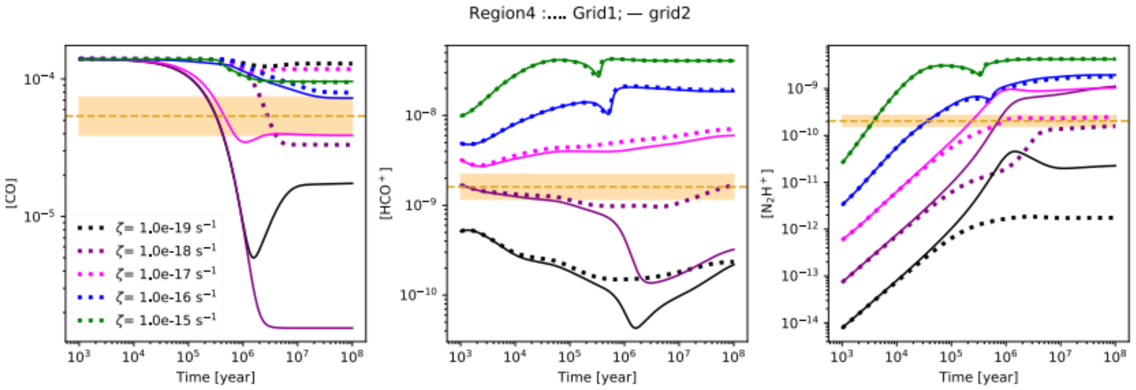

Figure 3.40: Same as for Figure 3.37 but for region 4.

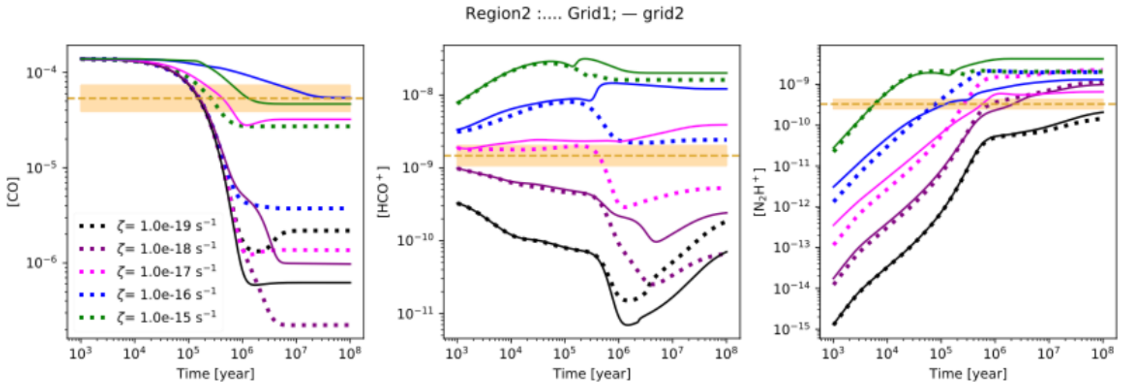

Figure 3.41: Shows the predicted time evolution by the models for [CO] (left panel), [HCO$^+$] (middle panel), and [N$_2$H$^+$] (right panel) based on different CRIR. The solid lines correspond to Grid 2 while the dotted ones correspond to Grid 1. The observed abundances from region 2 for the SMF case are shown by the dotted horizontal line. The uncertainties concerning the derived abundances are shown by the shaded region.

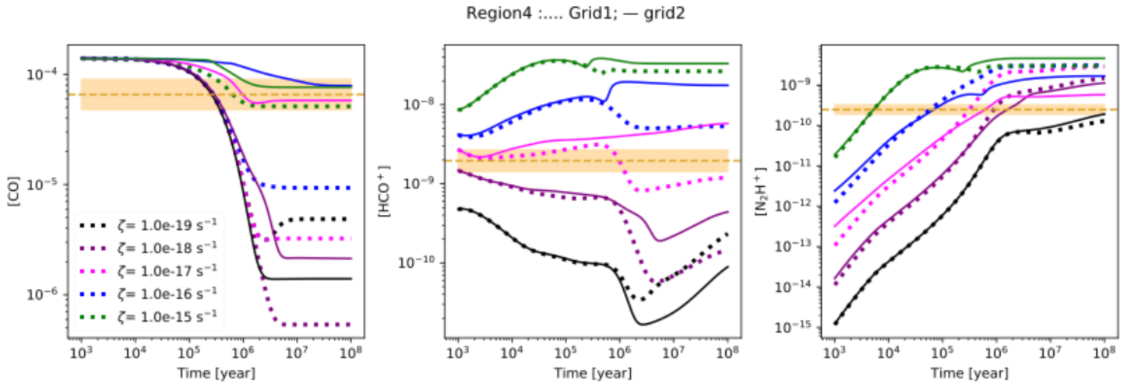

Figure 3.42: Same as for Figure 3.41 but for region 4

4

Discussion

In the following chapter, we discuss the results presented in the previous chapter in the same order. We also discussed made assumptions and uncertainties and how they may affect our results.

4.1 Kinematics

Cloud G showed a complex kinematic structure. The spectra for the different positions in Figure 3.2 show smaller peaks on the main velocity component, which hints at the line profile consisting of multiple Gaussians, indicating the presence of a multiple velocity component structure. The small peaks themselves wouldn't necessarily be classified as distinct peaks.

Looking at the moment 1 maps in Figure 3.7, the upper region of the ring structure showed values for the velocity component, ranging from 43.4 km/s - 44.4 km/s. The exact values for position 1-5 shown in Table 3.1 are slightly higher than the mean velocity of 43.5 km/s (Simon et al. (2006b), Butler & Tan (2009), Butler & Tan (2012), Hernandez & Tan (2015)). The estimated velocity gradient between the center of regions 2 and 3 was roughly 0.36 km/s per parsec. Looking at the bigger picture the values of the velocity components appear quite similar, especially when you compare it to the red-shifted region towards the HII region, ranging from 44.6km/s - 47.0km/s or the blue-shifted region (40.0km/s - 42.8km/s) towards the SNR. It is also within the velocity range of 40.0km/s - 42.8km/s that we observe the presence of the arch from the direction of the SNR in the channel maps.

Neither the ^{13}CO nor the C^{13} spectra extracted from the upper part of the ring structure showed any clear indication of so-called broad wings (see Figure 3.2). This would insinuate that there is a lack of outflow activity from the three cold cores (Sanhueza et al., 2017). Meaning that Cloud G could very well be in the early stages of its evolution where the star formation activity is low. This seems to support the claim made by Cosentino et al. (2018).

4.2 CO Depletion

The CO depletion factor for Cloud G was found to range from 1.5-6 for the instance where it is derived from Σ_{GG} or Σ_{SMF}, and the values are up to twice as large when they are derived from Σ_{KT13}. Our values seem to be in agreement with those presented in Sabatini et al. (2019) and Hernandez et al. (2011), where the depletion values were estimated for the IRDCs G351.77-0.51 and G035.30-00.33. While other studies, such as in Jiménez-Serra et al. (2014) and Entekhabi et al. (2021) reported larger CO depletion values for the IRDCs ranging between 4-12. Fontani et al. (2012) found a broad range of depletion values (5-78) for a set of multiple IRDCs, some of which were significantly higher than the depletion factor obtained in our project. But as it was stated in Tan et al. (2014), the estimated CO depletion factor in IRDCs could be widespread in order.

Additionally, the values obtained from our IRDC appear to be greater in order compared to the more evolved cores that are known to contain massive protostars (Fontani et al., 2006). This was further supported in Giannetti et al. (2014) where the depletion factor was studied as a function of evolution. It was determined that colder cores had a higher CO depletion factor, and they concluded that cores at their earlier evolutionary stage (characterized by a lower temperature) had a larger f_D. We could therefore speculate that our IRDC is at an early stage of evolution.

We observed clear trends for how f_D varies with respect to the dust temperature and the mass surface density of the cloud. The depletion factor showed a positive correlation to the density, indicating that denser regions tend to be more depleted. As reported by Giannetti et al. (2014), the depletion timescale decreases for denser regions. We found an anti-correlation between the depletion factor and the dust temperature which is consistent with what has been discovered in other papers such as for Fontani et al. (2012) that measured a faint anti-correlation. This would indicate that for greater temperatures, a larger number of previously depleted molecules are released into the gas phase. Another prediction is that for temperatures greater than 20 K, CO shouldn't show any signs of depletions, which seems to be in agreement with the CO depletion factors derived from the Σ_{SMF}. The CO depletion factor derived from the Σ_{GG} on the other hand show elevated f_D values for temperature up to 25.5 K.

One discrepancy is that the warm (dust temperature of 33 K), dense core observed in position 6 displayed a large depletion value. Based on Figure 3.18 one would expect that it would show no signs of depletion, as the temperature is greater than the sublimation temperature of CO. It is uncertain what occurs in the core, perhaps some of the carbon towards the core is in other organic molecules rather than as CO. One could also speculate that the large depletion value is due to a poor choice of excitation temperature for the specific region. Similar instances were reported in Giannetti et al. (2014), where warm protostellar envelopes showed signs of depletion (e.g. Fuente et al. 2012), but the reasons remain unclear. Nonetheless, further analysis would be beneficial in order to gain more clarity.

In order to determine the CO depletion for Cloud G, some assumptions were made, all of which contributed to a certain degree of uncertainty. But while the exact CO depletion values reported contain some degree of uncertainty, the order of magnitude can be taken at face value. One important assumption made regarding CO depletion was the assumption that ^{13}CO and C^{18}O were optically thin. We studied the abundance ratio between the two CO isotopologues with the intention to determine whether ^{13}CO was optically thin or thick. Both ^{13}CO and C^{18}O were converted to CO by multiplying with their respective isotopologue ratios, assuming that these constants are correct and that the line emission of ^{13}CO is optically thin, the CO abundances measured from both molecules should more or less be in an agreement with one another. The abundance ratio should therefore roughly equal to $N_{13\mathrm{CO}}/N_{\mathrm{C18O}} \approx 327/49.8 = 6.56$. Now, the abundance ratio observed in Figure 3.8 was estimated to be around 4-8.

Positions 3-5 had an abundance ratio of 6.25, 6.53, and 6.62 respectively, which are fairly close to the theoretical abundance ratio. It is therefore granted that the CO depletion factor from ^{13}CO and C^{18}O appear to be similar for these regions (see Table 3.3). This indicates that the optical depth toward these positions is not significant for the ^{13}CO nor the C^{18}O emission lines. Positions 1, 2 and 6 suggest that the f_D derived from C^{18}O is lower, which seems reasonable, granted that C^{18}O is always optically thin. The abundance ratios for both positions were 5.85 and 4.54, both were below the expected value. One could speculate that this indicates that ^{13}CO is optically thick for these parts of the IRDC, which should be considered for further studies of the cores. For an optically thick part of the cloud, the chances of the emitted photons being absorbed by other surrounding molecules increase, which lowers the probability of the photon escaping from the region, so-called radiative trapping. This would result in an underestimation of the column density of ^{13}CO.

Position 1 was the only region where the depletion factor derived from C^{18}O appeared greater than the one derived from ^{13}CO, and had an abundance ratio of 7.55. This discrepancy is most likely due to the peculiar individual pixel that originated from the integrated intensity map of C^{18}O. It remains however unclear whether position 1 is optically thick as well, seeing how it is in close vicinity to position 2.

Another source of the uncertainties was the choice of excitation temperature. In order to estimate the column densities of each species studied in this project, we assumed a constant excitation temperature throughout the cloud and set it to equal 7.5 K. The assumption that T_{ex}=7.5 K has been utilized by other previous work on IRDC, such as in Hernandez et al. (2011) and Entekhabi et al. (2021). In Cosentino et al. (2018), the excitation temperature was determined to range from 6-11 K for Cloud G. The estimated column density of H^{13}CO^{+}(1-0) was of the same magnitude as the ones estimated in this paper.

In an effort to understand how a constant T_{ex} affects the calculated column density, the excitation temperature was varied by 30% in both directions. The column density varied more drastically for the instance where the temperature was decreased by 30%. In an attempt to minimize the uncertainty in the column density due to the selection of excitation temperature, one could for future studies aim to produce an excitation temperature map by studying two different transitions of the same species. In Sabatini et al. (2019) the excitation temperature for the C^{18}O map of the IRDC G351.77-00.51 was derived from the dust temperature map, using the relation from Giannetti et al. (2017). The relation was only valid for a dust temperature within 10 K to 45 K, making T_{GG} and T_{SMF} eligible candidates.

We would benefit from an estimated excitation temperature map for further studies of the warm dense core in position 6. The dust temperature found for position 6 was greater than those hypothesized for the freeze-out process and was not abiding by the typical trend, where the depletion factor decreased for greater dust temperatures. There is a possibility for radiative trapping. Another effect induced by radiative trapping is that it can increase the level of excitation and in turn enhance the excitation temperature. It is therefore reasonable to assume that the excitation temperature should be greater than 7.5 K for Position 6. By assuming an excitation temperature of 30 K the column density changed by a factor of 1.36 and the depletion factor decreased by 26 %. Similarly, for an excitation temperature of 50 K, the column density increased by a factor of 1.67, which reduced the depletion factor by 40 %

4.3 Virial analysis

We estimated the mass and the virial parameter for regions 1-4 and determined that none of the regions were gravitationally bounded. This would suggest that the forces acting outwards are greater than the gravitational potential energy which would in turn prevent the regions from collapsing inwards and forming massive stars.

Previous studies such as Kainulainen & Tan (2013) estimated the virial parameter for Cloud G as a whole was equal to 4.7 implying that the cloud itself was gravitationally unbounded as well, and out of all the IRDC studied, Cloud G had the highest α_{vir} parameter. Larson's first law states that the motion of giant molecular clouds is described as being chaotic, where the velocity dispersion is expected to increase with the cloud size. Cloud G seems to deviate from this trend in a sense. Out of the ten studied IRDC in Butler & Tan (2012), Cloud G had the third smallest effective radius (3.06 pc) and the second highest velocity dispersion (2.95 km/s) which was derived by fitting a gaussian to the spectra from the region enclosed inside of the ellipsoid (Kainulainen & Tan, 2013). The velocity dispersion could have been enhanced by the shocks from the HII region and the supernova remnant.

Nevertheless α_{vir} for the whole cloud was much lower than the values obtained for the individual regions. Another study conducted by Liu et al. (2014) observed 12 northern IRDCs (Cloud G was not among the observed IRDC, but the IRDC G034.43+00.24 (Cloud F) and G038.95-00.47 (Cloud I) were), using the emission lines of ^{13}CO(1-0) and C^{18}O(1-0). They arrived at the conclusion that 57.5% of the 41 IRDC cores in the paper were gravitationally bound. The α_{vir} parameter was in this case defined as a ratio between the virial mass and the mass of the cores. Most of the cores in Cloud F had a virial parameter between 0.5 to 2.

Now we only performed a rough virial analysis in this paper and there could be several uncertainties that contributed to the high value of α_{vir} for cloud G. For three out of the four regions considered were believed to contain a cold dense core within them. The radius of each region was set to equal 0.22 pc which is greater than the radius of the cold dense cores mentioned in Butler & Tan (2012). When we determine the average density for each region, we include the mass surface density of both the core and the region around it, which in turn could result in a dilution of the average density value. The average mass surface density was obtained for a region consisting of 11 × 11 pixels. The area for each pixel was estimated to be

$2.75'' \times 2.75''$ (area of 0.0015 pc^2). The area confined within a radius of 0.22 pc consists of 101 pixels, meaning that the circular area only corresponds to 83% of the total area used. The determined mass is therefore underestimated (should be 1.16 times greater) and the virial parameter in the table in the method is overestimated.

Besides the radius, we can observe in Figure 3.24 that the choice of which mass surface density map is utilized also affects the final result. The only parameter that varied was the mass (the velocity dispersion was estimated from the emission lines of ^{13}CO(1-0) and $C^{18}O$(1-0)) which in turn was a direct reflection of the mass surface density since the area of the region also remained constant. The values from Σ_{KT13} were more than twice as large compared to the values from the two other Σ maps, which resulted in lower values for the virial parameters.

The velocity dispersion measured in our case ranged between 2.2-2.4 km/s for ^{13}CO and between 1.7-2.0 km/s for $C^{18}O$. The lower values of σ for $C^{18}O$ is the single reason why the virial parameters are smaller for $C^{18}O$ than ^{13}CO.

4.4 Additional abundances and astrochemical modeling

The molecular abundances measured in this project (see Table 3.6 and 3.7) were, in general, greater by a factor of 2.1-3.3 than those reported in Entekhabi et al. (2021). Specifically, the CO abundance, which was roughly $5 \cdot 10^{-5}$, was approximately 2.5 times greater than that for the other IRDC in the Butler & Tan (2012) sample, i.e., Cloud C. The overall HCO^+ and N_2H^+ abundances were also greater by a factor of 3.3 and 2.5 compared to those in Entekhabi et al. (2021), even though Cloud C was slightly denser. All of which could point to Cloud G having a higher CRIR.

One significant difference between the input parameters used in this project compared to those applied in Entekhabi et al. (2021), is the dust temperature value, which was set to 15 K for the SMF instance and 20 K for the GG instance. Compared to Entekhabi et al. (2021), the models that were run for Cloud C focused solely on a temperature of 15 K. The enhancement of the abundances derived from the Σ_{GG} could simply be a byproduct of a higher dust temperature. The abundances derived from the Σ_{SMF} were of similar order as those determined from Σ_{GG}, but the regions of interest showed dust temperatures of 15 K, consistent with the temperatures reported in Entekhabi et al. (2021). One could therefore speculate that the observed regions have a higher CRIR, meaning that the presence of the SNR and the HII region might affect the chemical properties of the IRDC. The input temperature was varied in Entekhabi et al. (2021) to illustrate how crucial the choice of dust temperature is. The model with 15 K preferred earlier timescales and the model with 20 K later timescales. This appears to be reasonable, seeing as 20 K is close to the CO sublimation limit. As recalled from the introduction CO tends to freeze for temperatures below 20 K.

The average CRIR in this project was estimated to be $2.5 \cdot 10^{-18}$ s^{-1} (GG) and $6.7 \cdot 10^{-18}$ s^{-1} (SMF) for Grid 1 (see Table 3.8). As hypothesized, the CRIR is greater for the model derived from Σ_{SMF}, while for Grid 2, the CRIR was identical in both cases for the four regions, with an average CRIR of $5.35 \cdot 10^{-18}$ s^{-1} (see Table 3.9). We can also observe that the models derived from Σ_{SMF} favor earlier time scales of the order 3.8-7.6$\cdot 10^5$. The chemical time estimated from the Σ_{GG} varies between the two grid models, grid 1 favors later time scales while grid 2 prefers earlier time scales.

In Entekhabi et al. (2021), the author also brought forward the possibility that the envelope gas could contaminate the estimated CO emission along the line-of-sight and set the contamination level of the cloud to 90%. If we were to consider a contamination level of 50%, the CO abundance would be decreased by a factor of 2, which would enhance the values of the CO depletion and abundance ratio presented in 3.43. The elevated values for [HCO^+]/[CO] would give rise to a higher CRIR, while the CO depletion and [N_2H^+]/[CO] favors $2.2 \cdot 10^{18}$ s^{-1}. One could speculate that the contaminated data would all favor the later-time solutions, regardless of whether the abundances were derived from Σ_{GG} or Σ_{SMF}. But we were not able to estimate a higher CRIR value by simply considering the CO contamination.

The author states that a lack of scattering was observed in the data points for the CO depletion factor versus density relation would suggest that the CO envelope contamination is negligible. We only observed four regions, we would therefore need more points data in order to establish whether the degree of CO contamination is negligible for cloud G. The relation between the CO depletion factor and the mass surface density was illustrated in Figure 3.18 observed with the GBT towards the region mapped by IRAM-30m telescope. If we complement the data points from the IRAM-30m with those from the GBT, the CO depletion vs density plot derived from the ^{13}CO(1-0) shows very little to no scattering, while $C^{18}O$(1-0) exhibits a more significant scattering among the values.

We can recall that the main differences between the astrochemical model grids were the assumed values for the CO ice binding energies and the inclusion of the Cosmic Ray-induced thermal desorption for Grid 2. In Entekhabi et al. (2021), it was concluded that a lack of scattering in the CO depletion-density relation seems to favor solutions that were deemed to be insensitive to the dust temperature, and rather relied on the cosmic ray-induced desorption. This could explain why the CRIR values were similar for the two cases (GG and SMF) when the cosmic ray-induced desorption mechanisms were included even though the input temperature was different. As the cosmic rays impact the dust grains, the energetic impact heats up the material and contributes to the desorption of the molecules that were previously depleted on the dust surface. We would therefore expect it to lower the CO depletion, and since cloud G is in the presence of both a HII region and an SNR, the cosmic ray-induced desorption could play a large role. An increase in the CO abundance could further increase the HCO^+ abundance, which so far has constrained the models to a lower CRIR.

The estimated CRIR for cloud G was greater than the average value from Entekhabi et al. (2021) ($2.44 \cdot 10^{-18}$ s^{-1}) by a factor of 1-2.74, but it was still significantly smaller than those measured for the diffuse interstellar medium and star-forming regions. One had hoped for higher values for CRIR since cloud G lies near a supernova remnant and a HII region. The highest CRIR values were found near HII rather than the supernova remnant. The shocks produced by supernovas are in general greater than those from a HII region. The fact that the CRIR values are slightly higher in positions 1 and 2, could imply that the supernova remnant has not had a great impact on the astrochemistry of the IRDC as of yet.

5

Conclusion

We studied how the physical and chemical conditions of the IRDC G34.77-0.55 were impacted by the presence of the SNR W44 and the HII region G34.8-0.7. The line emission of ^{13}CO(1-0) and C^{18}O(1-0) were observed towards the IRDC and its surroundings using the Green Bank Telescope (GBT). Additional molecular line species tracing higher density conditions were also observed using the Instituto de Radioastronomia Milimetrica (IRAM) 30m telescope. We also utilized the mass surface density and dust temperature maps derived from archival Spitzer and Herschel Space Telescope data.

With these data, we measured the abundances of various species, especially CO, HCO$^+$, and N$_2$H$^+$. We furthermore present maps of the CO depletion factor, which measures the extent to which CO freezes out from the gas phase to form CO ice coatings on dust grains and study how it depends on physical conditions. We conclude that the CO depletion factor ranged from 1.5-6 and that the CO depletes more efficiently in cold, dense regions. One discrepancy is that the warm (33 K) dense core observed displayed a large depletion value, the reasoning behind this remains unclear. Nonetheless, further analysis is required. We have discussed the methodology used to derive the depletion factor and the impact that it may have on the result, such as the choice of a constant excitation temperature and isotopologue ratios, and the assumption that ^{13}CO and C^{18}O were optically thin.

The measured abundances of CO, HCO$^+$, and N$_2$H$^+$ were furthermore used for astrochemical modeling to constrain the age of the cloud to be $\sim 10^5$ - 10^6 yrs and the cosmic ray ionization rate (CRIR) $\sim 10^{-17}\mathrm{s}^{-1}$. This CRIR is several times larger than that inferred by identical methods in another IRDC, which may indicate that G34.77-0.55 is impacted by the W44 SNR and HII region G34.8-0.7. However, the overall rate is still significantly lower than that of the diffuse ISM.

We also carried out a kinematical analysis of the GBT observational data. The first moment maps revealed a velocity gradient from high (more redshifted) to low (more blueshifted) values from the HII region side to the SNR side. This may indicate that the IRDC is located beyond the HII region and in front of the SNR. The line emission spectra of ^{13}CO nor the C^{13} extracted from the from positions in the northern part of the ring structure showed no clear indication of broad wings, suggesting that there is a lack of outflow activity from the three cold cores. Supporting the notion that G34.77-0.55 may be in the early stages of its evolution where the star formation activity is low.

Lastly, we perform a roughly virial analysis on positions 1-4 and concluded that none of the regions were gravitationally bounded.

Bibliography

Ackermann, M., Ajello, M., Allafort, A., et al. 2013, Science, 339, 807, doi: 10.1126/science.1231160

Agertz, O., Kravtsov, A. V., Leitner, S. N., & Gnedin, N. Y. 2013, , 770, 25, doi: 10.1088/0004-637X/770/1/25

Ballesteros-Paredes, J., Hartmann, L., & Vazquez-Semadeni, E. 1999, The Astrophysical Journal, 527, 285, doi: 10.1086/308076

Bally, J. 2010, Proceedings of the International Astronomical Union, 6, 247–254, doi: 10.1017/S1743921311000469

Battersby, C., Bally, J., Jackson, J. M., et al. 2010, , 721, 222, doi: 10.1088/0004-637X/721/1/222

Bell, A. R. 1978, Monthly Notices of the Royal Astronomical Society, 182, 147, doi: 10.1093/mnras/182.2.147

Bergin, E. A., & Tafalla, M. 2007, , 45, 339, doi: 10.1146/annurev.astro.45.071206.100404

Bertoldi, F., & McKee, C. F. 1992, , 395, 140, doi: 10.1086/171638

Butler, M. J., & Tan, J. C. 2009, , 696, 484, doi: 10.1088/0004-637X/696/1/484

—. 2012, The Astrophysical Journal, 754, 5, doi: 10.1088/0004-637X/754/1/5

Carey, S. J., Feldman, P. A., Redman, R. O., et al. 2000, , 543, L157, doi: 10.1086/317270

Caselli, P., Walmsley, C. M., Zucconi, A., et al. 2002, The Astrophysical Journal, 565, 344, doi: 10.1086/324302

Chira, R.-A., Beuther, H., Linz, H., et al. 2013, Astronomy &amp: Astrophysics, 552, A40, doi: 10.1051/0004-6361/201219567

Cosentino, G., Jiménez-Serra, I., Henshaw, J. D., et al. 2018, Monthly Notices of the Royal Astronomical Society, 474, 3760, doi: 10.1093/mnras/stx3013

Cosentino, G., Jiménez-Serra, I., Caselli, P., et al. 2019, The Astrophysical Journal, 881, L42, doi: 10.3847/2041-8213/ab38c5

Cosentino, G., Jiménez-Serra, I., Tan, J. C., et al. 2022, Monthly Notices of the Royal Astronomical Society, 511, 953, doi: 10.1093/mnras/stac070

Egan, M. P., Shipman, R. F., Price, S. D., et al. 1998, , 494, L199, doi: 10.1086/311198

Entekhabi, N., Tan, J. C., Cosentino, G., et al. 2021, Astrochemical modelling of infrared dark clouds, arXiv, doi: 10.48550/ARXIV.2111.05379

Fontani, F., Caselli, P., Crapsi, A., et al. 2006, Astronomy &amp Astrophysics, 460, 709, doi: 10.1051/0004-6361:20066105

Fontani, F., Giannetti, A., Beltrá n, M. T., et al. 2012, Monthly Notices of the Royal Astronomical Society, 423, 2342, doi: 10.1111/j.1365-2966.2012.21043.x

Fontani, F., Ceccarelli, C., Favre, C., et al. 2017, , 605, A57, doi: 10.1051/0004-6361/201730527

Foster, J. B., Arce, H. G., Kassis, M., et al. 2014, The Astrophysical Journal, 791, 108, doi: 10.1088/0004-637x/791/2/108

Frost, A. J., Oudmaijer, R. D., de Wit, W. J., & Lumsden, S. L. 2021, Astronomy &amp: Astrophysics, 648, A62, doi: 10.1051/0004-6361/202039748

Fukui, Y., Habe, A., Inoue, T., Enokiya, R., & Tachihara, K. 2020, Publications of the Astronomical Society of Japan, 73, S1, doi: 10.1093/pasj/psaa103

Garrod, R. T., Widicus Weaver, S. L., & Herbst, E. 2008, , 682, 283, doi: 10.1086/588035

Giannetti, A., Leurini, S., Wyrowski, F., et al. 2017, Astronomy &amp: Astrophysics, 603, A33, doi: 10.1051/0004-6361/201630048

Giannetti, A., Wyrowski, F., Brand, J., et al. 2014, Astronomy &amp Astrophysics, 570, A65, doi: 10.1051/0004-6361/201423692

Hartmann, L., Ballesteros-Paredes, J., & Bergin, E. A. 2001, The Astrophysical Journal, 562, 852, doi: 10.1086/323863

Hasegawa, T. I., & Herbst, E. 1993, Monthly Notices of the Royal Astronomical Society, 261, 83

Heitsch, F., Hartmann, L. W., Slyz, A. D., Devriendt, J. E. G., & Burkert, A. 2008, The Astrophysical Journal, 674, 316, doi: 10.1086/523697

Hernandez, A. K., & Tan, J. C. 2015, The Astrophysical Journal, 809, 154, doi: 10.1088/0004-637x/809/2/154

Hernandez, A. K., Tan, J. C., Caselli, P., et al. 2011, The Astrophysical Journal, 738, 11, doi: 10.1088/0004-637x/738/1/11

Heyer, M., & Dame, T. M. 2015, , 53, 583, doi: 10.1146/annurev-astro-082214-122324

Hillas, A. M. 2005, Journal of Physics G: Nuclear and Particle Physics, 31, R95, doi: 10.1088/0954-3899/31/5/r02

Jiménez-Serra, I., Martín-Pintado, J., Caselli, P., Viti, S., & Rodríguez-Franco, A. 2009, , 695, 149, doi: 10.1088/0004-637X/695/1/149

Jiménez-Serra, I., Martín-Pintado, J., Rodríguez-Franco, A., & Martín, S. 2005, , 627, L121, doi: 10.1086/432467

Jiménez-Serra, I., Caselli, P., Fontani, F., et al. 2014, Monthly Notices of the Royal Astronomical Society, 439, 1996, doi: 10.1093/mnras/stu078

Kainulainen, J., & Tan, J. C. 2013, Astronomy & Astrophysics, 549, A53, doi: 10.1051/0004-6361/201219526

Lacy, J. H., Knacke, R., Geballe, T. R., & Tokunaga, A. T. 1994, , 428, L69, doi: 10.1086/187395

Leitherer, C., Schaerer, D., Goldader, J. D., et al. 1999, , 123, 3, doi: 10.1086/313233

Leroy, A. K., Walter, F., Sandstrom, K., et al. 2013, The Astronomical Journal, 146, 19, doi: 10.1088/0004-6256/146/2/19

Lim, W., Tan, J. C., Kainulainen, J., Ma, B., & Butler, M. J. 2016, The Astrophysical Journal, 829, L19, doi: 10.3847/2041-8205/829/1/l19

Liu, X.-L., Wang, J.-J., & Xu, J.-L. 2014, Monthly Notices of the Royal Astronomical Society, 443, 2264, doi: 10.1093/mnras/stu1268

McElroy, D., Walsh, C., Markwick, A., et al. 2013, , 550, A36, doi: 10.1051/0004-6361/201220465

Molinari, S., Schisano, E., Elia, D., et al. 2016, Astronomy &amp Astrophysics, 591, A149, doi: 10.1051/0004-6361/201526380

Neufeld, D. A., & Wolfire, M. G. 2017, The Astrophysical Journal, 845, 163, doi: 10.3847/1538-4357/aa6d68

Perault, M., Omont, A., Simon, G., et al. 1996, , 315, L165

Peretto, N., & Fuller, G. A. 2010, , 723, 555, doi: 10.1088/0004-637X/723/1/555

Rathborne, J. M., Jackson, J. M., & Simon, R. 2006, The Astrophysical Journal, 641, 389, doi: 10.1086/500423

Sabatini, G., Giannetti, A., Bovino, S., et al. 2019, Monthly Notices of the Royal Astronomical Society, 490, 4489, doi: 10.1093/mnras/stz2818

Sanhueza, P., Jackson, J. M., Zhang, Q., et al. 2017, The Astrophysical Journal, 841, 97, doi: 10.3847/1538-4357/aa6ff8

Sashida, T., Oka, T., Tanaka, K., et al. 2013, The Astrophysical Journal, 774, 10, doi: 10.1088/0004-637x/774/1/10

Silsbee, K., & Ivlev, A. V. 2020, The Astrophysical Journal Letters, 902, L25, doi: 10.3847/2041-8213/abbc20

Simon, R., Jackson, J. M., Rathborne, J. M., & Chambers, E. T. 2006a, The Astrophysical Journal, 639, 227, doi: 10.1086/499342

Simon, R., Rathborne, J. M., Shah, R. Y., Jackson, J. M., & Chambers, E. T. 2006b, The Astrophysical Journal, 653, 1325, doi: 10.1086/508915

Tan, J. C., Beltrá n, M. T., Caselli, P., et al. 2014, in Protostars and Planets VI (University of Arizona Press), doi: 10.2458/azu_uapress_9780816531240-ch007

Tan, J. C., Kong, S., Butler, M. J., Caselli, P., & Fontani, F. 2013, The Astrophysical Journal, 779, 96, doi: 10.1088/0004-637x/779/2/96

van Dishoeck, E. F., & Black, J. H. 1988, , 334, 771, doi: 10.1086/166877

Vasyunina, T., Linz, H., Henning, T., et al. 2011, Astronomy &amp: Astrophysics, 527, A88, doi: 10.1051/0004-6361/201014974

Vaupré, S., Hily-Blant, P., Ceccarelli, C., et al. 2014, , 568, A50, doi: 10.1051/0004-6361/201424036

Walsh, C., Nomura, H., & van Dishoeck, E. 2015, Astronomy &amp Astrophysics, 582, A88, doi: 10.1051/0004-6361/201526751

Wilson, T. L., & Rood, R. 1994, , 32, 191, doi: 10.1146/annurev.aa.32.090194.001203

Wootten, A. 1978, The moon and the planets, 19, 163, doi: 10.1007/BF00896988

Zeng, S., Jimé nez-Serra, I., Cosentino, G., et al. 2017, Astronomy &amp Astrophysics, 603, A22, doi: 10.1051/0004-6361/201630210

Zhang, C., Ren, Z., Wu, J., et al. 2020, Monthly Notices of the Royal Astronomical Society, 497, 793, doi: 10.1093/mnras/staa1958

A

Appendix

A.0.1 Regridding

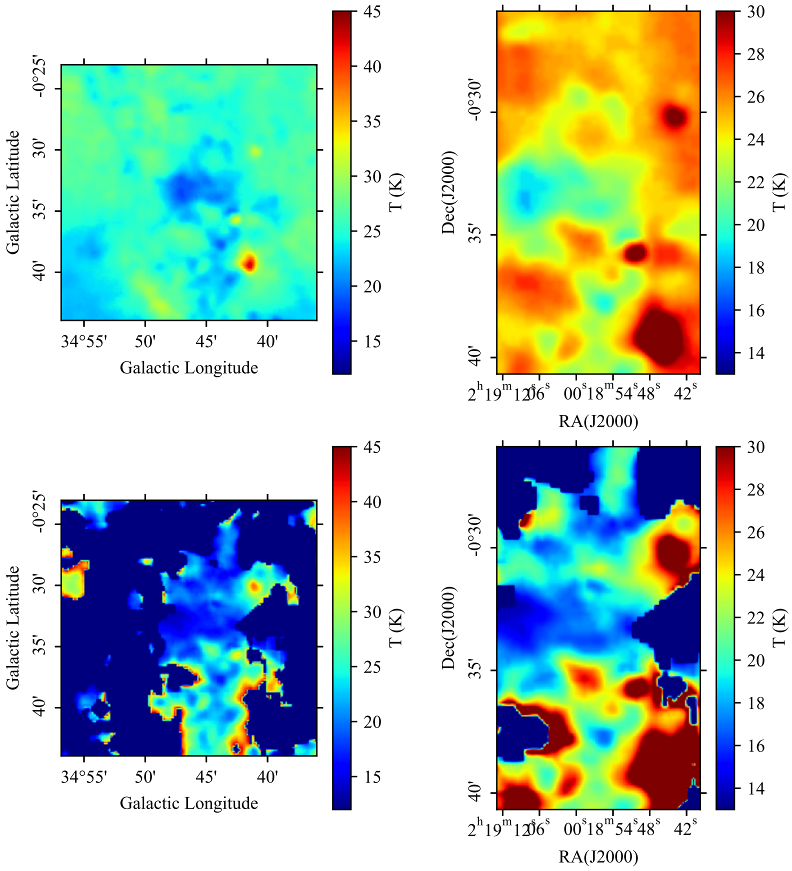

Figure A.1: Regridding of the original T maps to match the header of the GBT data

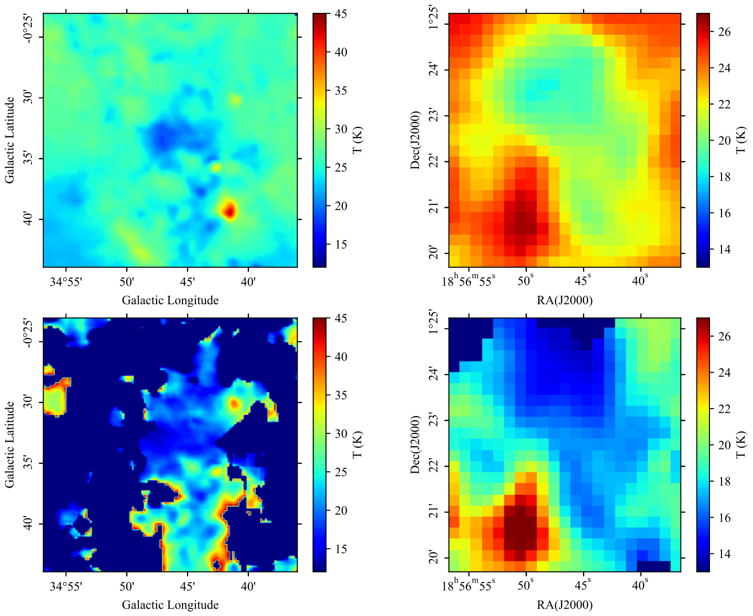

Figure A.2: Regridding of the original T maps to match the header of the IRAM data

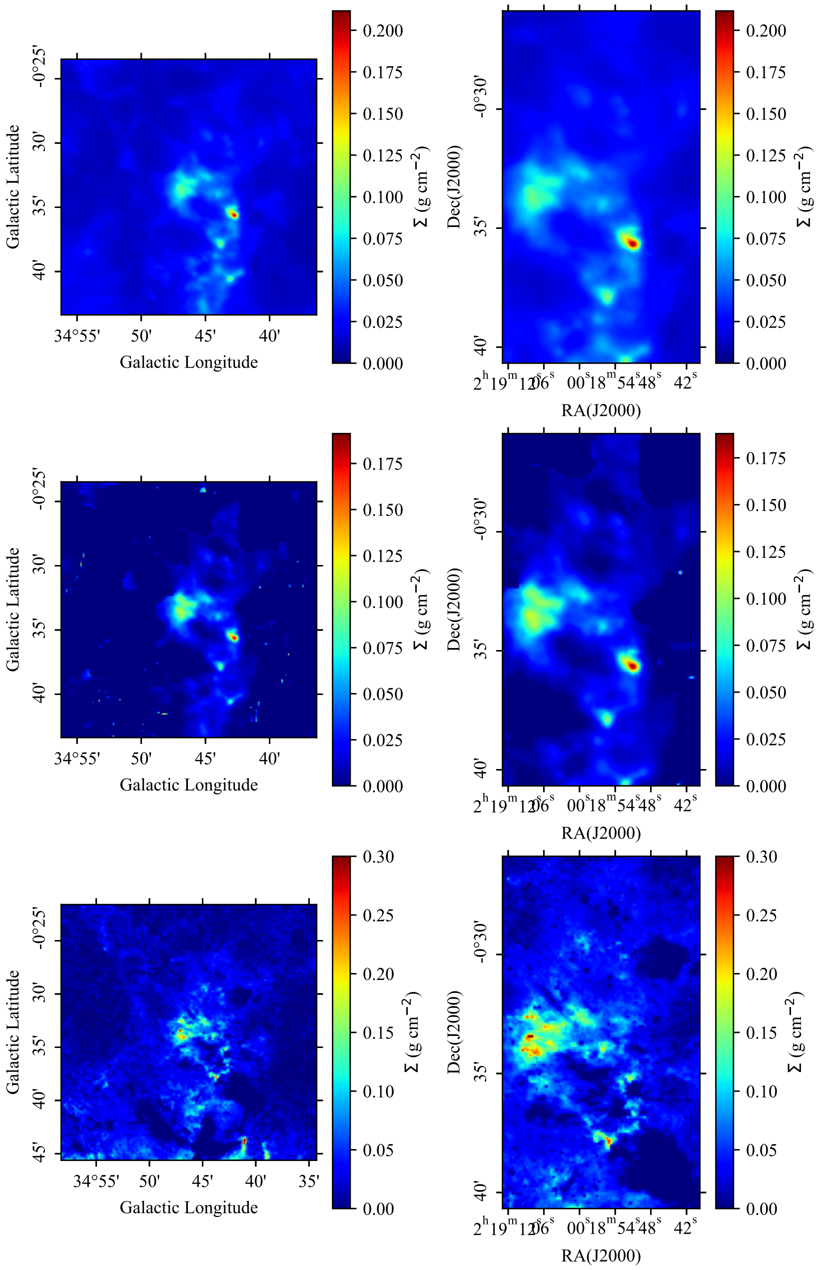

Figure A.3: Regridding of the original Σ maps to match the header of the GBT data

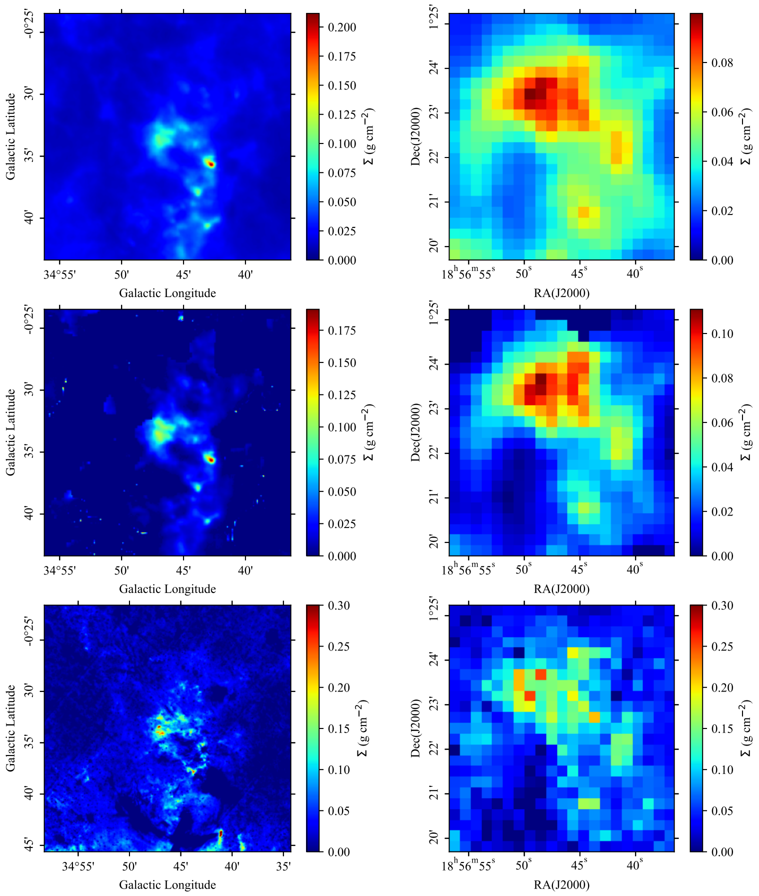

Figure A.4: Regridding of the original Σ maps to match the header of the IRAM data

A.0.2 Additional CO depletion maps

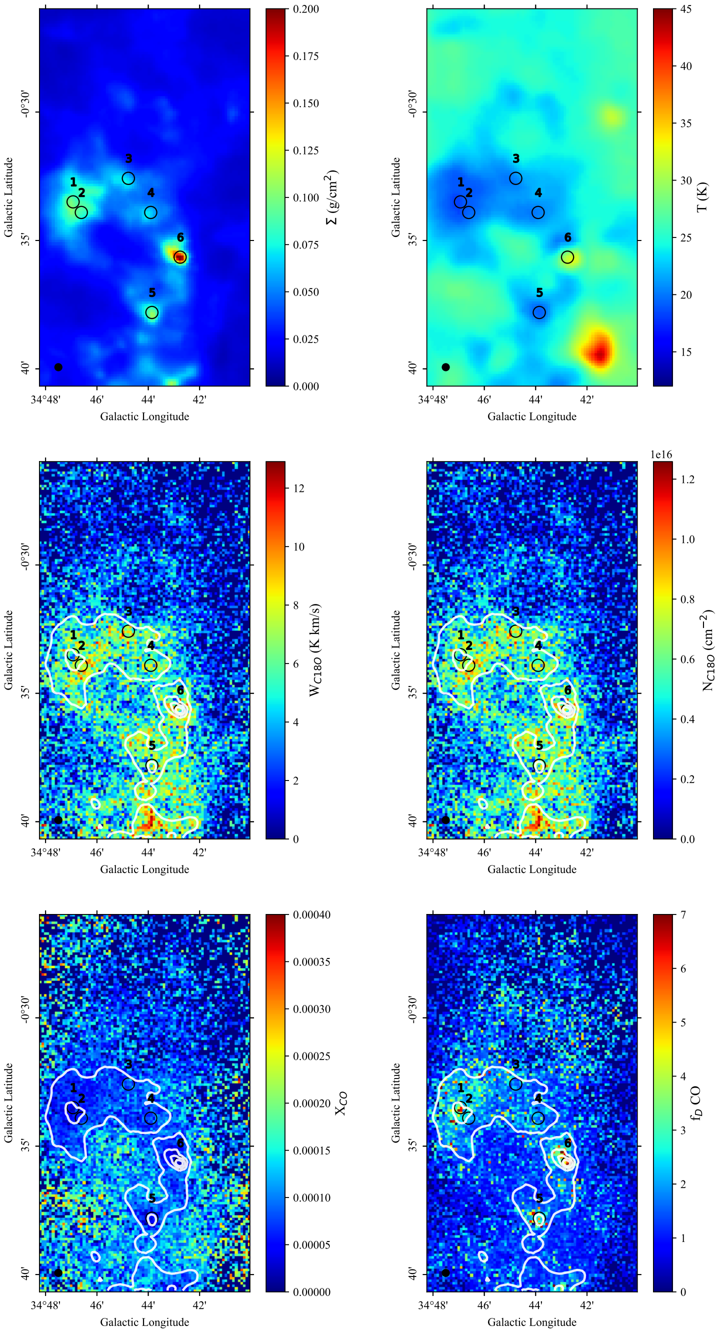

Figure A.5: Top left: the mass surface density obtained with the GG method. Top right: the dust temperature map for the GG method. Middle left: the integrated intensity of $C^{18}O$ over the integration range 36-52.5 km/s. Middle right: the corresponding column density of $C^{18}O$. Bottom left: the corresponding abundance of $C^{18}O$. Bottom right: the depletion factor of CO. The mass surface density is overlayed on top of the middle and bottom rows as white contours. The maps had a pixel size of 6 arcsec.

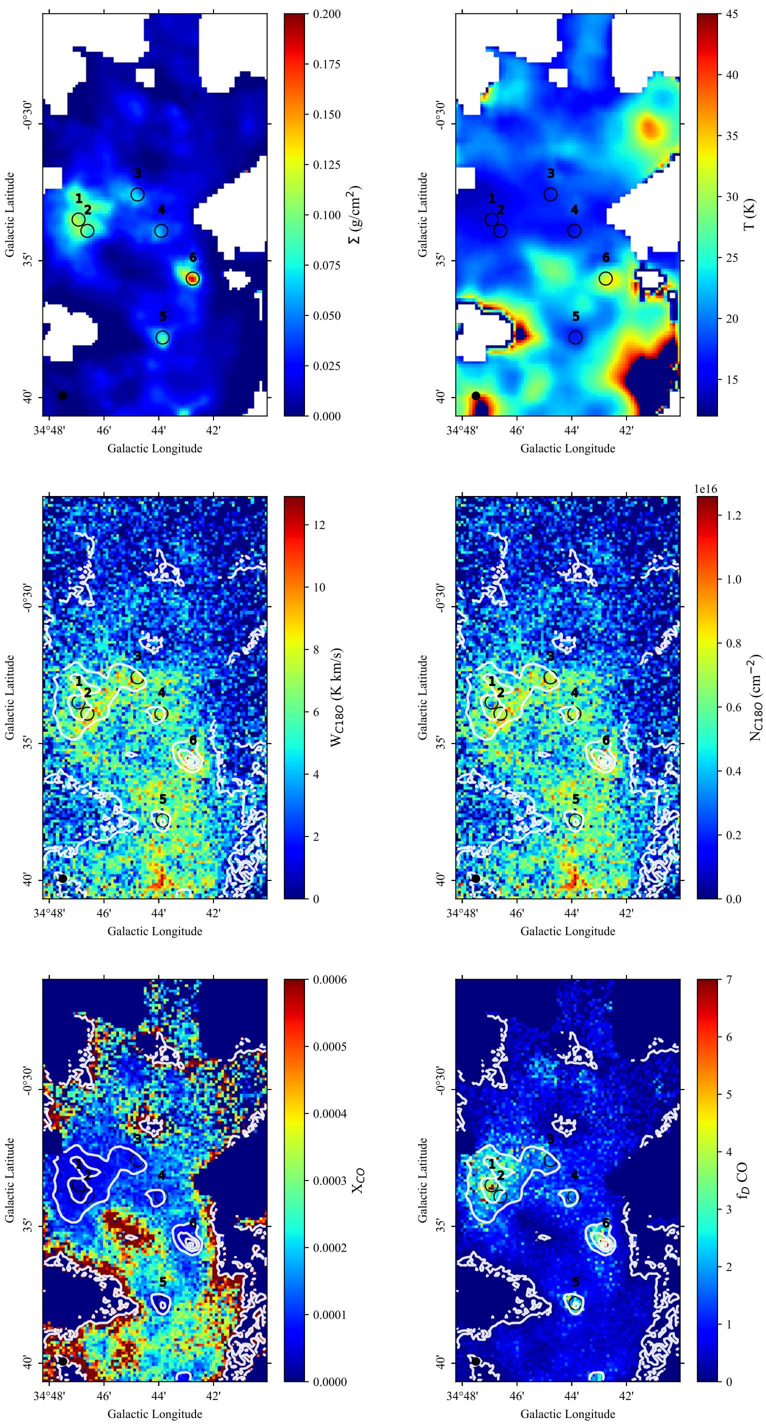

Figure A.6: Top left: the mass surface density obtained with the SMF method. Top right: the dust temperature map for the SMF method. Middle left: the integrated intensity of C^{18}O over the integration range 36-52.5 km/s. Middle right: the corresponding column density of C^{18}O. Bottom left: the corresponding abundance of C^{18}O. Bottom right: the depletion factor of CO. The mass surface density is overlayed on top of the middle and bottom rows as white contours. The maps had a pixel size of 6 arcsec.

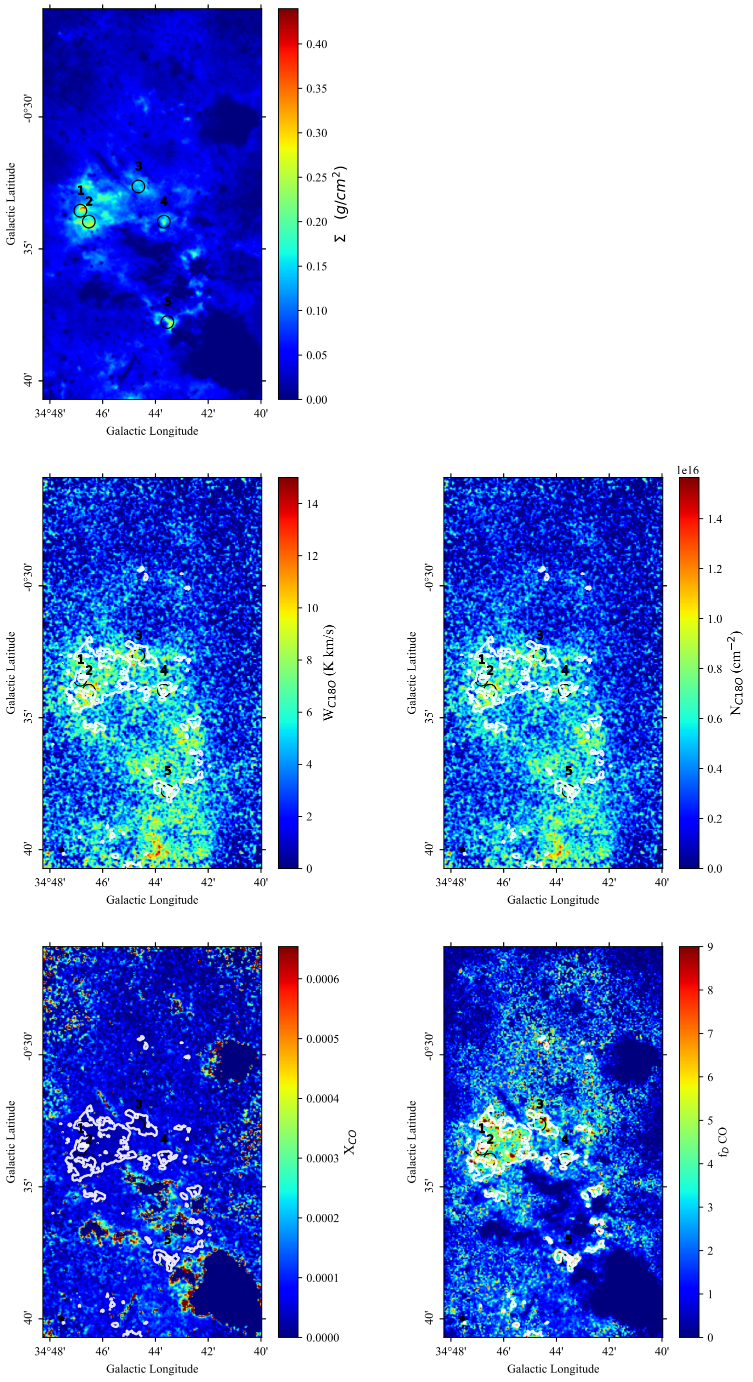

Figure A.7: Top left: the mass surface density obtained with the KT13 method. Middle left: the integrated intensity of $C^{18}O$ over the integration range 36-52.5 km/s. Middle right: the corresponding column density of $C^{18}O$. Bottom left: the corresponding abundance of $C^{18}O$. Bottom right: the depletion factor of CO. The mass surface density is overlayed on top of the middle and bottom rows as white contours. The maps had a pixel size of 2.75 arcsec.

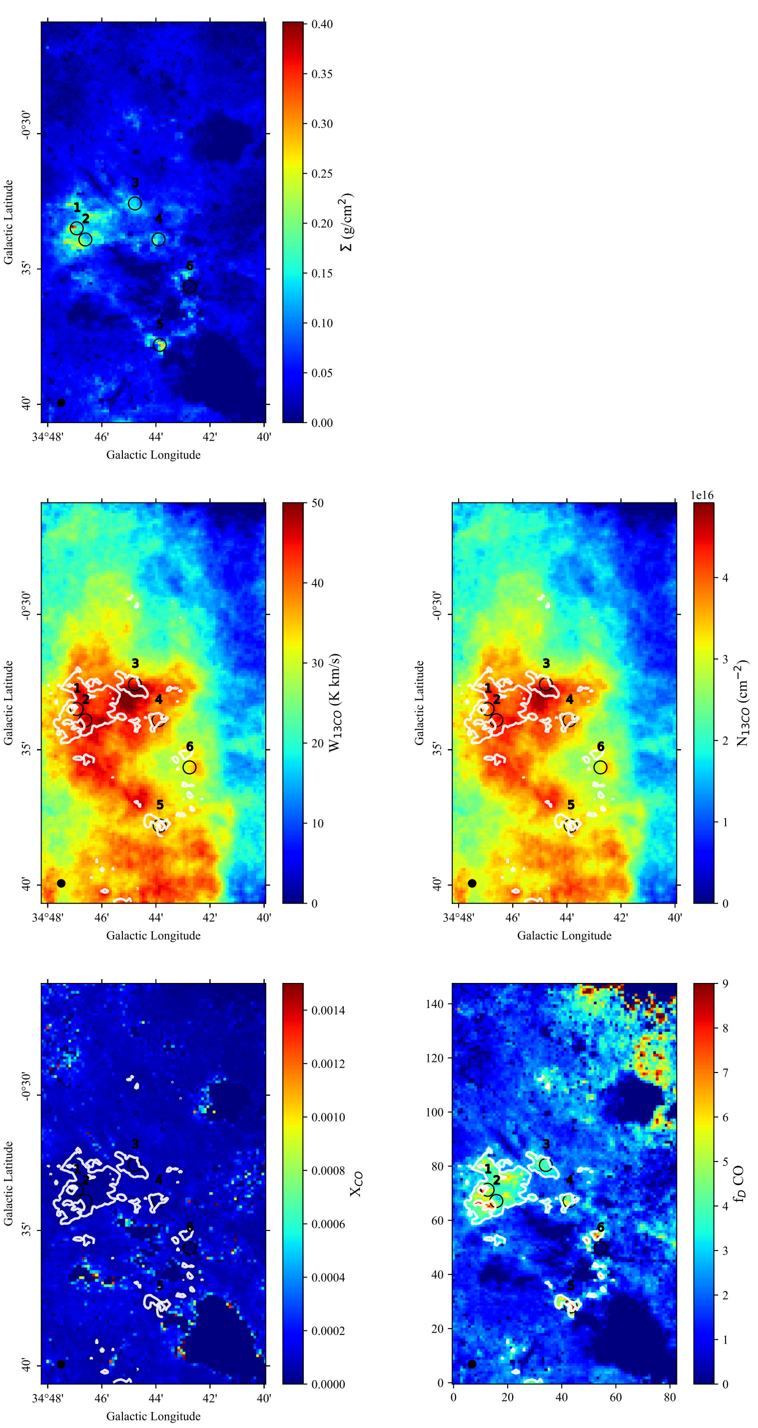

Figure A.8: Top left: the mass surface density obtained with the KT13 method. Middle left: the integrated intensity of ^{13}CO over the integration range 36-52.5 km/s. Middle right: the corresponding column density of ^{13}CO. Bottom left: the corresponding abundance of ^{13}CO. Bottom right: the depletion factor of CO. The mass surface density is overlayed on top of the middle and bottom rows as white contours. The maps had a pixel size of 6 arcsec.

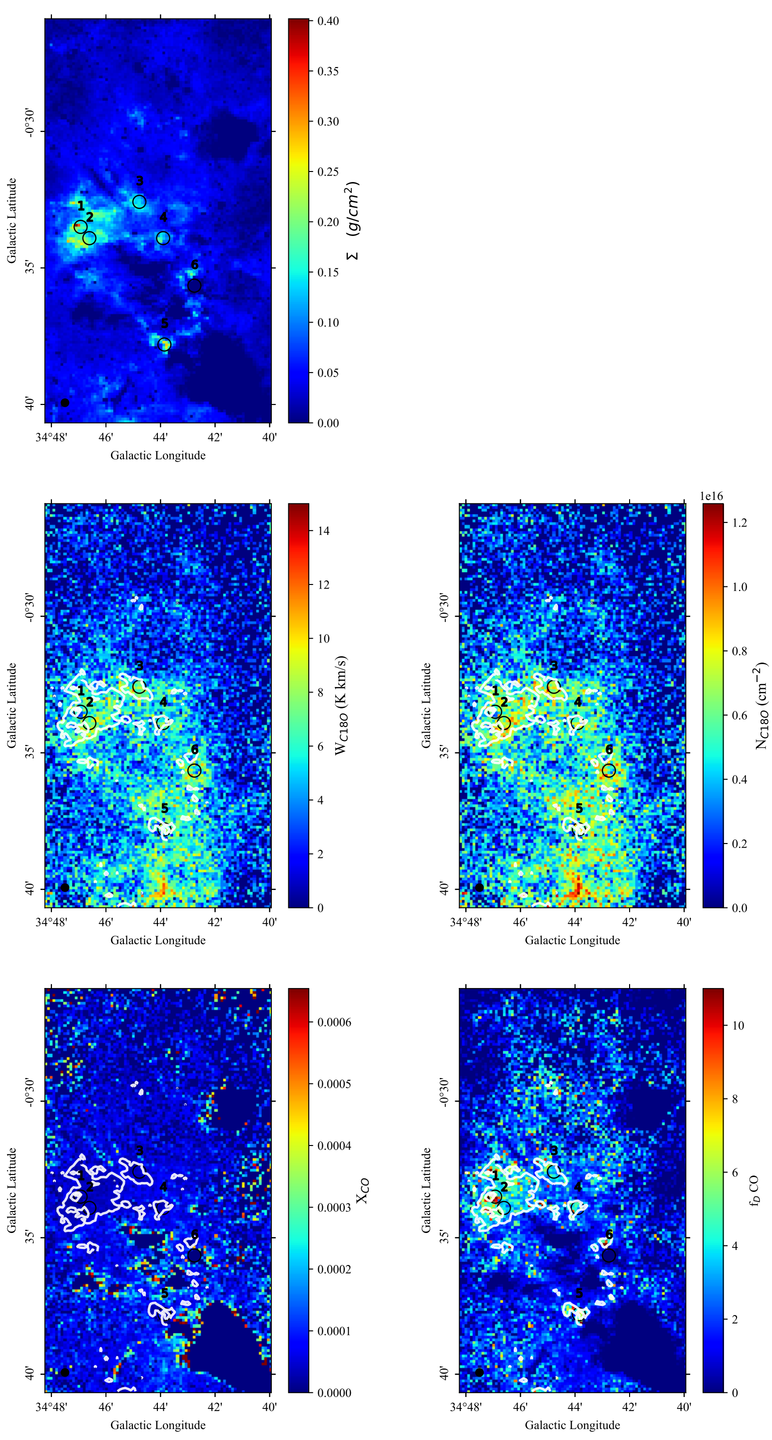

Figure A.9: Top left: the mass surface density obtained with the KT13 method. Middle left: the integrated intensity of $C^{18}O$ over the integration range 36-52.5 km/s. Middle right: the corresponding column density of $C^{18}O$. Bottom left: the corresponding abundance of $C^{18}O$. Bottom right: the depletion factor of CO. The mass surface density is overlayed on top of the middle and bottom rows as white contours. The maps had a pixel size of 6 arcsec.

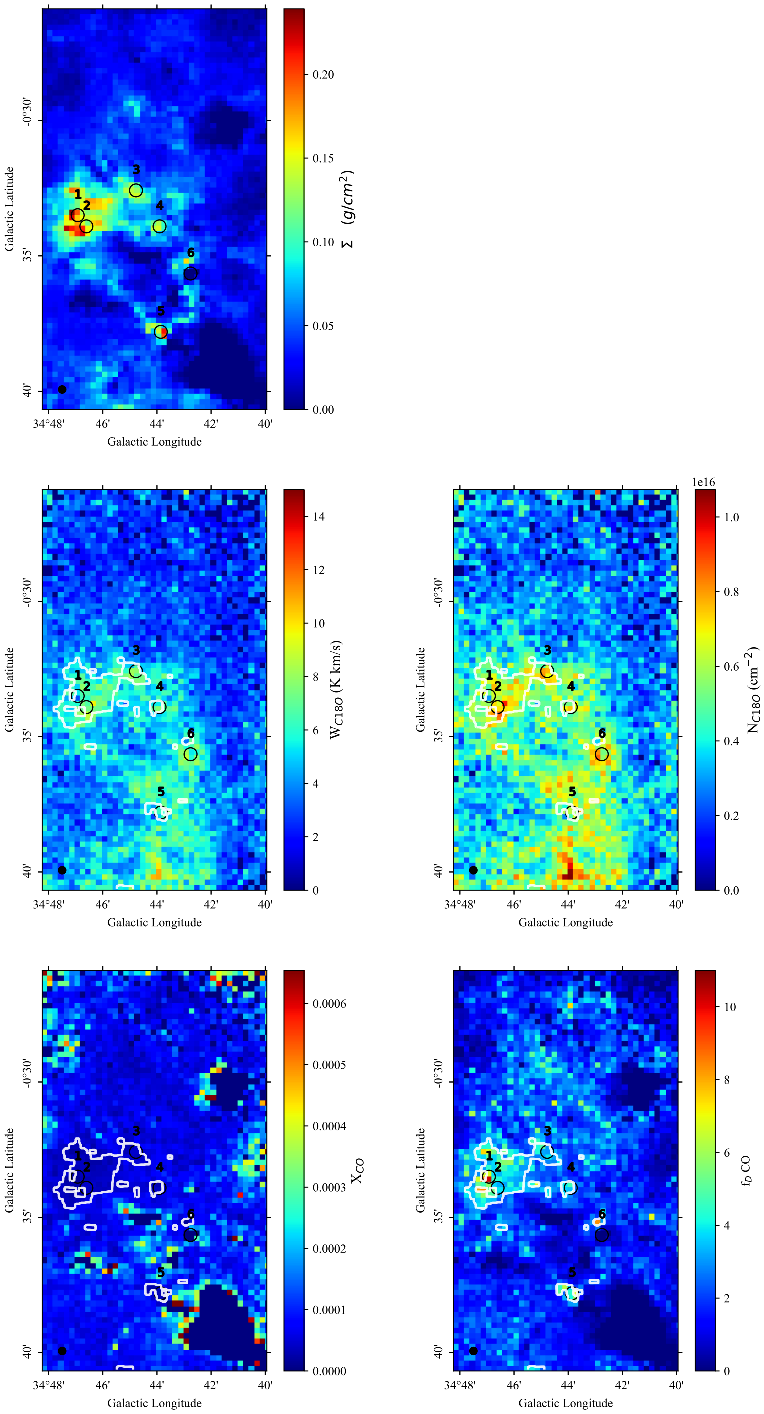

Figure A.10: Top left: the mass surface density obtained with the KT13 method. Middle left: the integrated intensity of C^{18}O over the integration range 36-52.5 km/s. Middle right: the corresponding column density of C^{18}O. Bottom left: the corresponding abundance of C^{18}O. Bottom right: the depletion factor of CO. The mass surface density is overlayed on top of the middle and bottom rows as white contours. The maps had a pixel size of 12 arcsec.

A.0.3 Channel maps

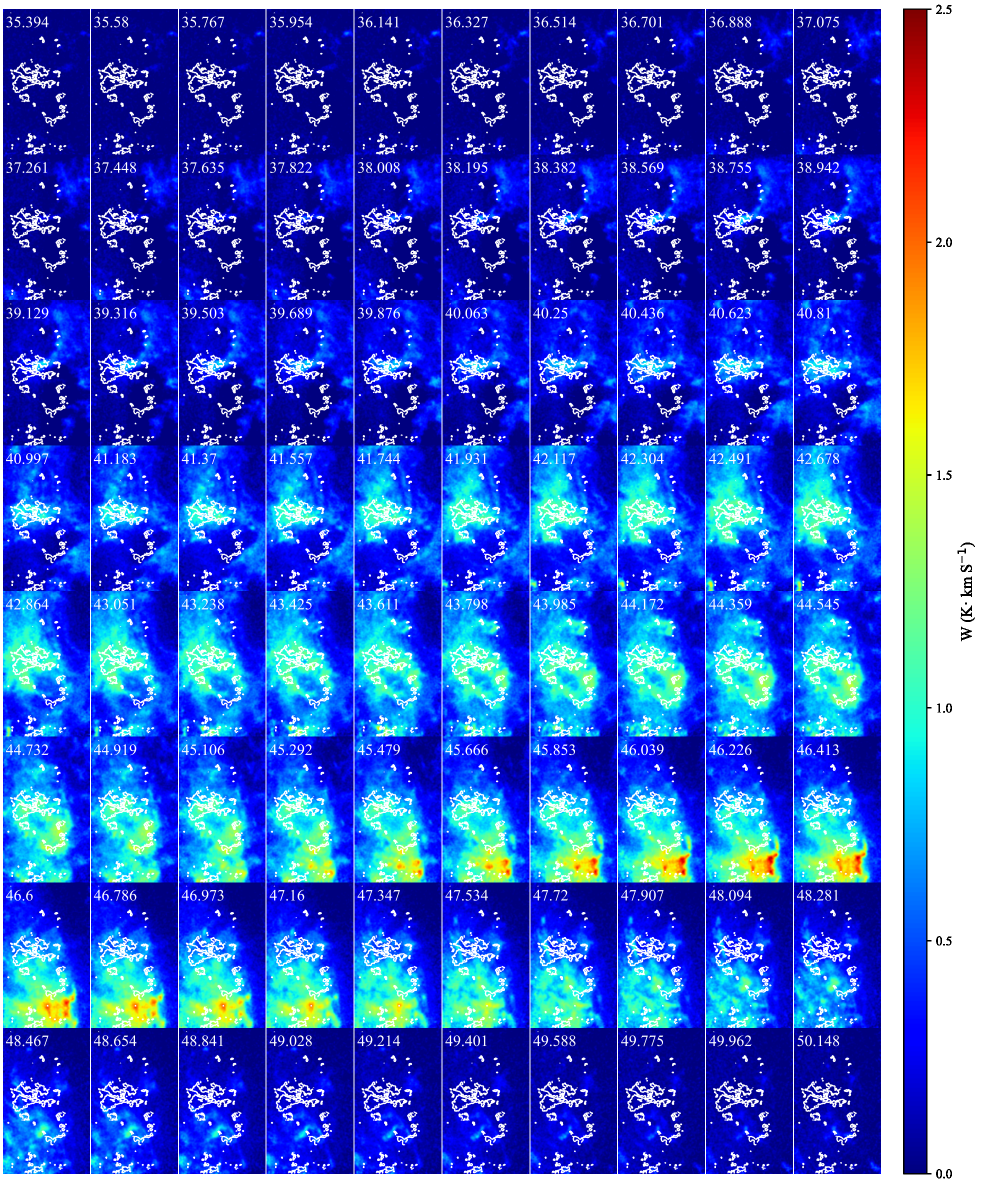

Figure A.11: Channel maps of the ^{13}CO (1-0) line emission towards cloud G. Σ_{KT13} is overlayed on top of each panel in the figure in the form of white contour level. The velocity range shown ranges roughly from 35.7 to 52 km/s in velocity increments of 0.187 km/s. The velocity for each panel is shown in the left corner.

DEPARTMENT OF SOME SUBJECT OR TECHNOLOGY
CHALMERS UNIVERSITY OF TECHNOLOGY
Gothenburg, Sweden
www.chalmers.se

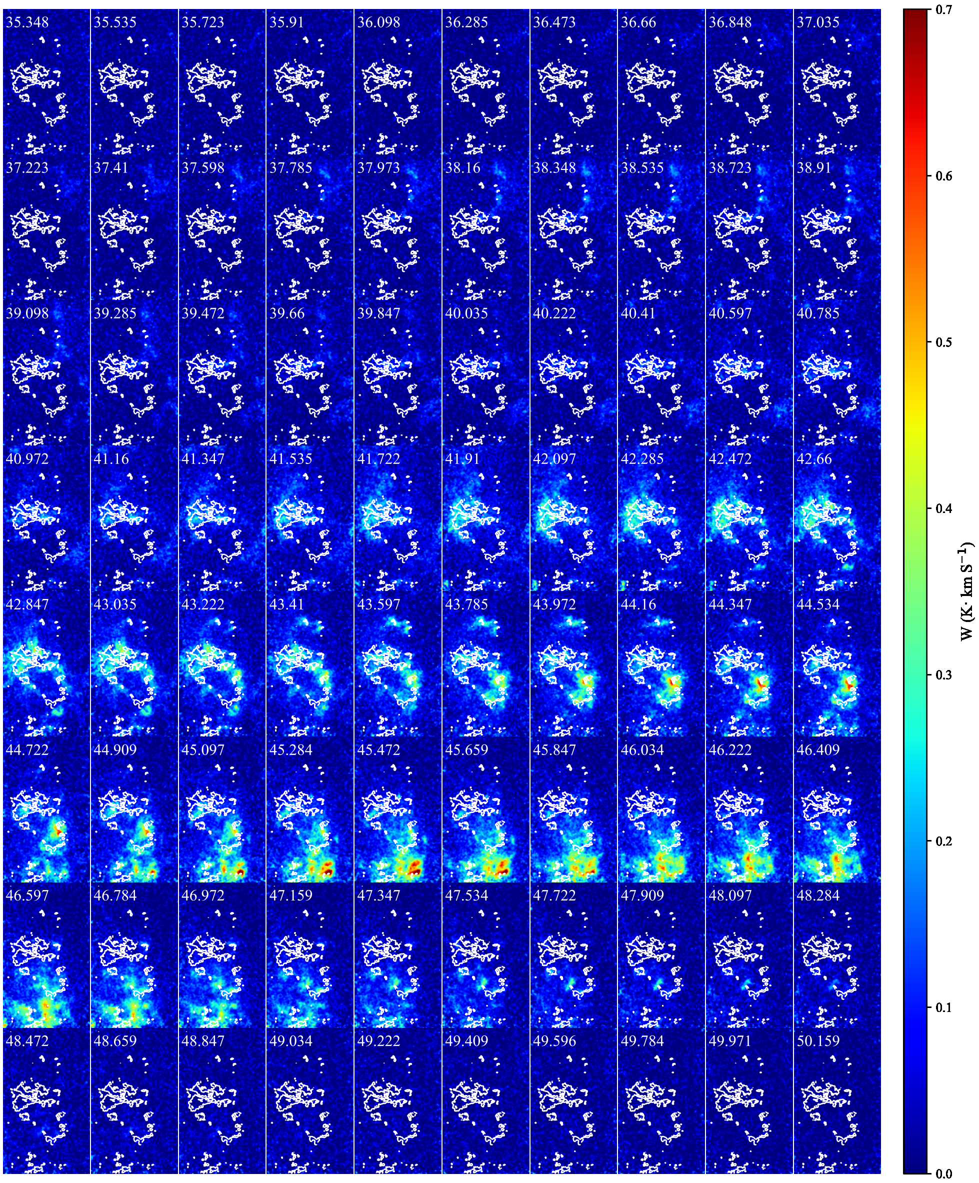

Figure A.12: Channel maps of the ^{13}CO (1-0) line emission towards cloud G. Σ_{KT13} is overlayed on top of each panel in the figure in the form of white contour level. The velocity range shown ranges roughly from 35.7 to 52 km/s in velocity increments of 0.187 km/s. The velocity for each panel is shown in the left corner.